ABSTRACT

Title of Dissertation:	ENERGY DEPOSITION IN FEMTOSECOND FILAMENTATION: MEASUREMENTS AND APPLICATIONS
	Eric Wieslander Rosenthal, Doctor of Philosophy, 2017
Dissertation directed by:	Professor Howard Milchberg Department of Physics

Femtosecond filamentation is a nonlinear optical propagation regime of high peak power ultrashort laser pulses characterized by an extended and narrow core region of high intensity whose length greatly exceeds the Rayleigh range corresponding to the core diameter. Providing that a threshold power is exceeded, filamentation can occur in all transparent gaseous, liquid and solid media. In air, filamentation has found a variety of uses, including the triggering of electric discharges, spectral broadening and compression of ultrashort laser pulses, coherent supercontinuum generation, filament-induced breakdown spectroscopy, generation of THz radiation, and the generation of air waveguides.

Several of these applications depend on the deposition of energy in the atmosphere by the filament. The main channels for this deposition are the plasma generated in the filament core by the intense laser field and the rotational excitation of nitrogen and oxygen molecules. The ultrafast deposition acts as a delta function-like

pressure source to drive a hydrodynamic response in the air. This thesis experimentally demonstrates two applications of the filament-driven hydrodynamic response. One application is the 'air waveguide', which is shown to either guide a separately injected laser pulse, or act as a remote collection optic for weak optical signals. The other application is the high voltage breakdown of air, where the effect of filament-induced plasmas and hydrodynamic response on the breakdown dynamics is elucidated in detail. In all of these experiments, it is important to understand quantitatively the laser energy absorption; detailed absorption experiments were performed as a function of laser parameters. Finally, as check on simulations of filament propagation and energy deposition, we measured the axially resolved energy deposition of a filament; in the simulations, this profile is quite sensitive to the choice of the nonlinear index of refraction (n_2). We found that using our measured values of n_2 in the propagation simulations results in an excellent fit to the measured energy deposition profiles.

ENERGY DEPOSITION IN FEMTOSECOND FILAMENTATION: MEASUREMENTS AND APPLICATIONS

by

Eric Wieslander Rosenthal

Dissertation submitted to the Faculty of the Graduate School of the
University of Maryland, College Park, in partial fulfillment
of the requirements for the degree of
Doctor of Philosophy
2017

Advisory Committee:
Professor Howard Milchberg, Chair
Professor Ki-Yong Kim
Dr. Gregory Nusinovich
Professor Phillip Sprangle
Dr. Jared Wahlstrand

Dedication

To all the hidden beauties in life…

Acknowledgements

I owe a special thank you to the myriad of individuals who have both assisted and supported me in my journey over these past many years. First and foremost, I want to thank my advisor, Howard Milchberg. His willingness to take a chance on me early on in my career has given me an opportunity to flourish as an aspiring scientist, a chance which I may not have been afforded were it not for his belief in my abilities. Graduate school has been a time of great intellectual and professional development for me, and Howard's mentorship has sharpened my skills and experimental acumen, and encouraged me to grow into the scientist I am today.

A special thank you also goes out to the graduate students who mentored me when I first joined the group, Dr. Sanjay Varma, and Dr. Yu-Hsin Chen. I learned a lot from both of them early on, and their warm introduction to the lab both got me up to speed and made me feel at home.

Without the help and support of my fellow graduate students throughout my time at UMD, I wouldn't have been able to accomplish nearly as much as I have. Through many late evenings and sleepless nights, my friend and colleague Dr. Nihal Jhajj and I punctuated the collection and analysis of endless data sets with coffee, jokes, and interesting discussion about everything under the sun. Dr. Sina Zahedpour Anaraki has been a true friend and colleague over the years, and deserves special thanks for always lending an ear when advice was needed, experimental or otherwise. Thanks to Fatholah Salehi, whose friendly demeanor and upbeat attitude has always brightened the lab. Thanks to Dr. Jared Wahlstrand, whose advice and assistance during the 'waveguide years' was indispensable. I am particularly grateful for the assistance given by Ilia Larkin, with whom it has been a pleasure to have worked on both laser building and experiments. I look forward to keeping in touch with you all after my time at UMD is up.

I also wish to acknowledge all of the students of the Big Lab, both past and present – Linus Feder, Robert Schwartz, Daniel Woodbury, Bo Miao, Dr. Sung Jun Yoon, Dr. Jennifer Elle, Dr. Andy Goers, and Dr. George Hine. Although I did not

have the chance to intimately collaborate on scientific projects with all of them, their continued support and camaraderie by way of Town Hall meetings and 'hallway attractor' discussions has been valuable. I would also like to extend my thanks to the undergraduate students Jesse Griff-McMahon, Dan Younis, and Ryan Smith, whose drive towards embarking on further scientific and engineering endeavors has been inspiring and enlightening.

Several members of the IREAP technical staff have also been instrumental in my learning, both scientifically and extracurricular. Many thanks go to Jay Pyle, Don Martin, and Dr. Steven Henderson for introducing me to the machine shop and for passing on volumes of expert shop knowledge. Thanks goes to Nolan Ballew for teaching me many valuable machine shop skills and for fielding my wildest SV questions. Thanks to Tom Loughran and all of the FabLab crew whose help in designing custom optics was invaluable. Thanks to Bryan Quinn for his tireless work in maintaining all of the behind-the-scenes aspects of our building and lab. And thanks to all of the additional IREAP staff who have worked seamlessly to enable all of the research we do.

Outside of the lab, my family and friends who have supported me deserve the utmost thank you. I am particularly indebted to my parents Barry and Leslie and my sisters Lee and Emma. My family has believed in me during my entire journey, even during the times I didn't believe in myself. A very special thank you goes to my wonderful girlfriend Christin Probst, who has been my number one supporter, always encouraging me to press forward in good times and bad, and whose no-nonsense attitude towards my nonsense has often kept me sane!

Table of Contents

List of Tables

List of Figures

Chapter 1: Introduction

1.1. Nonlinear response of gases

The Coulomb electric field internal to the hydrogen atom is approximately $E_0 \sim 10^{11}\,\mathrm{V/m}$. For laser pulses with electric fields E even a small fraction of this field strength, nonlinear optics must be considered when describing the laser-matter interaction [3]. Roughly speaking, for $E/E_0 < \sim 10^{-2}$, perturbative nonlinear optics is adequate, while for larger E/E_0 one must consider non-perturbative nonlinear optics. For commonly available high peak power laser pulses, electric field strengths can routinely satisfy $E/E_0 > 1$. In the perturbative limit, the medium's polarization **P** can be written as the series

$$\mathbf{P}(\omega) = \overline{\overline{\chi}}^{(1)}(\omega)\cdot\mathbf{E}(\omega) + \overline{\overline{\chi}}^{(2)}(\omega)\cdot\mathbf{E}(\omega)\cdot\mathbf{E}(\omega) + \overline{\overline{\chi}}^{(3)}(\omega)\cdot\mathbf{E}(\omega)\cdot\mathbf{E}(\omega)\cdot\mathbf{E}(\omega) + \cdots \qquad (1.1)$$

taking into account the possible frequency dependent and anisotropic medium response, where $\overline{\overline{\chi}}^{(n)}(\omega)$ is a rank $(n+1)$ tensor. This expansion allows classification of nonlinear interactions by the order of the process; that is, the number of wave fields needed to generate the resulting polarization **P** of interest. For example, second harmonic generation is a $\chi^{(2)}$ process whereby two propagating optical fields 'mix' and generate a polarization response **P** which oscillates at twice the frequency of either of the input fields. Sum/difference frequency generation is likewise a two wave mixing process, but with the waves at distinct frequencies. Optical rectification and the Pockels effect are other examples of $\chi^{(2)}$ processes [3].

Many important effects relating to ultrashort laser pulse propagation are $\chi^{(3)}$ processes. Examples are two photon absorption, self- and cross-phase modulation, and "four wave mixing" (where the product wave is considered to mutually interact with the three 'input' waves. In that sense, difference frequency generation, for example, might be considered "three wave mixing"). A very important $\chi^{(3)}$ process in this thesis, playing a central role in filamentation, is the optical Kerr effect. Under conditions of instantaneous and isotropic medium response to the applied fields, the nonlinear polarization can be written

$$P = \left[\chi^{(1)} + \chi^{(3)} E^2 \right] E = \chi_{eff} E \qquad (1.2)$$

$$n = \sqrt{1 + \chi_{eff}} \approx n_0 + n_2 I \qquad (1.3)$$

where χ_{eff} is the effective susceptibility, I is the laser intensity envelope, and $n_2 = \frac{1}{2n_0} \chi^{(3)}$ is the nonlinear index of refraction. Note that $\chi^{(2)} \to 0$ because the response is taken to be isotropic. It is important to note that inside femtosecond filaments, the peak laser intensity of $<\sim 10^{14}\,\mathrm{W/cm^2}$ is no longer perturbative. Nevertheless, experimental work by our group [4], [5] has shown that the leading terms of the perturbative expansion for the Kerr effect (along with the measured values of n_2 for atmospheric atomic and molecular constituents) remain the correct description of the nonlinear response, with ionization being the next major contributor to the nonlinear polarization as the intensity is further increased. This is equivalent to showing that any "high order Kerr effect" is unimportant.

1.1.1. Electronic and rotational nonlinear responses

While monatomic gas atoms experience a near-instantaneous bound electronic nonlinearity (away from atom resonances), molecular gases experience both an instantaneous electronic and a delayed rotational nonlinearity, both of which contribute to the first order correction to the index of refraction. In air, the diatomic molecules N_2 and O_2 dominate the response. At short time scales, the electronic nonlinearity dominates. At the same time, the applied laser field induces a molecular dipole with contributions along and across the bond axis. Viewed classically, the induced dipole is torqued into alignment with the field. Quantum mechanically, a spectrum of rotational eigenstates is excited [6] via the rotational Raman process. For ~40-100 fs laser pulses, as used in the experiments of this dissertation, the laser bandwidth is insufficient for vibrational state excitation by the Raman process [6].

The combined response can be expressed, to second order in the laser electric field, as the transient refractive index shift

$$\Delta n(t) = n_2 I(t) + \int_{-\infty}^{\infty} R(t-t')I(t')dt' \qquad (1.4)$$

where R is the rotational Raman response function, and the first and second terms describe the instantaneous electronic and delayed rotational response. Separating out these terms is often necessary for proper interpretation of experimental results, as experiments that use pulses longer than a few hundred femtoseconds [7], [8] cannot distinguish the electronic from rotational response. Our group's prior experiments

were the first to cleanly separate these contributions to the nonlinearity [1], [4], [9], [10].

1.1.2. Self-focusing

Self-focusing is a direct consequence of the Kerr effect for optical fields whose intensity is a function of space and time. Owing to a typical beam having higher intensity in the center, Eq. (1.3) shows that the beam center will accumulate more nonlinear phase shift then the periphery—this gives rise to inwardly curved (focusing) phase fronts. The critical power threshold P_{cr} for self-focusing is reached when this inward curvature just cancels the natural outward curvature from diffraction [3],

$$P_{cr} = \frac{\pi(0.61)^2 \lambda^2}{8 n_0 n_2} \qquad (1.5)$$

Right at the threshold $P = P_{cr}$, the beam self-focuses to a singularity at infinity. For $P > P_{cr}$, the focus occurs at finite distances. In practice, the singularity is never reached because of various self-focusing arrest mechanisms to be discussed.

1.1.3. Self-phase modulation

Intense laser pulses experience another nonlinear effect called ‘self-phase modulation’, which also arises from the third order optical nonlinearity discussed

earlier. Self-phase modulation has found use in a wide variety of research areas. One of the most important uses is for generation of coherent supercontinuum beams where broad-band white light can be used to provide excellent time resolution for interferometric measurements [11]. This broadband white light can also be used for temporal compression of optical pulses – additional bandwidth can be temporally compensated after generation through the use of dispersive delay inducing optics such as chirped mirrors or fiber Bragg gratings. In self-phase modulation, the third order nonlinearity mediates an interaction between a laser field and itself in the time domain. Self-focusing, discussed above, is the spatial analogue of this process. The instantaneous phase of the pulse is given by

$$\phi(t) = kz - \omega_0 t = \frac{2\pi n(t)}{\lambda} L - \omega_0 t \qquad (1.6)$$

The instantaneous frequency of the pulse, $\omega(t)$, is given by the time rate of change of the phase,

$$\omega(t) = -\frac{d\phi(t)}{dt} = \omega_0 - \frac{2\pi L}{\lambda}\frac{dn(t)}{dt} = \omega_0 - \frac{2\pi n_2 L}{\lambda}\frac{dI(t)}{dt} \qquad (1.7)$$

a changing function of time as the pulse propagates. In particular, for the pulse leading edge, where $\frac{dI(t)}{dt} > 0$, we have $\Delta\omega = \omega(t) - \omega_0 < 0$, or a red-shift. On the pulse trailing edge, $\frac{dI(t)}{dt} < 0$, giving $\Delta\omega = \omega(t) - \omega_0 > 0$, or a blue-shift.

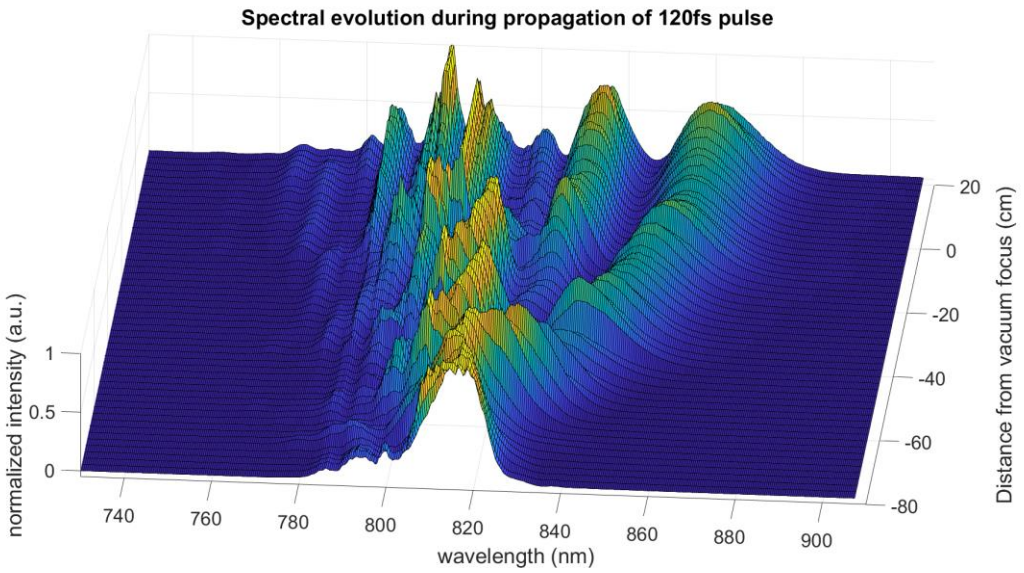

Figure 1.1 Dramatic spectral changes occur during propagation of a ~120 fs, several mJ laser pulse in air. The input laser pulse has a bandwidth of approximately 20 nm centered about 800 nm. After several meters of propagation, the effects of self-phase modulation accumulate and promote the creation of new frequency content spanning from 750 nm to 900 nm.

The result of these frequency shifts on the propagation of a high power pulse in a Kerr medium can often be seen quite dramatically when examining the spectral content the pulse throughout its propagation, as shown in Figure 1.1. Initially, the pulse has a bandwidth of approximately 20 nm centered about 800 nm. The spectral broadening induced through self-phase modulation from the Kerr and molecular rotational nonlinearities and ionization allows generation of new frequency components spanning the entire range from 750 nm to 900 nm.

1.1.4. Photo-ionization

Due to the strong electric fields present in pulsed laser radiation, ionization of the medium through which a laser pulse travels often becomes a factor relevant to the propagation. Ionization of gases and subsequent propagation of a laser pulse through

the laser produced plasma are central in the description of femtosecond laser filamentation, where the free electrons generated during the ionization act to defocus the remainder of the pulse and arrest self-focusing collapse. Two main ionization mechanisms, multiphoton ionization and tunnel ionization are important for plasma generation by propagating femtosecond pulses. In general, at atmospheric pressure, femtosecond pulses are temporally too short to drive avalanche ionization.

Keldysh [12] provided a dimensionless parameter $\gamma_K = \sqrt{U_i / 2U}$, which is used to identify whether an ionization process is more multiphoton ionization-like or tunneling ionization-like. Keldysh theory gives the full behavior of the ionization process, where the high field, non-perturbative limit is tunneling ($\gamma_K \ll 1$) and the low field perturbative limit is multiphoton ionization (MPI) ($\gamma_K \gg 1$). Here, U_i is the ionization potential of an atom or molecule, and $U = e^2E^2 / 4m\omega_0^2$ is the quiver energy (or ponderomotive energy) of a free electron in the laser field [13]. For the conditions common to femtosecond filaments in atmosphere, i.e. peak intensities $<10^{14}$ W/cm^2 at λ = 800 nm, the ionization process is in the intermediate range of γ_K lying closer to MPI [13], [14].

For laser pulses at λ = 800 nm, the photon energy is $h\nu \approx 1.5$ eV. The MPI rate scales with intensity as I^K, where in the case of oxygen, K = 8 (oxygen ionization potential U_i = 12.1 eV). At higher fields, the electric field of the laser is capable of distorting the atomic/molecular potential well. In the presence of this field-distorted potential, an electron has a greater probability of undergoing tunneling through the diminished potential barrier. Figure 1.2 illustrates MPI and tunneling.

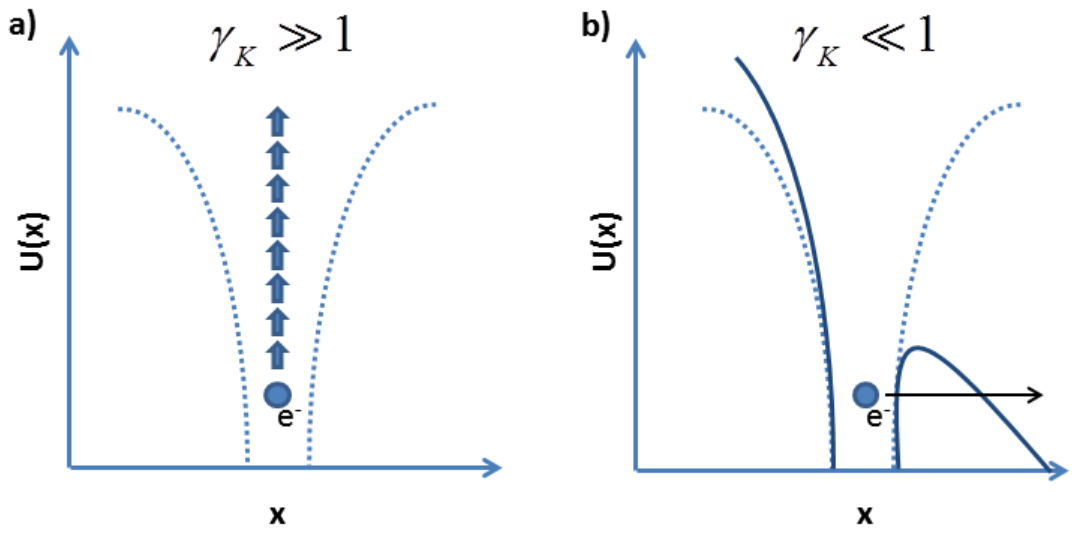

Figure 1.2 Illustration of the two common ionization channels present in ultrashort laser matter interactions. (a) Multiphoton ionization typically proceeds through the successive absorption of several laser photons imparting energy exceeding the ionization threshold to a bound electron. (b) Tunnel ionization, occurring through field distortion of the bound electron's potential barrier provides a decreased potential through which the electron may be promoted to the continuum.

1.1.5. Plasma defocusing

Due to the very fast (~fs) timescale for photoionization, the rising edge of the temporal pulse envelope will liberate electrons, and the remainder of the pulse will experience the refractive effect of these free electrons. Because of the high-order dependence of ionization yield on intensity, these free electrons tend to be concentrated on axis, and their optical response defocuses the pulse. Ignoring collisions (a good assumption for femtosecond pulses and low density gases), the plasma dielectric constant is

$$\varepsilon = 1 - \frac{4\pi n_e e^2}{m_e \omega^2} = 1 - \frac{\omega_p^2}{\omega^2} \qquad (1.8)$$

where m_e is the electron mass, n_e is the density of electrons, e is the electron charge, and $\omega_p = \sqrt{\frac{4\pi n_e e^2}{m_e}}$ is the plasma frequency. Thus, we can write the index of refraction, as before, in terms of the dielectric constant as

$$n = \sqrt{\varepsilon} = \sqrt{1 - \frac{\omega_p^2}{\omega^2}} = \sqrt{1 - \frac{n_e}{n_c}} \approx 1 - \frac{n_e}{2n_c} \qquad (1.9)$$

where n_e is the electron density and $n_c = \frac{m_e \omega^2}{4\pi e^2} \approx 1.7\text{x}10^{21}\text{cm}^{-3}$ (at λ = 800 nm) is the critical density. Here we used $n_e / n_c \ll 1$, which is the case for the experiments of this thesis, for which $n_e / n_c \sim 10^{-5}$.

1.2. Filamentation

As discussed earlier, an intense pulse propagating in a transparent medium induces a nonlinear correction to the refractive index through the Kerr effect. This index of refraction perturbation co-propagates with the pulse as a self-lens. Once the laser pulse peak power exceeds a critical value, typically $P > P_{cr}$ ~5-10 GW in gases [1], [15], the self-induced lens overcomes diffraction and focuses the beam, leading to plasma generation and beam defocusing when the gas ionization intensity threshold is exceeded. The dynamic interplay between self-focusing and defocusing leads to self-sustained propagation of a tightly radially confined high intensity region accompanied by plasma of diameter < 100 μm [16] over distances greatly exceeding the optical Rayleigh range. Long range filamentation of intense femtosecond laser pulses in

gases is an area of increasing interest, as it combines exciting potential applications with fundamental nonlinear optical physics [15], [17], [18]. Since its first demonstration in gaseous media [19], it has found a variety of uses, including triggering of electric discharges [20], spectral broadening and compression of ultrashort laser pulses [21]–[24], coherent supercontinuum generation [25], filament-induced breakdown spectroscopy [26], and generation of THz radiation [27]–[29]. Filaments can extend from millimeters to hundreds of meters, depending on the medium and laser parameters [15]. More recently, femtosecond filaments have been used by our group to generate air waveguides, utilizing the long timescale gas density depression that remains in the wake of a filamenting pulse [30]. As will be demonstrated in Chapter 2 and Chapter 3 of the thesis, these waveguides have been shown to be viable for the guiding of externally injected high peak and high average power laser pulses [30], and also for the remote collection of optical signals for spectral analysis [31].

A schematic representation of filament dynamics is shown in Figure 1.3. Here, the self-focusing collapse at the left of the figure is followed by plasma generation, identified by the yellow regions in the figure. Defocusing which occurs during the propagation of the pulse through the self-produced plasma is then followed by additional self-focusing when the pulse intensity remains high enough to support the Kerr nonlinearity. A plasma filament in air can proceed through several such focusing/defocusing/refocusing cycles, the combined effect of which allows the pulse to retain its tightly collimated plasma producing mode over many Rayleigh ranges.

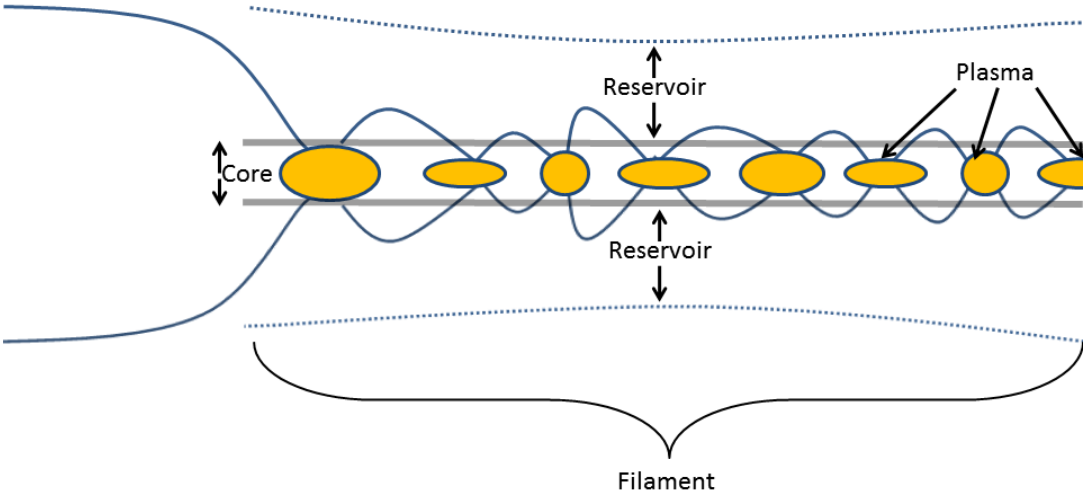

Figure 1.3 Schematic representation of the filamentation process demonstrating self-focusing collapse followed by plasma induced defocusing and Kerr induced re-focusing, both of which repeatedly occur along the propagation direction. Also depicted are the two transverse spatial regions of the filament, known as the 'core' and the 'reservoir', the interplay between which allows extended propagation of ultrashort laser pulses.

Central to the research presented in this thesis is the role played by energy deposition during femtosecond filamentation, which occurs under our conditions of ~40-100 fs, λ = 800 nm pulses and atmospheric pressure air. The main deposition mechanisms are plasma generation by laser field ionization and molecular rotation of nitrogen and oxygen molecules. The air waveguide concept presented in Chapters 2 and 3 relies critically on energy deposited from the laser pulse into the medium, where the deposited energy drives a hydrodynamic response of the neutral gas. The magnitude and spatial distribution of this neutral gas density perturbation directly dictates the usefulness of such schemes. In Chapters 4 and 5 of the thesis, mechanisms through which energy deposition results from femtosecond filamentation in air are described in detail, and measurements which shed light on the magnitude and spatial distribution of this energy deposition are presented.

1.2.1. Single vs multiple filamentation

It is important to note that filamentation cannot proceed in its most simple form as a single core and reservoir for arbitrarily large input pulse powers. Since filamentation is seeded during propagation via a modulational instability, an increase in input pulse power leads to several locations across the beam's transverse profile which can collapse. For very high input pulse powers, $P \gg P_{cr}$, optical beams will collapse into a large number N of individual filaments, where $N \sim P / P_{cr}$ [32]. Figure 1.4 shows images of typical far-field intensity profiles exhibited by filaments in both the single filament regime, as well as the multiple filament regime.

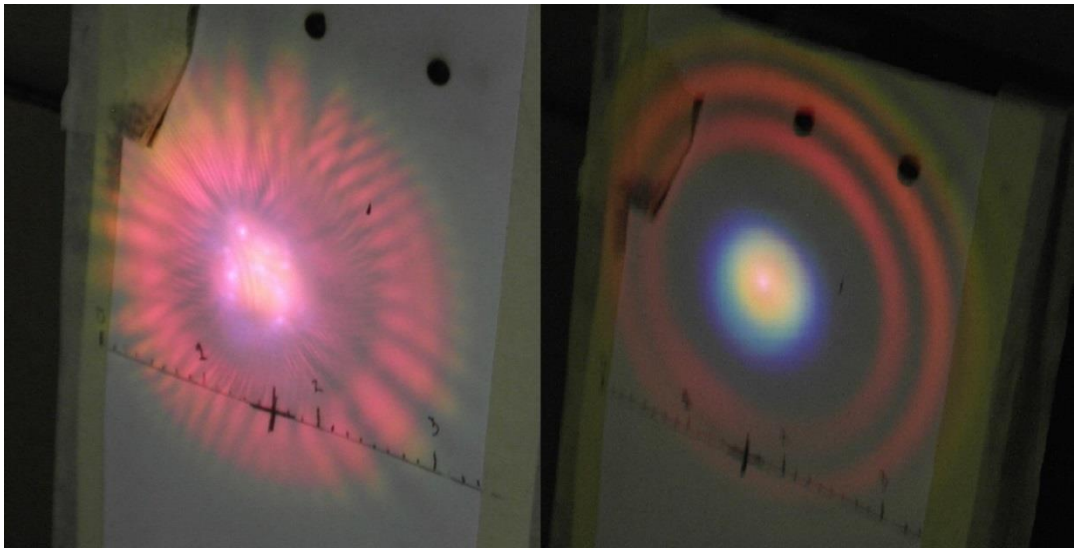

Figure 1.4 (a) Photograph of the typical far field intensity profile of a multiply filamenting beam. Several individual filament cores can be seen throughout the transverse profile, each of which carries optical power roughly corresponding to P_{cr}. (b) Photograph of the typical far-field intensity profile of a single filament. Broadband coherent white light generation on axis is accompanied by conical emission at the periphery.

1.2.2. Patterned filamentation and multi-lobed beams

Most filamentation studies have proceeded using either single filaments, by controlling the input laser power to lie below the threshold necessary for formation of multiple filament cores, or through multiple filamentation, which occurs at much higher pulse powers, $P \gg P_{cr}$ [15]. Typical multifilament experiments utilize a very high peak power laser pulse whose spatial profile evolves via modulational instability into several distinct filament cores. The spatial distribution of these filament cores across the beam are typically dictated by small perturbations on the intensity profile, characteristic of common amplification schemes. Several studies have examined the possibility to control the multi-filamentation process through the use of stepped phase masks [30], [31], [33], microlens arrays [34], or spatial light modulators [35] which can control the spatial phase variation of a filamenting beam. In the research of this dissertation, both home-made and commercially available phase-shifting optics have been utilized to achieve controlled multiple filamentation. Shown below in Figure 1.5 is a photograph of a typical far-field profile of a four-lobed beam undergoing filamentation. This beam is generated using an initial TEM_{11} transverse mode. After several meters of propagation, each lobe initiates its own filament which is accompanied by visible conical emission and strong supercontinuum generation leading to white light generation in the cores.

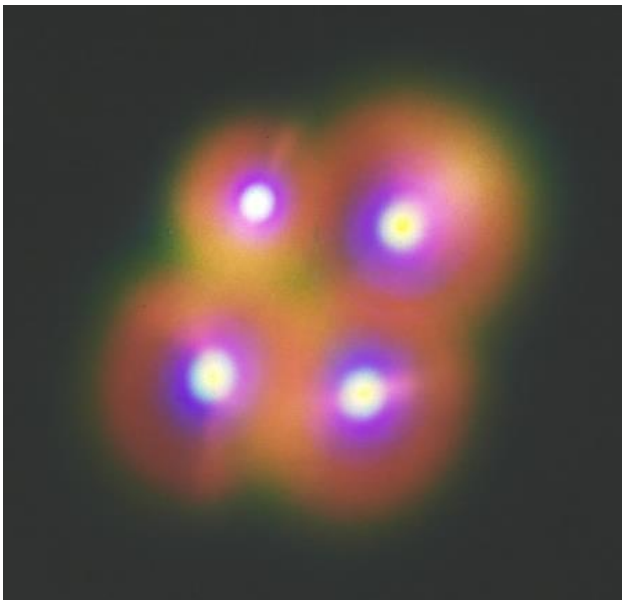

Figure 1.5 Photograph of the typical far field intensity profile of a patterned filamenting beam. Four individual filament cores can be seen throughout the transverse profile, which is seeded from a TEM_{11} input beam created using a homemade reflective phase plate.

The generation of these multi-lobed beams has proven useful for the demonstration of air waveguides, which utilize the patterned hydrodynamic response in the wake of a filamenting beam such as that shown in Figure 1.5 above. In the next section, we describe the fabrication of reflective and transmissive phase shifting optics for generating multi-lobed beams.

1.2.2.1. Transmissive vs reflective phase masks

The results presented in Chapter 2 and Chapter 3 required the generation of multi-lobed beams, with each lobe having a π phase shift relative to its neighboring lobes. These beams were used to create patterned filamentation and produce air waveguides utilizing the hydrodynamic response of the air in the wake of filamentary propagation. In the experiments presented in Chapter 2, multi-lobed beams were

generated from two orthogonally mounted half-pellicle beamsplitters, as shown in Figure 2.2. Although successful at imprinting the desired phase mask on the filamenting beam, the half-pellicles proved to be both difficult to produce and align. Half-pellicles were produced in our lab by cutting commercially available pellicle beamsplitters through their centers with a sharp blade. Due to the tension under which the pellicle membrane is suspended, the edge which was cut exhibited a tendency to loosen and curl, producing undesirable diffraction at the phase-shifted interface. Furthermore, the alignment of the half-pellicles was tedious, requiring precise angle tuning to achieve the proper phase shift.

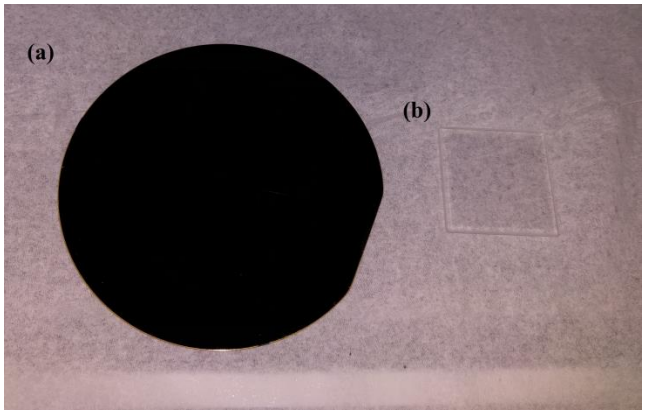

Figure 1.6 Reflective and transmissive phase plates generated using photolithography techniques are shown. (a) Reflective phase plate made by etching a ~200 nm step into a separately grown layer of SiO_2 onto a silicon wafer substrate, then coated with gold. (b) Transmissive phase plate made by etching a ~783 nm step into a BK7 glass window substrate.

In order to ameliorate these difficulties, both transmissive and reflective phase plates were fabricated out of BK7 glass windows and gold-coated silicon wafer substrates, respectively. For the case of a transmissive phase plate, in order to impose a π phase shift across half the beam, a step of height $d = \pi = \frac{\lambda}{2(n_{glass} - n_{air})}$ is etched

into half of the substrate. For a laser beam of wavelength λ = 800 nm, the refractive index of BK7 glass is $n_{glass} \approx 1.5108$, the refractive index of air is $n_{air} \approx 1.0003$, and the appropriate step height is $d \approx 783\,\text{nm}$. This step height can be applied in any desired pattern through the use of well-known photolithography techniques. The phase mask depicted in Figure 1.6(b) was produced by first coating one side of a 25.4mm square x 3mm thick BK7 substrate with standard photoresist on a spinner table. A binary mask made of aluminum machined to the desired pattern is placed over the photoresist covered sample, and ultraviolet light is allowed incident on the photoresist through the negative space in the mask. Exposed photoresist is removed from the surface using acetone and isopropyl alcohol, and the un-coated portion of the substrate is then etched using a buffered oxide etchant, which reacts with the BK7 substrate at a known rate. The depth of etch is controlled by submersing the substrate in the buffered oxide etch for a predetermined amount of time.

For the case of a reflective phase plate, the appropriate spatial phase shift is imposed upon an incident beam in a similar manner, but utilizing a path length difference entirely in air. In this case, the appropriate step size fabricated onto the mask is given by $d = \frac{\pi}{2} = \frac{\lambda}{4n_{air}} \approx 200\,\text{nm}$. For the reflective phase mask shown in Figure 1.6(a), this step was produced through a similar photolithography process utilizing plasma enhanced chemical vapor deposition (PECVD), followed by a buffered oxide etch. As a first step, the pre-determined thickness of SiO_2 $(d = 200\,\text{nm})$ is grown on a 4" diameter Si wafer substrate using an Oxford PlasmaLab 100 PECVD system. The sample is then coated with standard photoresist

on a spinner table. A binary mask made of aluminum machined to the desired pattern is placed over the photoresist covered sample, and ultraviolet light is allowed incident on the photoresist through the negative space in the mask. Exposed photoresist is removed from the surface using acetone and isopropyl alcohol, and the un-coated portion of the substrate is then etched using a buffered oxide etchant. The optic is then cleaned of all remaining photoresist. In order to increase reflection efficiency of the fabricated phase plate, the finished optic was sputter-coated with a thin layer (~15 – 20 nm) of gold, which can be deposited very uniformly, and exhibits high reflectivity in the vicinity of λ = 800 nm.

1.3. 2.5 TW Ti:Sapphire system

The experiments described in this thesis were all performed with a 2.5 TW laser amplifier chain, which will now be detailed. The system is seeded with a femtosecond oscillator (Coherent Mantis) which outputs ultrafast laser pulses of ~35 fs FWHM at a repetition rate of 80 MHz. Pulse energy is 6 nJ, leading to average power output of ~0.5 W. Pulses from the oscillator are then passed to a commercial regenerative amplifier (Coherent Spitfire). This amplifier includes a dispersive pulse stretcher based around a single diffraction grating, two Pockels cells for actively switching the seed pulse into and out of the cavity, and a Brewster cut Ti:Sapphire gain medium. The Ti:Sapphire crystal of the regenerative amplifier is pumped by a Coherent Evolution producing ~9 W of pump power @ 527 nm. After regenerative amplification of the seed pulse, the resultant pulse train has ~1 mJ per pulse with a

pulse repetition rate of 1 kHz. This pulse train is then passed through a Faraday isolator to prevent back-reflections generated downstream from entering the regenerative amplifier. Next, the beam is passed through an external Pockels cell pulse slicer. Utilizing an externally controllable Pockels cell allows an additional level of extinction of any pre-pulse which may develop in the regenerative amplifier, and also allows for the repetition rate to be decreased to 10 Hz for subsequent stages of amplification.

The next two stages of amplification are each performed in a multi-pass configuration. Both stages are pumped with a ~10 ns, 532 nm, frequency doubled Nd:YAG laser (Spectra Physics QuantaRay GCR-270). This laser's 10 W output is split between two amplification stages, labelled as PA1 (Power Amplifier 1) and PA2 (Power Amplifier 2). PA1 is composed of a Brewster cut, 12 mm diameter Ti:Sapphire crystal pumped with 350 mJ of the Nd:YAG pump beam, while PA2 is composed of a flat cut Ti:Sapphire crystal pumped from both sides with the remaining 650 mJ from the QuantaRay GCR-270. In the first stage of amplification (PA1), the 10 Hz output pulse from the regenerative amplifier and pulse slicer makes three passes (arranged in a bow-tie configuration) through the Ti:Sapphire crystal achieving pulse energy of ~10 mJ. The beam is then passed through a transmissive telescope to optimize the input beam dimeter for the next amplification stage. PA2 consists of four passes (arranged in a ring configuration) of amplification through a flat-cut 10 mm diameter Ti:Sapphire rod. Total pulse energy after this second stage of amplification is ~160 mJ. Pulses are then sent into a dual-grating pulse compressor, the energy to which is controlled by an upstream half-waveplate and

thin-film polarizer. The pulse compressor is capable of fine control of the group velocity dispersion and third order dispersion of the compressed pulse, allowing continuous adjustment of the pulsewidth. The compressor efficiency was measured to be ~65%. A minimum pulsewidth of ~40 fs was routinely measured using single shot autocorrelation, resulting in a final stage pulse output of ~100 mJ / 40 fs = 2.5 TW.

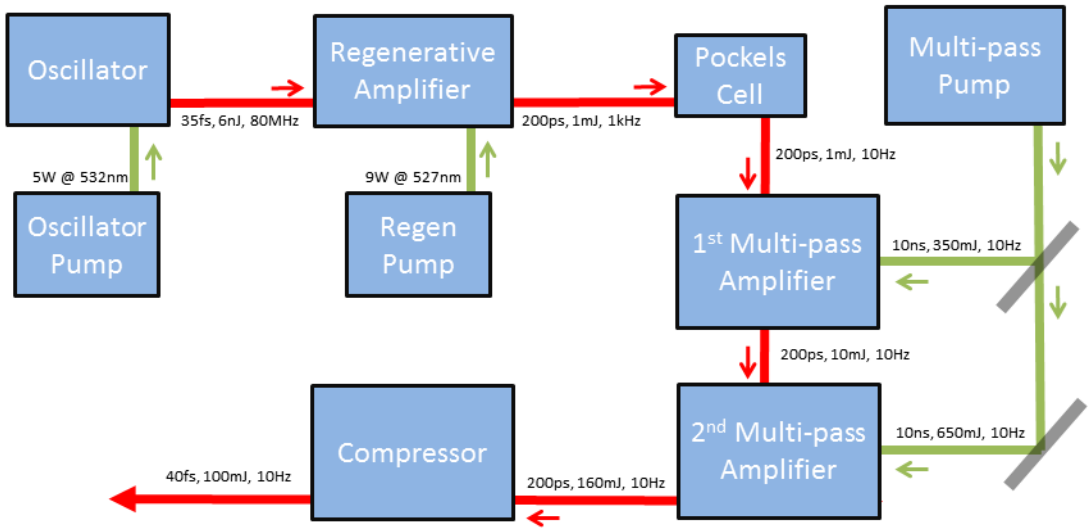

Figure 1.7 Schematic diagram of the UMD 2.5 TW laser system.

A schematic diagram of the entire laser system is shown above in Figure 1.7. Downstream of the grating compressor, we have an optical table for pulse diagnostics and a 10 m filament range for experiments.

1.3.1. 10 TW Ti:Sapphire system upgrade

In an effort to expand the range of our waveguiding experiments described in Chapter 2 and Chapter 3, our laser amplifier has recently been upgraded to produce

~400 mJ compressed output. This required a complete redesign of our existing two stage multi-pass amplifier system, an effort which will be described in this section.

The new 10 TW amplifier utilizes a similar multi-pass architecture, but this time in a single bowtie configuration pumped on either side by separate Nd:YAG pump lasers (Spectra Physics QuantaRay GCR-270 and Spectra Physics QuantaRay PRO-290). Each pump laser outputs ~900 mJ of 532 nm, 10 ns FWHM pulses at 10 Hz repetition rate towards a 12 mm diameter, 15 mm long Ti:Sapphire gain medium. The same regeneratively amplified seed pulse described before is passed through this amplifier in five passes, allowing for final amplified pulse energy of ~600 mJ. This pulse train is then sent towards a vacuum spatial filter for cleaning of the transverse intensity profile of the beam. The design of the laser amplifier is included as a schematic diagram with beam lines superimposed below in Figure 1.8.

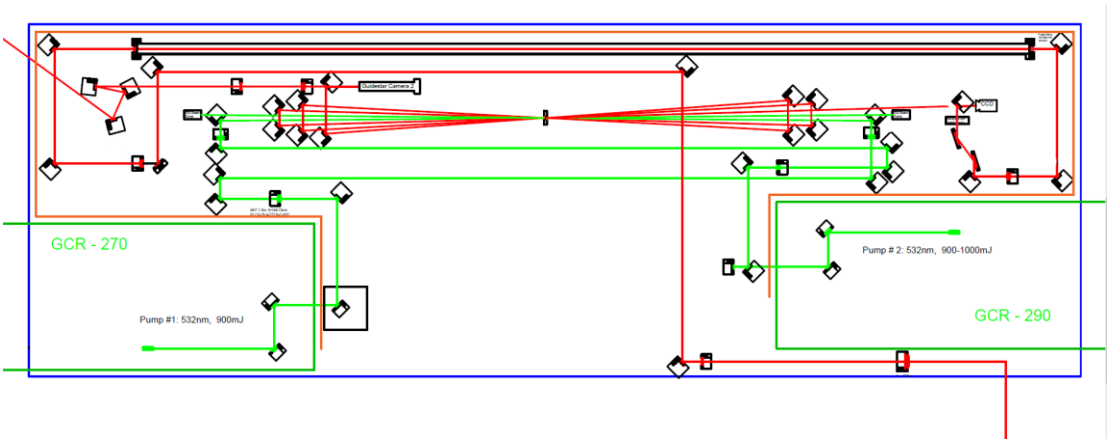

Figure 1.8 Schematic diagram of UMD 10 TW amplifier. Pump laser beam lines are shown in green, while the amplified seed beam path is shown in red.

Beam size and pulse energy achieved in the amplifier were carefully considered during design of the amplifier using a simulation of the Frantz-Nodvik equation. This modelling describes the evolution of the seed laser beam and the stored energy in the

gain medium during the amplification process, and was used to inform our choices of pump and seed beam diameters and pump energy required to reach saturation fluence in the Ti:Sapphire.

1.4. Outline of the Thesis

The outline of the thesis is as follows: Chapter 2 will present demonstration of the 'air waveguide', a novel technique utilizing the hydrodynamic response in the wake of filamentation to guide a separately injected laser beam. The hydrodynamic response occurring in the wake of filamentation is detailed, and the creation of multifilament guiding structures is demonstrated and analyzed. In Chapter 3, experimental results are presented demonstrating use of air waveguides as a collection optic for remotely generated optical signals. In order to advance the possibility of utilizing waveguides over a larger distance, further efforts were undertaken to understand the mechanisms determining their formation. In Chapter 4, the longitudinal dependence of the energy deposition in femtosecond filamentation is investigated both experimentally and numerically. Using a sonographic approach, the energy deposited into the air (which ultimately acts as the driver for the hydrodynamic response creating the waveguide) is measured and compared to a simulation of pulse propagation for a variety of input pulse parameters. Separate measurements of the nonlinear refractive index in air are corroborated through these measurements. In Chapter 5, axially resolved measurements of energy deposition are presented for single filaments in atmosphere. In Chapter 6, preliminary

measurements are presented of the effect on high voltage discharge dynamics of femtosecond filament heating of the air between the electrodes. It is found that the depth of the density depression left behind by an ultrafast laser pulse is strongly affected by the interaction between the laser produced electrons and the applied HV electric field.

Chapter 2: High power optical waveguide in air

2.1. Introduction and motivation

Despite the applications discussed in the previous sections, it remains a significant limitation that femtosecond filamentation cannot deliver high *average* power over long distances in a single tight spatial mode. This is due to the fact that for laser pulses with $P \sim$ several P_{cr} , the beam will collapse into multiple filaments [36] with shot-to-shot variation in their transverse location. For $P_{cr} \sim$ 5-10 GW, this means that single filament formation requires pulses of order ~1 mJ. For a 1 kHz pulse repetition rate laser, this represents only 1 W of average power.

In this chapter, a method employing filaments that can easily supersede this limitation is demonstrated by setting up a robust, long range optical guiding structure lasting milliseconds. It opens the possibility for optical guiding of megawatt levels of average power over long distances in the atmosphere. The guiding structures demonstrated here have substantial potential for directed energy applications [37].

The generation of long-lived thermal guiding structures in air using filament arrays also has the potential to enhance other photonics applications in the atmosphere. For instance, they could be used to concentrate heater beams for remote atmospheric lasing schemes [38] or for inducing characteristic emission for standoff detection of chemical compounds. Many remote detection applications rely on the collection of fluorescence [39]–[41]. For these remote-sensing schemes where detection over large distances may be desired, very little of the isotropically emitted fluorescence reaches the detector at a distance. In Chapter 3, an experimental demonstration is presented, showing that the long-lived guiding structures introduced

here could be used as an effective collection lens, enhancing signal-to-noise ratios in such schemes. They may also find use in atmospheric laser communication[42]. Finally, they might also be used to enhance and control the propagation of an injected ultrashort filamenting pulse [43], similar to what has been done with a permanent refractive index structure in glass [44] and recently with the plasma from an array of filaments in air [45].

We note that there has been much recent work on using the refractive index of the *plasma* generated by an array of filaments to form guides for microwaves [46], [47] and nanosecond optical pulses [48]. We emphasize that the guiding we demonstrate here does not use the optical response of the plasma – rather, it uses the ~10^6 times longer duration hydrodynamic response of the gas after heating by the filaments.

2.2. Gas hydrodynamic response

Recently we found that a femtosecond filament, starting at an electron temperature and density of a few eV and a few times 10^{16} cm^{-3} [16], acts as a thermal source to generate long-lived gas density hole structures that can last milliseconds and dissipate by thermal diffusion [49]. In air, additional heating can occur from molecular excitation [49], with peak deposited energy density in the plasma and molecules of as much as ~100 mJ/cm^3. Our earlier gas density measurements [49] were limited to ~40 μs resolution, so the early time dynamics on the nanosecond timescale had been simulated but not directly measured. These structures are initiated as the filament plasma recombines to a neutral gas on a ~10 ns timescale and the

molecular excitation (if applicable) thermalizes. Owing to the finite thermal conductivity of the gas, the initial energy invested in the filament is still contained in a small radial zone, but it is repartitioned into the translational and rotational degrees of freedom of the neutral gas. The result is an extended and narrow high pressure region at temperatures up to a few hundred K above ambient. In air, this pressure source launches a radial sound wave ~100 ns after the filament is formed. By ~1 μs, the gas reaches pressure equilibrium with an elevated temperature and reduced gas density in the volume originally occupied by the filament, after which the 'density hole' decays by thermal diffusion on a few millisecond timescale [49].

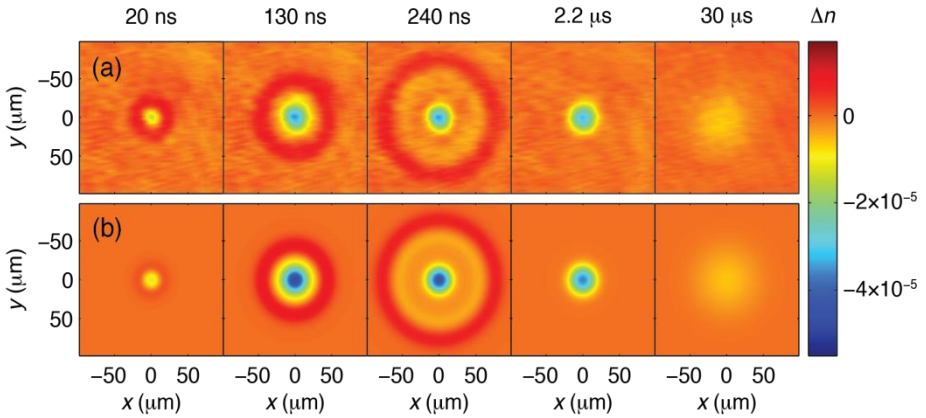

Figure 2.1 Gas dynamics following a single filament in air. (a) Interferometric measurement of the refractive index change following a short pulse as a function of the time delay of the probe pulse. (b) Hydrodynamic simulation, assuming a 60 μm FWHM Gaussian heat source of peak initial density 32 mJ/cm^3.

The full dynamics are now clearly seen in Figure 2.1(a), which presents new, higher time resolution measurements of the 2D density hole evolution (expressed as air refractive index shift) of a short air filament from nanoseconds through microseconds after filament formation. A 1D radial fluid code simulation, described in Section 2.9, is shown in Fig. 2.1(b) for comparison and the results are in excellent

agreement with the measurements. The transverse gas density profiles, shown in Fig. 2.1(b), were obtained using a 532 nm pulse as an interferometric probe of a single short ~2 mm filament, as shown in Figure 2.2. The short filament length is essential for minimizing refractive distortion of the interferometric probe pulse [50].

The experimental results verify that the density hole first deepens over tens of nanoseconds, and launches a sound wave which propagates beyond the ~200 μm frame by ~300 ns. By ~1-2 μs, pressure equilibrium is reached and the hole decays by thermal diffusion out to millisecond timescales. We note that at no probe delay do we see an on-axis refractive index enhancement that might act as a waveguiding structure and explain a recent report of filament guiding [51], an issue further discussed in ref. [52]. At the longer delays of tens of microseconds and beyond, the thermal gas density hole acts as a negative lens, as seen in our earlier experiments [49].

2.3. Experimental setup

The gas density measurements were performed using the setup shown in Fig. 2.2. A λ = 532 nm, 7 ns duration beam counter-propagates along a femtosecond filament structure generated by a 10 Hz Ti:Sapphire laser system producing λ = 800 nm, 50 fs pulses up to 100 mJ. Here, the 532 nm pulse serves as either a low energy interferometric probe of the evolving gas density profile, using a folded wavefront interferometer, or as an injection source for optical guiding in the gas density structure. The delay of the 532 nm probe/injection pulse is controlled with respect to the Ti:Sapphire pulse with a digital delay generator. The pulse timing jitter of <10 ns

is negligible given the very long timescale gas evolution we focus on. For the injection experiments, up to 110 mJ is available at 532 nm.

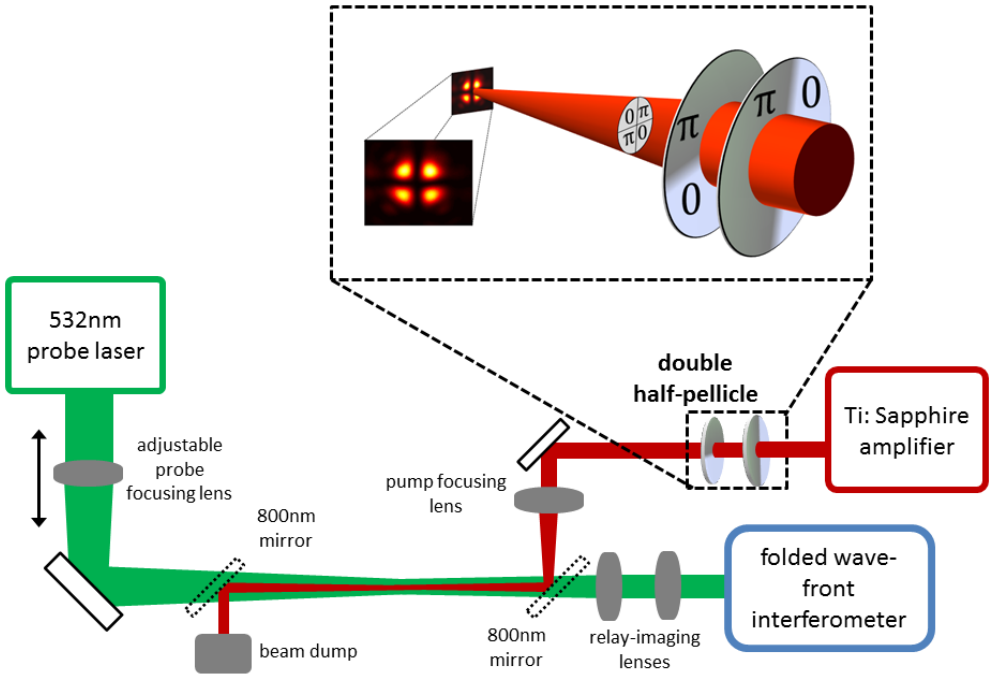

Figure 2.2 Generation of a filament array using half pellicles. A 55 fs, 800 nm, 10 Hz pulsed laser is used to generate an array of four filaments. A pulse propagates through two orthogonal half-pellicles, inducing π phase shifts on neighboring quadrants of the beam, and then are focused to produce a 4-filament with a TEM_{11} mode (actual low intensity image shown). A 7 ns, 532 nm 10 Hz pulsed laser counter-propagates through the filament and is imaged either directly onto a CCD for guiding experiments or through a folded wavefront interferometer and onto a CCD for interferometry.

2.4. Creation of multifilament guiding structure

Although a single filament results in a beam-defocusing gas density hole, a question arises as to whether a guiding structure can be built using the judicious placement of more than one filament. We tested this idea with a 4-lobed focal beam structure using two orthogonal 'half-pellicles'. As seen in Fig. 2.2, the pellicles are oriented to phase-shift the laser electric field as shown in each near-field beam

quadrant. Below the filamentation threshold, the resulting focused beam at its waist has a 4-lobed intensity profile as shown, corresponding to a Hermite-Gaussian TEM_{11} mode, where the electric fields in adjacent lobes are π phase shifted with respect to each other. Above the threshold, the lobes collapse into filaments whose optical cores still maintain this phase relationship and thus 4 parallel filaments are formed. As a demonstration of this, Figure 2.3 shows an image of the Rayleigh side-scattering at 800 nm from a 2-lobed filament produced by a single half pellicle, indicating that the π phase shift is preserved along the full length of the filament. This image was obtained by concatenating multiple images from a low noise CCD camera translated on a rail parallel to the filament. The images were taken through an 800 nm interference filter.

The bottom panel of Figure 2.3 shows burn patterns taken at multiple locations along the path of a ~70 cm long 4-lobe filament used later. For the 70 cm 4-filament, the filament core spacing is roughly constant at ~300 μm over a L ~ 50 cm region with divergence to ~1 mm at the ends.

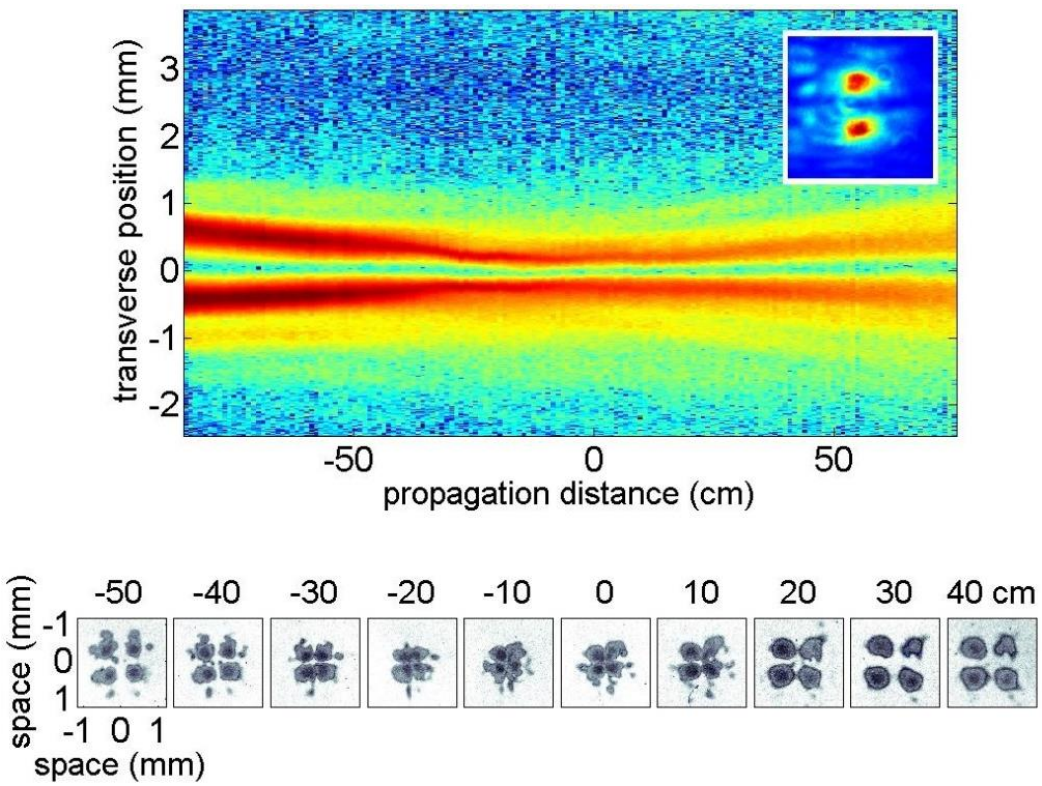

Figure 2.3 Rayleigh scattering as a function of *z* with a bi-filament produced by a single half pellicle (the bi-filament far-field mode is shown in inset). The bottom row shows burn patterns produced by a 4-filament produced by two orthogonal half pellicles.

The effect of a 4-filament structure on the gas dynamics is shown in Fig. 2.4, a sequence of gas density profiles measured for a short ~2 mm filament (produced at *f*/35) to minimize refractive distortion of the probe beam. The peak intensity was $<10^{14}$ W/cm^2, typical of the refraction-limited intensity in more extended filaments, so we expect these images to be descriptive of the gas dynamics inside much longer filaments. Inspection of the density profiles shows that there are two regimes in the gas dynamical evolution which are promising for supporting the guiding of a separate injected laser pulse. A shorter duration, more transient *acoustic regime* occurs when the sound waves originating from each of the four filaments superpose at the array's geometric center, as seen in panel (a) of Fig. 2.4, causing a local density enhancement

of approximately a factor of two larger than the sound wave amplitude, peaking ~80 ns after filament initiation and lasting approximately ~50 ns. A far longer lasting and significantly more robust profile suitable for guiding is achieved tens of microseconds later, well after the sound waves have propagated far from the filaments. In this *thermal regime*, the gas is in pressure equilibrium [49]. As seen in panels (c) and (d) of Fig. 2.4, thermal diffusion has smoothed the profile in such a way that the gas at center is surrounded by a 'moat' of lower density. The central density can be very slightly lower than the far background because its temperature is slightly elevated, yet it is still higher than the surrounding moat. The lifetime of this structure can be several milliseconds. In both the acoustic and thermal cases, the diameter of the air waveguide "core" is approximately half the filament lobe spacing. A movie of the 4-filament-induced gas evolution is provided in the supplementary material of our previously published findings [30].

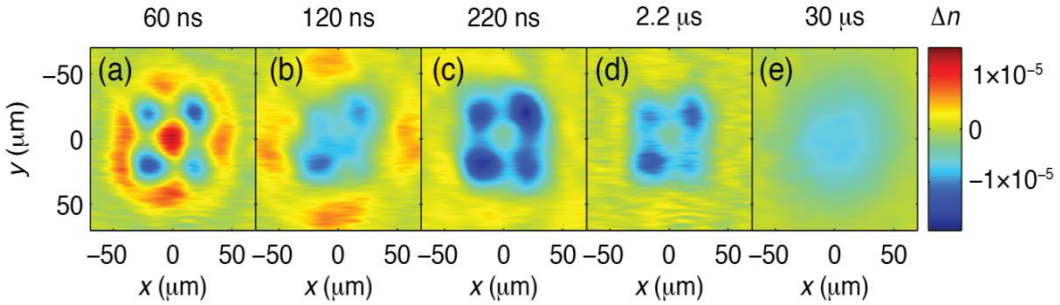

Figure 2.4 Interferometric measurement of the air density evolution induced by a 4-filament. (a) The acoustic waves generated by each filament cross in the middle, generating a positive index shift, producing the *acoustic guide.* (b) The acoustic waves propagate outward, leaving behind a density depression at the location of each filament. (c) The density depressions produce the *thermal guide*, with a higher central density surrounded by a moat of lower density. (d,e) The density depressions gradually fill in as the thermal energy dissipates. A movie of the 4-filament-induced gas evolution is provided in the supplementary material of our previously published findings [30].

2.5. Fiber analysis of the air waveguide

Having identified two potential regimes for optical guiding, a short duration acoustic regime, and a much longer duration thermal regime, it is first worth assessing the coupling and guiding conditions for an injected pulse. We apply the fibre parameter V for a step index guide [53] to the air waveguide, $V = (2\pi a/\lambda)(n_{co}^2 - n_{cl}^2)^{1/2} \sim (2\sqrt{2}\pi a/\lambda)(\delta n_{co} - \delta n_{cl})^{1/2}$, where the effective core and cladding regions have refractive indices $n_{co,cl} = n_0 + \delta n_{co,cl}$, n_0 is the unperturbed background air index, $n_0 - 1 = 2.77\text{x}10^{-4}$ at room temperature and pressure [54]), δn_{co} and δn_{cl} are the (small) index shifts from background at the core and cladding, and the core diameter is $2a$, taken conservatively at the tightest spacing of the filament array. The numerical aperture of the guide is $\text{NA} = \lambda V/(2\pi a)$. Because accurate density profile measurements are restricted to short filaments, we use the results of Fig. 2.4 and apply them to much longer and wider-lobe-separated filaments that are inaccessible to longitudinal interferometry owing to probe refraction. As typical filament core intensities are restricted by refraction ('intensity clamping') to levels $<10^{14}$ W/cm^2 [15], we expect that the measurements of Fig. 2.4 apply reasonably well to longer filaments and different lobe spacings. For the acoustic guide, we used a filamenting beam with lobe spacing of 150 μm, so $2a$ ~ 75 μm. Using $\delta n_{co}/(n_0 - 1) \sim 0.05$, and $\delta n_{cl}/(n_0 - 1) \sim -0.02$ from Fig. 2.4 then gives V ~ 2.8 (> 2.405) and NA ~ 6.3×10^{-3}, indicating a near-single mode guide with an optimum coupling f-number of $f/\#$ =0.5 / NA ~ 80. For the long thermal guide, we used a filamenting beam with lobe spacing of ~300 μm, so $2a$ ~ 150 μm. From Fig. 2.4, the

core index shift is $\delta n_{co} \sim 0$ and the cladding shift is the index decrement at the moat, $\delta n_{cl} / (n_0 - 1) \sim -0.02$, giving $V \sim 2.9$, corresponding to a near-single mode guide with $NA \sim 3.2 \times 10^{-3}$, corresponding to $f/\# \sim 160$.

2.6. Discussion of experimental results

Using the experimental setup shown in Figure 2.2, an end mode image from injection and guiding of a low energy λ = 532 nm pulse in the acoustic waveguide produced from a 10 cm long 4-filament is shown in Fig. 2.5. In order to differentiate between guiding and the propagation of the unguided beam through the fully dissipated guide at later times (>2 ms) we define the guiding efficiency as $\left(E_g - E_{ug}\right) / \left(E_{tot} - E_{ug}\right)$ where E_g is the guided energy within the central mode, E_{tot} is the total beam energy and E_{ug} is the fraction of energy of the unguided mode occupying the same transverse area as the guided mode.

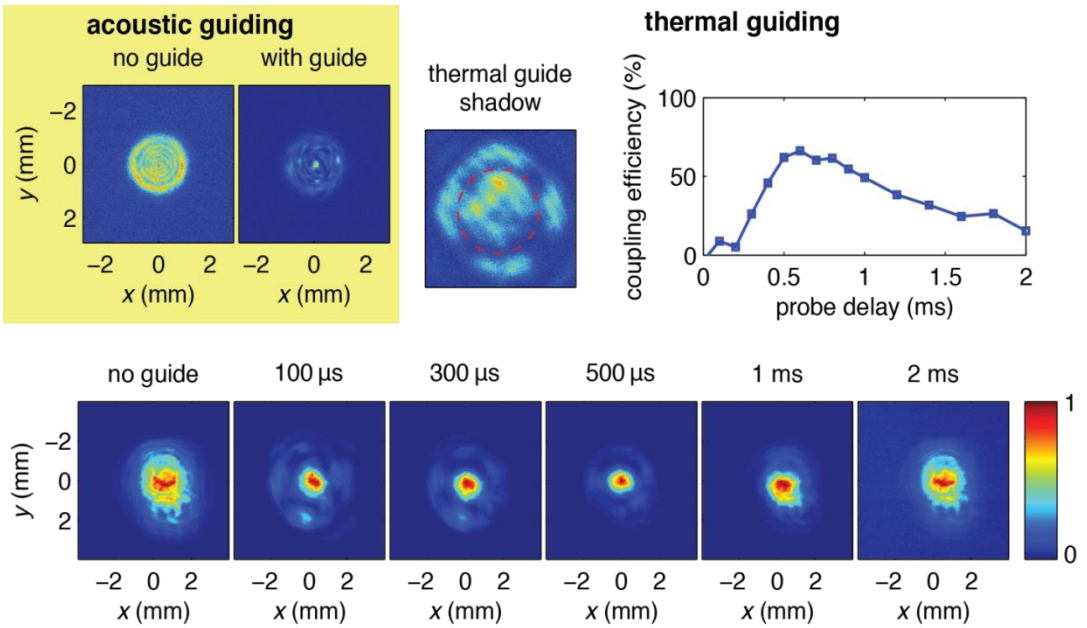

Figure 2.5 Demonstration of guiding of 7 ns, λ = 532 nm pulses in 70 cm long acoustic and thermal air waveguides produced by a 4-filament. The panel in the upper left shows the probe beam, which is imaged after the filamentation region, with and without the filament. The time delay of the probe was 200 ns, which is in the acoustic guiding regime. The effect of the thermal waveguide, the shadow of which can be seen in the image in the top center (with a red dashed circle showing the position of the lower density moat), is shown in the bottom row, where the probe beam is imaged after the exit location of the air waveguide with and without the filamenting beam. The coupling efficiency vs. injected pulse delay is shown in the upper right. Peak energy guided was ~110 mJ.

The best coupling in the acoustic regime occurred at an injection delay of ~200 ns and *f*/# >100, with a peak guided efficiency of 13%, although the guides were not stable on a shot-to-shot basis. Efficient guiding in the acoustic regime takes place over an injection delay interval of only ~100 ns, consistent with the time for a sound wave to cross the waveguide core region, a/c_s ~ 100 ns, where $2a$ = 75µm and $c_s \sim 3.4\text{x}10^4$ cm/s is the air sound speed [55]. We found that for longer filaments with wider lobe spacings, the acoustic guides were even less stable. Unless the 4-filament lobes were well balanced in energy and transverse position, the sound wave superposition would not form a well-defined air waveguide core. This is why a shorter 10 cm filament was used for the acoustic guide experiment. While the

acoustic superposition guide is a promising approach, future experiments will need filaments generated by very well-balanced multi-lobe beam profiles, an example of which is seen in ref. [52].

By comparison, the thermal guides were far more robust, stable, and long-lived. Results from the thermal guide produced by a 70 cm long 4-filament are also shown in Fig. 2.5, where optimal coupling was found for *f/#* = 200, in rough agreement with the earlier fibre-based estimate. An out of focus end mode image (not to scale) is shown to verify the presence of the thermal guide's lower density moat. Here we note that owing to the much greater lobe spacing of its long 4-filament, the thermal guide of Fig. 2.5 lasts much longer (milliseconds) than that from the short 4-filament of Fig. 2.4 (~10 μs). Guided output modes as function of injection delay are shown imaged from a plane past the end of the guide, in order to minimize guide distortion of the imaging. These mode sizes are larger than upstream in the guide where 4-filament lobe spacing is tighter, but where we are unable to image reliably. We injected up to 110 mJ of 532 nm light, the maximum output of our laser, with 90% energy throughput in a single guided mode. This corresponds to a peak guiding efficiency of 70%. Guiding efficiency vs. injected pulse delay is plotted in Fig. 2.5. As seen in that plot, peak guiding occurs at ~600 μs and persists out to ~2 ms where the guiding efficiency drops to ~15%. Based on the guide core diameter of $2a$ ~ 150 μm and the portion of the filament length with constant lobe spacing, L ~ 50 cm, the guided beam propagates approximately $L\lambda/(\pi a^2)$ ~ 15 Rayleigh ranges. A movie of the thermal waveguide output beam, during real time rastering (at 10 Hz) of the injected beam

across the guide entrance, is shown in the supplementary material of our previously published work [30].

2.7. Simulations of waveguide development and guiding

Owing to the linearity of the heat flow problem, the evolution of the 4-filament-induced density structure in the thermal regime can be calculated by finding the solution $T(x,y,t)$ to the 2D heat flow equation, $\partial T / \partial t = \alpha \nabla^2 T$, for a single filament source located at $(x, y) = (0, 0)$ and then forming $T_4(x, y, t) = \sum_{j=1}^{4} T(x - x_j, y - y_j, t)$, where (x_j, y_j) are the thermal source locations in the 4-filament. Here $\alpha = \kappa / c_p$, where κ and c_p are the thermal conductivity and specific heat capacity of air. To excellent approximation, as shown in ref. [49], $T(x,y,t)$ is Gaussian in space. Invoking pressure balance, the 2D density evolution is then given by $\Delta N_4(r,t) = -N_b \frac{\Delta T_0}{T_b}\left(\frac{R_0^2}{R_0^2 + 4\alpha t}\right)\sum_{j=1}^{4} exp\left(\frac{-\left(x - x_j\right)^2 - \left(y - y_j\right)^2}{R_0^2 + 4\alpha t}\right)$, where R_0 is the initial $1/e$ radius of the temperature profile of a single filament and ΔT_0 is its peak value above T_b, the background (room) temperature. Using $R_0 = 50$ μm , $\Delta T_0 = 15$K , $\alpha = 0.21$ cm^2/s for air [49], and source locations separated by 500 μm, approximating our 70 cm 4-filament, gives the sequence of gas density plots shown in the upper panels of Fig. 2.6, clearly illustrating the development and persistence of the guiding structure over milliseconds.

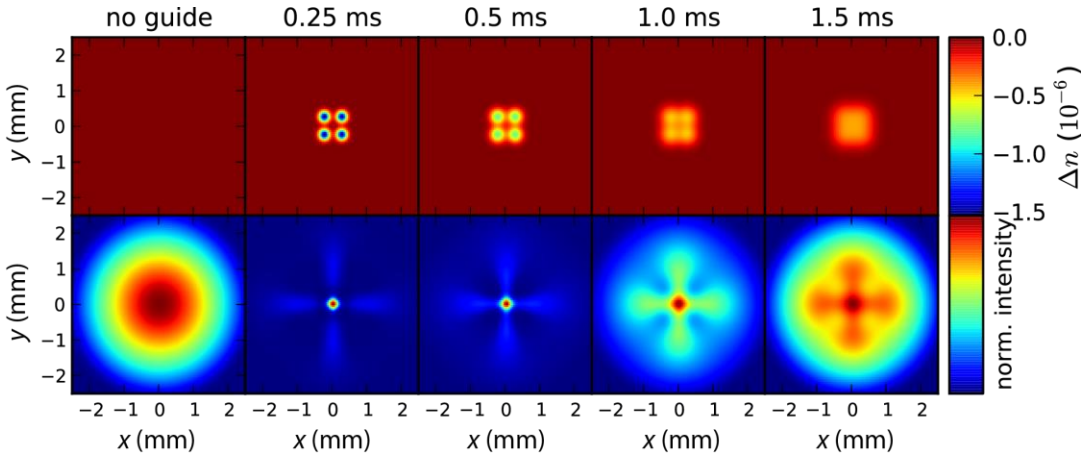

Figure 2.6 Simulation of the evolution of and guiding in a thermal air waveguide. The top row shows the index of refraction shift produced by the 4-filament-induced temperature profile as a function of time. The bottom row shows a BPM simulation of the guided laser beam profile at the end of a 70 cm waveguide produced by the 4-filament-induced refractive index change.

The propagation of the 532 nm beam in the waveguide was simulated in the paraxial approximation using the beam propagation method (BPM) [56]. The calculated intensity at the output of the waveguide is shown in the lower panels of Fig. 2.6. At early delays <100 μs, characteristics of a multimode waveguide are observed in the simulation, including mode beating. At later times, as the refractive index contrast decreases, the propagation is smoother, indicating single mode behaviour, consistent with the estimates in Section 2.5 using the fibre parameter. The simulation is in reasonable agreement with the experimental results. Axial nonuniformity in the waveguiding structure could explain the absence of four fold symmetry in the experimental data, whereas it is pronounced in the simulations.

2.8. Discussion of future long-range guiding possibilities

We have demonstrated the generation of very long-lived and robust optical waveguides in air, their extent limited only by the propagation distance of the initiating femtosecond filament array and the axial uniformity of its energy deposition. Assuming a sufficiently uniform filament, this is ultimately determined by the femtosecond pulse energy absorbed to heat the gas. Based on a single filament diameter of ~100 μm, an electron density of ~3×10^{16} cm^{-3} [16], ionization energy of ~10 eV per electron, and 5 meV of heating per air molecule [49], approximately 0.5 mJ is needed per metre of each filament. Detailed measurements of the magnitude of energy deposition into air for the case of single filaments launched with a variety of initial pulse parameters are also presented in Chapter 5. With a femtosecond laser system of a few hundred millijoules pulse energy, waveguides hundreds of meters long are possible.

What is the optical power carrying capacity of these guides? For ~10 ns pulses of the type used here for waveguide injection, the peak energy is limited by an ionization threshold of 10^{13} W/cm^2 to ~20 J for our 150 μm core diameter (the self-focusing threshold in air for 10 ns pulses is P_{cr} ~4 GW [3] or ~40 J). However, the real utility of these air waveguides, in the thermal formation regime, derives from their extremely long millisecond-scale lifetime. This opens the possibility of guiding very high average powers that are well below the ionization threshold.

2.8.1. Thermal blooming

We now consider the robustness of our filament-induced waveguides to thermal blooming [37], [57] from molecular and aerosol absorption in the atmosphere. For thermal blooming, we consider the deposited laser energy which can raise the local gas temperature by a fraction η of ambient, $P_g \Delta t / A = 1.5 \eta \alpha^{-1} p$, where P_g is the guided laser power, Δt is the pulse duration, α is the absorption coefficient, A is the waveguide core cross sectional area, and p is the ambient pressure. Thermal blooming competes with guiding when η is approximately equal to the relative gas density difference between the core and cladding. In our measurements of the thermal air waveguide, the typical index (and density) difference between the core and cladding is of the order of ~2% at millisecond timescales. Taking η = 0.02, p = 1 atm, and $\alpha = 2\text{x}10^{-8}$ cm^{-1} [37], gives $P_g \Delta t / A < \sim 1.5\text{x}10^{5}$ J/cm^2 as the energy flux limit for thermal blooming. For example, for a 1.5 mm diameter air waveguide core formed from an azimuthal array of filaments, the limiting energy is $P_g \Delta t \sim 2.7$ kJ. Note that we use a conservative value for α at λ ~ 1 μm which includes both molecular and aerosol absorption for maritime environments [37], which contain significantly higher aerosol concentrations than dry air. If a high power laser is pulsed for Δt ~ 2 ms, consistent with the lifetime of our 10 Hz-generated thermal waveguides, the peak average power can be 1.3 MW. It is possible that in such environments, air heating by the filament array itself could help dissipate the aerosols before the high power beam is injected, raising the thermal blooming threshold and also reducing aerosol scattering. An air waveguide even more robust against thermal blooming and capable

of quasi-continuous operation may be possible using a kHz repetition rate filamenting laser. We have already shown that the cumulative effect of filamenting pulses arriving faster than the density hole can dissipate leads to steady state hole depths of order ~10% [49].

2.9. Simulation of gas hydrodynamic evolution

The simulations of the gas hydrodynamic evolution presented in Figure 2.1 and Figure 2.6 are performed in cylindrical geometry using a one-dimensional Lagrangian one-fluid hydrocode, in which the conservation equations for mass, momentum and energy, $\partial\xi_i / \partial t + \nabla \cdot (\xi_i \mathbf{v} + \phi_i) = \mathrm{S}_i$ were solved numerically. For the mass equation, $\xi_1 = \rho$ and $\phi_1 = 0$, for the momentum equation, $\xi_2 = \rho\mathbf{v}$ and $\phi_2 = P\vec{\vec{\mathbf{I}}}$ (where $\vec{\vec{\mathbf{I}}}$ is the unit tensor), and for the energy equation, $\xi_3 = \varepsilon + \frac{1}{2}\rho\mathbf{v}^2$ and $\phi_3 = P\mathbf{v} + \mathbf{q}$. Here, ξ is the volume density of the conserved quantity, ϕ is the flux of that quantity, and S refers to sources or sinks, while ρ is mass density, ε is fluid internal energy density, $\mathbf{v}$ is fluid velocity, P is gas pressure, and $\mathbf{q} = -\kappa\nabla T$ is the heat flux, where κ and T are the gas thermal conductivity and temperature. The radiation of the heated gas contributes negligibly to the energy balance, as can be verified by assuming the maximum emission of a black body and finding it to be tiny. At all times, $S_1 = S_2 = 0$ by mass and momentum conservation, but without approximations, $S_3 \neq 0$ because the thermal part of the energy density is changed by laser heating and by ionization/recombination of all the relevant species in the gas. However, we

recognize that at times > ~10 ns after laser filament excitation, all of the energy initially stored in free electron thermal energy and in the ionization and excitation distribution is repartitioned into a fully recombined gas in its ground electronic state. The 'initial' radial pressure distribution driving the gas hydrodynamics at times > 10 ns is set by the initial plasma conditions $P_0(r) \approx (f_e / f_g) N_e(r) k_B T_e(r)$ where k_B is Boltzmann's constant, $N_e(r)$ and $T_e(r)$ are the initial electron density and electron temperature profiles immediately after femtosecond filamentation in the gas, and f_e and f_g are the number of thermodynamic degrees of freedom of the free electrons and gas molecules. Here, f_e = 3, and f_g = 5 for air at the temperatures of this experiment (ΔT_0 < 100K). To simulate the neutral gas response at long timescales we solve the fluid equations for the ξ_i, using $S_3 = 0$ and the initial pressure profile given by $P_0(r)$ above.

Chapter 3: Collection of remote optical signals using air waveguides

3.1. Overview and motivation

In optical stand-off detection techniques, spectroscopic or other light-based quantitative information is collected from a distance. While the air waveguide concept presented in Chapter 2 demonstrated the ability to guide separately injected laser light from a source location towards a distant target, such a refractive index structure is also capable of carrying remotely generated light back towards a detector. In this chapter, we demonstrate that femtosecond filament-generated air waveguides can collect and transport remotely-generated optical signals while preserving the source spectral shape. The air waveguide acts as an efficient standoff lens. Here, we demonstrate collection of an isotropically emitted optical signal, the worst case scenario in terms of collection efficiency. Even stronger collection enhancement would apply to directional signals from stimulated backscattering [58] or backward lasing [38]. Our results have immediate impact on remote target applications of laser-induced breakdown spectroscopy (LIBS) [59] and on LIDAR studies [39]. Our proof of principle experiment tests ~1 m long air waveguides of various configurations, in both the acoustic and thermal regimes. Extrapolation of our results to >100 m waveguides generated by extended filamentation [15], [60], [61] implies potential signal-to-noise enhancements greater than $\sim 10^4$. Of course, demonstration of sufficiently uniform filament energy deposition will need to be demonstrated over such distances.

3.1.1. Laser induced breakdown spectroscopy

The ability to deliver high peak intensities at relatively long distances has been applied to LIDAR [39] and LIBS [59], and other remote sensing schemes [38], [41]. In remote LIBS, as a specific example, laser-breakdown of a gas or solid target of interest generates a characteristic line spectrum that allows identification of target constituents. However, as the optical emission from the target is isotropic with a geometrical R^{-2} falloff with source distance, very little of the signal is collected by a distant detector, necessitating large numerical aperture collection optics and high gain detectors [59]. Schemes to increase the LIBS signal by increasing the plasma temperature and/or density have been proposed, such as use of double pulses [62], but all such methods are still subject to the geometrical factor. Some recent schemes for optical stand-off detection use femtosecond filamentation.

3.2. Experimental setup

Figure 3.1 illustrates the experimental setup. Single filaments and filament arrays 75-100 cm long are generated in air using 10 Hz Ti:Sapphire laser pulses at 800 nm, 50-100 fs, and up to 16 mJ. The beam focusing is varied between *f*/400 and *f*/200 depending on the type of guide. Arrays with four or eight filaments are generated by phase shifting alternating segments of the beam's near field phase front by π. As described in Chapter 2, four-filament arrays, or quad-filaments, are generated using two orthogonal "half-pellicles" [30], and 8-filament arrays, or octo-filaments, are generated using eight segment stepped mirrors [52], resulting in either a TEM_{11}-like

mode or a linear combination of $LG_{0,\pm4}$ modes in the low intensity beam focus, as seen in insets (b) and (c) of Fig. 3.1.

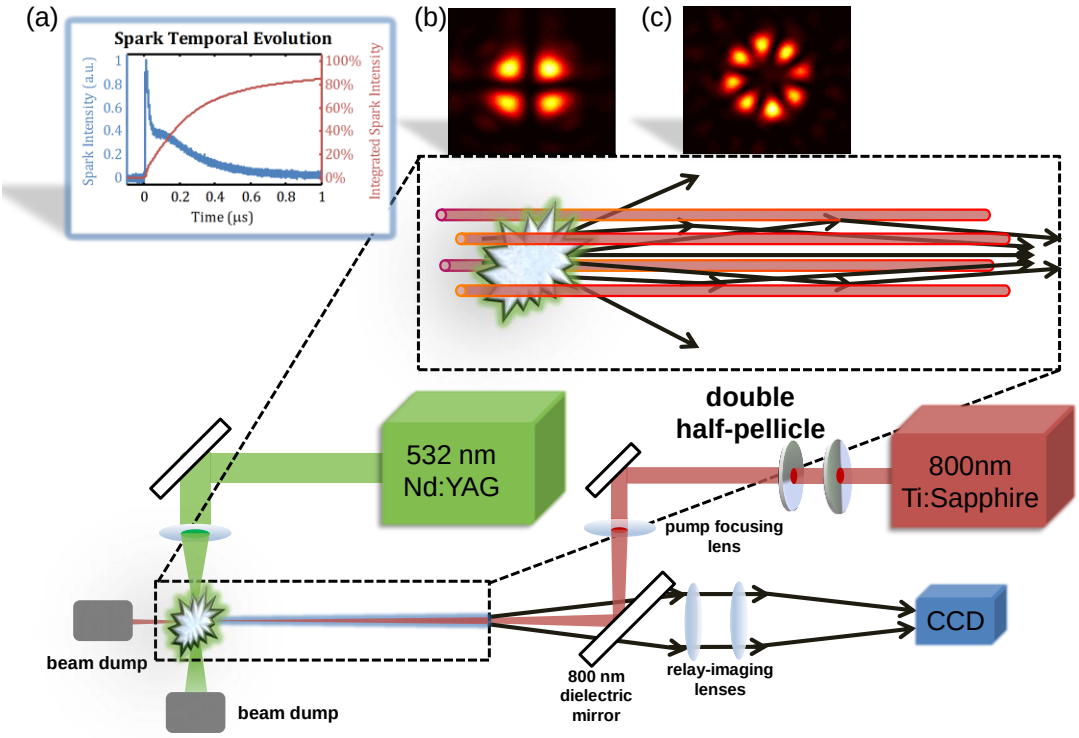

Figure 3.1 Experimental setup for demonstration of light collection and transport by the air waveguide. Insets: (a) Time evolution of the spectrally integrated emission of the spark (blue curve) and its running integral (red curve). (b) Low intensity image of the 4 lobe beam focus generated by orthogonal half pellicles (shown). (c) Low intensity image of the 8 lobe beam focus generated by the segmented mirror (not shown).

Above the self-focusing threshold, the beam lobes collapse into parallel and distinct filaments [30], [52]. By inserting burn paper into the paths of the quad- and octo-filaments [30], we have verified that their 4 or 8 lobe character is preserved through the whole propagation path. As detailed in the previous chapter, colliding acoustic waves at the array center launched by either quad-filaments or octo-filaments form waveguides of duration ~1 μs, roughly corresponding to the acoustic wave

transit time through the array center. Millisecond lifetime waveguides develop during the slow post-acoustic thermal diffusion of the density holes left by the filaments [30].

3.3. Guiding of plasma emission from laser breakdown sparks in air

We tested the signal collection properties of our waveguides using an isotropic, wide bandwidth optical source containing both continuum and spectral line emission, provided by tight focusing at *f*/10 of a 6 ns, 532 nm, 100 mJ laser pulse to generate a breakdown spark in air. Time evolution of the spectrally integrated spark emission is shown in Fig. 3.1(a), where the scattered 532 nm signal has been filtered out. The signal FWHM is ~35 ns, with a long ~1 μs decay containing >85% of the emission. The air spark laser and the filament laser are synchronized with RMS jitter <10 ns. The delay between the spark and the filament structure is varied to probe the time-evolving collection efficiency of the air waveguides. The air spark and filament beams cross at an angle of 22°, so that the spark has a projected length of ~500 μm transverse to the air waveguide. As depicted in Fig. 3.1, the spark is positioned just inside the far end of the air waveguide. Rays from the source are lensed by the guide and an exit plane beyond the end of the guide is imaged through an 800 nm dielectric mirror onto a CCD camera or the entrance slit of a spectrometer. This exit plane is located within 10 cm of the end of the waveguide.

3.4. Source collection enhancement and peak signal enhancement

The collected signal appears on the CCD image as a guided spot with a diameter characteristic of the air waveguide diameter. Guided spots are shown in Fig. 3.2 for five types of air waveguide: the quad-filament and octo-filament waveguides in both the acoustic and thermal regimes, and the single filament annular acoustic guide. Surrounding the guided spots are shadows corresponding to the locations of the gas density depressions, which act as defocusing elements to scatter away source rays. We quantify the air waveguide's signal collecting ability using two measures. The peak signal enhancement, η_1, is defined as the peak imaged intensity with the air waveguide divided by the light intensity without it. We define the source collection enhancement, η_2, as the integrated intensity over the guided spot, divided by the corresponding amount of light on the same CCD pixels in the absence of the air waveguide. Figure 3.3 shows plots of η_1 and η_2 for each of our waveguide types as a function of time delay between the spark and filament laser pulses. Inspection of Fig. 3.1(a) shows that ~70% of the spark emission occurs before 500 ns, so the evolution of the peak signal and collection enhancements are largely characteristic of the waveguide evolution and not the source evolution. The spot images shown in Fig. 3.2 are for time delays where the collection efficiency is maximized for each waveguide. In general, we find $\eta_1 > \eta_2$ because the peak intensity enhancement is more spatially localized than the spot.

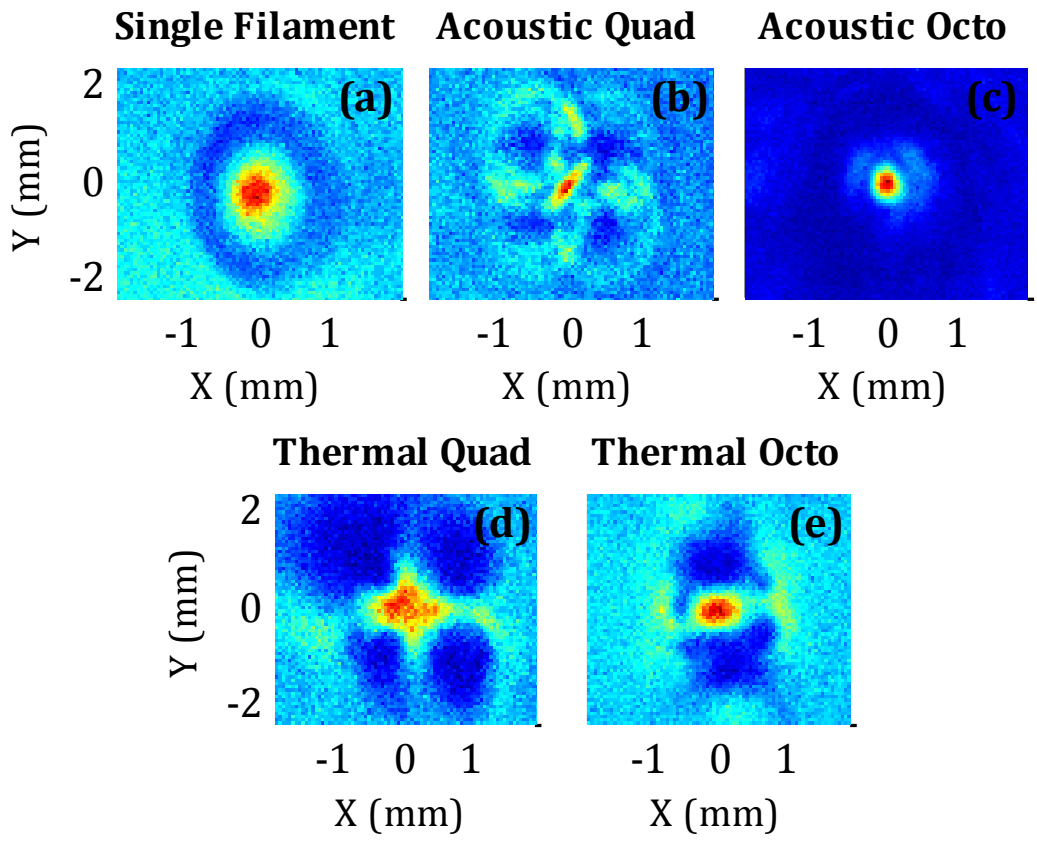

Figure 3.2 Single shot images of the breakdown spark light emerging from the exit of the guiding structures. (a) Single filament-induced guide at 1.2 μs. (b) Four-lobed acoustic guide at 3.2 μs, (c) Eight-lobed acoustic guide at 1.4 μs, (d) Four-lobed thermal guide at 250 μs, (e) Eight-lobed thermal guide at 100 μs.

Figures 3.2 and 3.3 illustrate the acoustic and thermal regimes of guiding discussed earlier. Figures 3.2(b) and (c) (and Fig. 3.3(b) and (c)) illustrate microsecond-duration acoustic guiding in the waveguide formed by colliding sound waves from quad and octo-filaments, while Figs. 3.2(d) and (e) (and Figs. 3.3(d) and (e)) illustrate the much longer duration thermal guiding from waveguide structures enabled by quad- and octo- density holes. The plots of peak and collection enhancement for the thermal guides show an almost 2 ms long collection window, ~10^3 times longer than for the acoustic guides. For a single filament (Fig. 3.2(a)) and 3(a)), we also see source light trapping in a window ~1 μs long, where trapping

occurs in the positive crest of the single cycle annular acoustic wave launched in the wake of the filament [52]. Here, the trapping lifetime is constrained by the limited temporal window for source ray acceptance as the acoustic wave propagates outward from the filament.

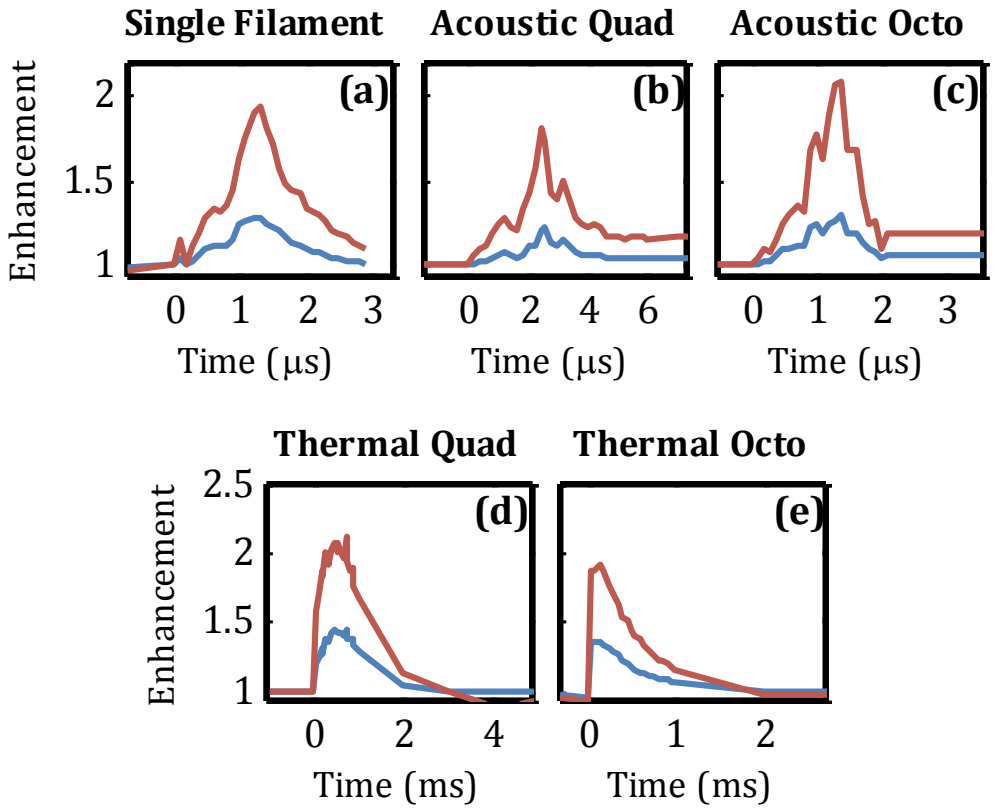

Figure 3.3 Source collection enhancement (blue) and peak signal enhancement (red) plotted vs. filament - spark source delay for (a) single filament acoustic guide, (b) four-lobed acoustic guide, (c) eight-lobed acoustic guide, (d) four-lobed thermal guide, and (e) eight-lobed thermal guide.

For each of the guides we observe peak signal enhancement in the range $\eta_1 \sim 1.8-2$, and source collection enhancement $\eta_2 \sim 1.3-1.5$. (Fig. 3.2(a-e) and Fig. 3.3 (a-e)). For a waveguide numerical aperture of $\mathrm{NA} = \sqrt{2}(\delta n_{co} - \delta n_{cl})^{1/2}$ [30],

where δn_{co} and δn_{cl} are the shifts in the air waveguide core and cladding refractive indices relative to undisturbed ambient air, the source collection enhancement is

$$\eta_2 = 4(\mathrm{NA})^2 \left(\frac{a_{in}}{w} \right)^2 \left(\frac{L}{a_{out}} \right)^2 \alpha \qquad (3.1)$$

where L is the waveguide length, a_{in} and a_{out} are the mode diameters for the waveguide at the spark source and the output respectively, w is the greater of the source diameter d_s and a_{in}, and α is a transient loss coefficient computed from a beam propagation method (BPM) [56] simulation (see below). For our octo-thermal guide we used burn paper to characterize the transverse profile of the guide, and a microphone [52] to measure the axial extent. Similar to previous experiments [30], we find the mode diameter to be roughly half the lobe spacing. Parameters for the octo-thermal guide are $NA \sim 2.5 \cdot 10^{-3}$, L = 1 m, a_{in} = 0.5 mm, a_{out} = 1.5 mm, d_s = 0.5 mm, and α = 0.28, resulting in η_2 = 3, which is in reasonable agreement with our measured η_2 = 1.4. Although the signal enhancement is modest for our meter-scale filament, the scaling $\eta_2 \propto L^2$ would enable a ~10^4 collection enhancement by a 100 m air waveguide.

3.5. Beam propagation method simulation of source collection enhancement

For the BPM simulation, we used a paraxial portion of a spherical wave to simulate rays from a point source lensed by an eight-lobed thermal index structure

with peak index shift consistent with the NA used above. Faster than exponential losses are observed over the first meter as the lossiest leaky modes radiate out of the guide, factored into Eq. (3.1) through α as discussed above. Extending the propagation simulation from ~1 to 100 m for either a constant or linearly tapered transverse profile (doubling over 100 m) gives similar results, showing that beyond 1 m, the losses transition to weakly exponential for the few weakly leaky modes remaining. After transient losses over the first meter, only 25% of the signal is lost over the remaining ~99 m of transit, preserving the L^2 efficiency scaling. These results do not account for absorption in air.

3.6. High fidelity transmission of spectral content through the air waveguide

Crucial to remote sensing schemes is identification of source chemical composition, which is typically done by identifying characteristic spectral lines of neutral atoms or ions of a given species. For such schemes, it is important that the emission spectrum at the source location be conveyed with high fidelity to the remote detector location. To investigate this property of our air waveguide, we compared spectra measured 10 cm from the air spark source to spectra of the guided signal collected from the output of the air waveguide. The results are shown in Fig. 3.4, for a thermal waveguide from a quad-filament, where the spectra have been averaged over 100 shots. There is no significant difference in the spectra except for attenuation in the range 700-900 nm owing to signal transmission through a broadband 800 nm dielectric mirror, as depicted in Fig. 3.1, and the onset of UV absorption at less than

~350 nm due to absorption by the BK7 substrate of the same mirror and in the following BK7 lenses. In addition to characteristic nitrogen emission lines identified in Fig. 3.4, a very strong scattering peak is seen at 532 nm from the spark laser, with the spectral peak extending well past the range of the plot's vertical axis.

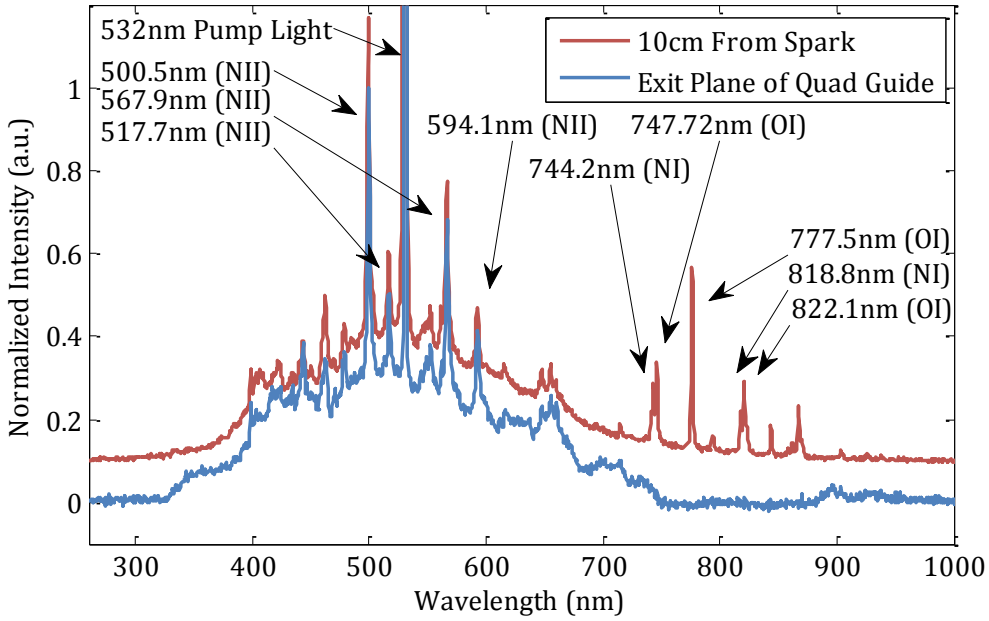

Figure 3.4 Air-spark spectrum collected near the source (red curve) and after transport in a 75 cm air waveguide (thermal guide from a quad-filament, blue curve). Characteristic lines are indicated on the spectrum. The red curve is raised for clarity. (Spectrometer: Ocean Optics HR2000+)

3.7. Concluding remarks

In conclusion, we have demonstrated that a femtosecond filament-generated air waveguide can be used as a remote broadband collection optic to enhance the signal in standoff measurements of remote source emission. This provides a new tool for dramatically improving the sensitivity of optical remote sensing schemes. By employing air waveguides of sufficient length, the signal-to-noise ratio in LIDAR and remote LIBS measurements can be increased by many orders of magnitude. Finally,

we emphasize that air waveguides are dual purpose: not only can they collect and transport remote optical signals, but they can also guide high peak and average power laser drivers to excite those sources, as demonstrated in Chapter 2.

Chapter 4: Sensitivity of propagation and energy deposition to nonlinear refractive index

4.1. Introduction and motivation

Since the laser-induced atomic/molecular nonlinearity is responsible for the onset of filamentation and its sustainment, accurate coefficients are needed for modeling the nonlinear response in propagation models. Modeling and interpretation of experiments in filament-based applications such as long range propagation [36], high harmonic generation [63], and ultrashort pulse shaping and supercontinuum generation [22], [23], depend on an accurate representation of the nonlinearities. Many indirect measurements of the nonlinear response have appeared in the literature, with the aim of extracting coefficients such as n_2, the nonlinear index of refraction or Kerr coefficient [3]. Such indirect measurements include spectral analysis after nonlinear propagation [8], [64], spatial profile analysis [7], polarization rotation by induced birefringence [65]**,** and spectral shifts of a probe pulse [66]. As an example, extracted n_2 values for the major constituents of air, N_2 and O_2, show a range of variation exceeding ~100%. Some of this variation might be attributed to nonlinear 3D propagation effects [64], [66], unintentional two-beam coupling in degenerate pump-probe experiments owing to the presence of laser-induced Kerr, plasma, and rotational gratings [66]–[69], and the laser pulsewidth dependence of the nonlinear response, which had not been *directly* resolved [7], [8], [64], [67]. Depending on the repetition rate of the laser, thermal changes in the gas density could also lead to an effective lowering of the nonlinearity observed in the experiment [49].

In this chapter, we explore the sensitivity of femtosecond filamentation in air to the nonlinear response of the constituent molecules. Experiments are performed with varying laser pulse energy, pulsewidth and focusing *f*-number, and filaments are diagnosed along their propagation path by evaluating the local energy density absorbed from the laser. The measurements are compared to laser propagation simulations in which the nonlinear coefficients pertaining to the instantaneous part of the response, namely the nonlinear indices of refraction n_2 for N_2 and O_2, are varied. We find sensitive dependence on the choices for n_2, with the best fit to experimental results obtained by using the values measured in [1]. For this sensitivity test, we focus on the instantaneous rather than the delayed response because of the prior wide variability in measured n_2, as displayed in Table 4.1. Our goal is to clearly demonstrate that accurate propagation simulations of high power femtosecond pulses depend sensitively on accurate values for the nonlinear response.

4.2. Summary of nonlinear refractive index measurements

At optical frequencies the electronic response, responsible for the Kerr effect, is nearly instantaneous on femtosecond time scales, while the response from molecular alignment is delayed owing to the molecular moment of inertia and depends strongly on the laser pulse duration [1], [17], [70]. The combined response can be expressed, to second order in the laser electric field, as a transient refractive index shift at a point in space,

$$\Delta n(t) = n_2 I(t) + \int_{-\infty}^{\infty} R(t-t')I(t')dt' \qquad (4.1)$$

where $I(t)$ is the laser intensity, R is the rotational Raman response function, and the first and second terms describe the instantaneous electronic and delayed rotational response. Experiments that use pulses longer than a few hundred femtoseconds [7], [8] cannot distinguish the electronic from rotational response, making such results of limited use for understanding the propagation of ultrashort pulses. Even experiments using pulses that are 90-120 fs [64], [66], [67], [70], [71] are barely able to distinguish the two. Recently, the optical nonlinear response for a range of noble and molecular gases was absolutely measured using single-shot supercontinuum spectral interferometry (SSSI) using 40 fs pump pulses [1], [17], [18]. This measurement technique enabled accurate determination of the separate instantaneous and delayed contributions to the total response. A remarkable additional aspect of the measurements [1], [17], [18] is that the instantaneous part of the response is seen to be linear in the intensity envelope well beyond the perturbative regime all the way to the ionization limit of the atom or molecule. Thus, the n_2 values measured in [1], [18] are valid over the full range of intensities experienced by atoms or molecules in the filament core.

	n_2 (10^{-19} cm^2/W)						$\Delta\alpha$ (10^{-25} cm^3)
	Wahlstrand *et al.* [1] (40 fs)	Nibbering *et al.* [64] (120 fs)	Loriot *et al.* [67] (90 fs)	Börzsönyi *et al.* [72] (200 fs)	Bukin *et al.* [73] (39 fs)	Shelton and Rice [2]	Wahlstrand *et al.*[1]
Air	0.78		1.2	5.7 ± 2.5	3.01		
N_2	0.74 ± 0.09	2.3 ± 0.3	1.1 ± 0.2	6.7 ± 2.0		0.81	6.7 ± 0.3
O_2	0.95 ± 0.12	5.1 ± 0.7	1.60 ± 0.35			0.87	10.2 ± 0.4
Ar	0.97 ± 0.12	1.4 ± 0.2	1.00 ± 0.09	19.4 ± 1.9		1.04	

Table 4.1 Measured nonlinear coefficients for the major constituents of air. The Kerr coefficient, n_2, for the instantaneous atomic or molecular response, is shown from Wahlstrand et al. [1] with results from other experiments shown for comparison. Included are the pump pulse durations used in the measurements. Also shown is the molecular polarizability anisotropy $\Delta\alpha$, for which there is much less variability in the literature. The column for Shelton and Rice [2] gives results based on static electric field-induced second harmonic generation measurements at much lower laser intensity than in a filament core.

Table 4.1 summarizes the results from these measurements for the major constituents of air, N_2, O_2, and Ar. Results from other experiments and calculations are shown for comparison, illustrating the wide range of values obtained.

4.3. Sonographic measurements of energy deposition

We have shown previously [49], [52], [74] that the ultrafast laser energy absorption during filamentation generates a pressure impulse leading to single cycle acoustic wave generation ~100 ns after the laser passes, followed at ~1 μs by a residual 'density hole' left in the gas after the acoustic wave propagates away. Hydrodynamics simulations show that for moderate perturbations to the gas, for which single filaments qualify, either the acoustic wave amplitude or the hole depth is proportional to the local laser energy absorbed [49], [52], [74]. While measurement of

the density hole depth requires an interferometry setup with associated phase extraction analysis, the simplest approach is to measure the *z*-dependent acoustic amplitude with a microphone, and we use this signal as a proxy for laser energy absorbed by the gas.

Laser energy is nonlinearly absorbed by the gas through ionization and molecular rotational Raman excitation [74], [75]. (The bandwidth of typical ultrashort 800 nm pulses is too small to support vibrational Raman absorption [70].) The rotational excitation thermalizes as the molecular rotational states collisionally dephase over a few hundred picoseconds [70], while the plasma recombines over ~10 ns. Eventually, but still on a timescale much shorter than the fastest acoustic timescale of a/c_s ~100 ns, where a is the filament radius and c_s is the sound speed, the absorbed laser energy is repartitioned over the thermodynamic degrees of freedom of the neutral gas and forms a pressure impulse that drives the subsequent hydrodynamics.

Acoustic measurements of optical filaments have been used in a number of prior contexts [76]–[79]. Other possible filament diagnostics are plasma conductivity [80], fluorescence [81], and direct [16] and indirect [81]–[85] measurements of filament plasma density, none of which are directly proportional to absorbed laser energy, and all of which require a combination of non-trivial optical setups and data retrieval, and complex auxiliary modeling for interpretation.

4.4. Simulation of propagation and laser energy absorption

For the purposes of comparing the effects of different values of n_2 on filamentation, we employ a 2D+1 simulation of the optical pulse propagation [75], [86], [87]. The simulation models the most relevant aspects of the pulse's propagation, including the instantaneous electronic response, the delayed rotational response, multiphoton ionization, ionization damping, and the plasma response.

The transverse electric field envelope of the laser pulse evolves according to the modified paraxial wave equation

$$\left[\nabla_{\perp}^{2}+2\frac{\partial}{\partial z}\left(ik-\frac{\partial}{\partial\xi}\right)-\beta_{2}\frac{\partial^{2}}{\partial\xi^{2}}\right]E=4\pi\left(ik-\frac{\partial}{\partial\xi}\right)^{2}P_{NL} \qquad (4.2)$$

where $k=\omega_0 c^{-1}[1+\delta\varepsilon(\omega_0)/2]$, ω_0 is the pulse carrier frequency, $\delta\varepsilon(\omega)$ is the neutral gas contribution to the linear dielectric response, $\xi=v_g t-z$ is the position coordinate in the group velocity frame, $v_g=c\left[1-\delta\varepsilon(\omega_0)/2\right]$, and $\beta_2/\omega_0 c=(\partial^2 \mathrm{k}/\partial\omega^2)\big|_{\omega=\omega_0}=20\mathrm{fs}^2/\mathrm{m}$ [88] accounts for group velocity dispersion in air. Included in the nonlinear polarization density, $P_{NL}=P_{elec}+P_{rot}+P_{free}+P_{ioniz}$, is the instantaneous electronic (Kerr) response, the delayed molecular rotational response, the (linear) free electron response, and a polarization density term associated with the laser energy loss from ionization (ionization damping).

It is convenient to express the electronic and rotational polarization densities as the product of an effective susceptibility and the electric field: $P_{elec} = \chi_{elec} E$ and $P_{rot} = \chi_{rot} E$, where

$$\chi_{elec} = \frac{1}{16\pi}\left(\frac{N_g}{N_{atm}}\right) n_2 |E|^2 \qquad (4.3a)$$

$$\chi_{rot} = \sum_j \frac{N_g (\Delta\alpha)^2}{15\hbar} \frac{(j+1)(j+2)}{2j+3}\left(\frac{\rho^0_{j+2,j+2}}{2j+5} - \frac{\rho^0_{j,j}}{2j+1}\right) \int_{-\infty}^{\xi} \sin[\omega_{j+2,j}(\xi' - \xi)] |E|^2 d\xi' \qquad (4.3b)$$

Here, n_2 is the nonlinear index of refraction (Kerr coefficient) at 1 atm, N_{atm} is the gas density at 1 atm, N_g is the gas density, $\Delta\alpha$ is the difference in molecular polarizabilities parallel and perpendicular to the molecular bond axis, j is the total angular momentum quantum number, $\omega_{j+2,j} = \hbar(2j+1)/I_M$, I_M is the moment of inertia, and the $\rho^0_{j,j}$ are thermal equilibrium density matrix elements [70], [86].

The free electron polarization density is determined by $(ik - \partial_\xi)^2 P_{free} = (4\pi)^{-1} k_p^2 E$ where $k_p^2 = 4\pi e^2 N_e / m_e c^2$ is the square of the plasma wavenumber and N_e is the free electron density. For inverse-bremsstrahlung losses, we include an electron-neutral collision rate, ν_{en}, on the left side of Eq. (4.2) when solving for the plasma response only. The ionization damping polarization density evolves as $(ik - \partial_\xi) P_{ioniz} = -2\kappa_{ion} E$, where

$$\kappa_{ion} = c^{-1} U_I \nu_I N_g \frac{1}{|E|^2} \qquad (4.4)$$

is the damping rate, U_I is the ionization potential, ν_I the cycle-averaged ionization rate [89], and $\partial_{\xi} N_e = c^{-1}\nu_I N_g$. A sum over species, namely nitrogen and oxygen, is implied in Eqs. (4.3) and (4.4). We neglect the contribution of Ar, which at ~1% atmospheric concentration has a negligible effect on the propagation simulation results.

With these expressions for the polarization densities and Eq. (4.2), the local depletion per unit length of the laser pulse energy, U_L, is given by

$$\frac{\partial}{\partial z} U_L = -\frac{1}{c}\int\left[2\pi\left(\frac{\partial \chi_{rot}}{\partial \xi}\right) I_L + \nu_I U_I N_g + c^{-1}\nu_{en}\left(\frac{\omega_p}{\omega_0}\right)^2 I_L + m_e c^2 K_{osc}\nu_I N_g\right] d^2 r d\xi \qquad (4.5)$$

where $I_L = (8\pi)^{-1} c\,|E|^2$ is the intensity and $K_{osc} = (e\,|E|/2m_e c\omega_0)^2$ is the normalized, cycle averaged quiver energy of a free electron. In order, the terms in the integrand represent the energy from the laser pulse absorbed (restored) by rotational excitation (de-excitation), the energy absorbed in freeing electrons from their binding potential (ionization energy), inverse-bremsstrahlung losses, and the cycle-averaged kinetic energy imparted to electrons by the laser field as they enter the continuum, a result of freed electrons being born with zero velocity. This final term is often referred to as semi-classical above threshold ionization energy [90].

Our experiments use beam aperturing and weak focusing of the laser pulse to enable adjustment of the *f*-number and to promote filamentation. To model the aperture, a radial filter is applied to the electric field. In particular, the field just after the aperture, $E_{a,+}$, is given by $E_{a,+} = \left[1 - 4(r/r_a)^{18} + 3(r/r_a)^{24}\right] E_{a,-}$, where r_a is the aperture radius and $E_{a,-}$ is the field just before the aperture. We note that the filter

function's value and derivative vanish at $r = r_a$. The lens is modeled by applying the thin-lens phase factor to the electric field $E_{l,+} = \exp(-ikr^2 / 2f) E_{l,-}$, where $E_{l,+}$ and $E_{l,-}$ are the fields just after and just before the lens and *f* is the lens focal length. The laser input field is modeled as $E(\xi) = \sin(\pi\xi / \sigma)$ for $0 < \xi < \sigma$, where the FWHM of $|E(\xi)|^2$ is $\sigma / 2$.

The simulations performed for this chapter examine the sensitivity of the axial profile of filament energy deposition to the choice of values of n_2 for N_2 and O_2. These determine the magnitude of the instantaneous part of the response and enter the simulation via Eq. (4.3a). The rotational response model, which is described by Eq. (4.3b) and uses the values of $\Delta\alpha$ from Table 4.1, remains unchanged for all simulations.

4.5. Experimental setup

The experimental setup is shown in Fig. 4.1. Pulses from our 10 Hz Ti:Sapphire laser system were apertured through a variable diameter iris immediately followed by a *f* = 3m MgF_2 lens to gently initiate filamentary propagation. The pulsewidth, pulse energy, and iris diameter were varied while still producing stable single filaments. Single filament propagation was confirmed by visually inspecting the beam on an index card over the full range of propagation into the far field. A compact electret-type microphone was mounted on a rail, 3 mm away from the filament, to enable scans over the full filament length. The microphone's transverse position variation

with respect to the filament was < 0.5 mm over the full scan. Since the sound wave amplitude decreases with distance from the filament as $\sim r^{-1/2}$, the fractional change in acoustic amplitude A for a radial variation Δr is $|\Delta A / A| = \frac{1}{2}|\Delta r / r|$. For our case, $|\Delta A / A| < 8\%$. The output signal of the microphone was digitized and collected by a computer for analysis. At each scan position along the filament, ~50 microphone traces were averaged. A typical averaged trace is shown in the inset of Figure 4.1. A CCD camera served as a shot-by-shot energy monitor using a small portion of the beam transmitted through a turning mirror. Energy binning allowed the discarding of laser shots deviating from the quoted pulse energy by more than ~10%. Note that the sound wave's maximum frequency is roughly $c_s / a \sim$ 10 MHz, greatly in excess of the microphone bandwidth's upper limit of ~15 kHz, so that the measured trace is simply the impulse response, whose peak is proportional to the acoustic wave amplitude.

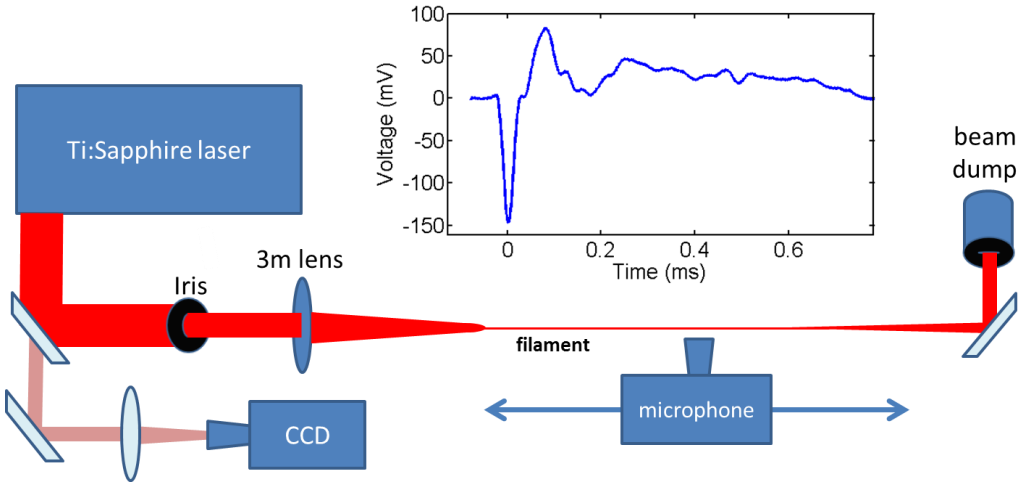

Figure 4.1 Pulses from a 10Hz Ti:Sapphire laser are apertured by an iris and focused by a f = 3 m MgF_2 lens, forming an extended filament. A small portion of the laser energy is collected by a CCD camera to enable later energy binning of the results. An electret-type microphone positioned 3 mm away from the propagation axis is axially scanned along the full length of the filament in 1 cm steps. Also shown is a typical averaged microphone signal.

4.6. Results and discussion

Figures 4.2 and 4.3 show microphone scans and propagation simulations for filaments generated with f/505 focusing (pulse energy 2.5 mJ) and f/300 focusing (pulse energy 1.8 mJ), for pulsewidths τ = 40 fs and τ = 132 fs. The pulse energy was reduced in the *f*/300 case to maintain single filamentation. As discussed above, the plotted points are proportional to the peak acoustic wave amplitude, which is proportional to the local energy absorption (or energy deposited per unit length) by the laser pulse. The simulation points are calculated as $-\partial U_L / \partial z$ from Eq. (4.5).

In the experiments, the laser pulsewidth was varied to explore the relative importance of choice of n_2 when filamentation is dominated by the instantaneous (Kerr) versus delayed (rotational) nonlinearities, and the *f*-number was varied to test the effect of lens focusing on the sensitivity of this choice.

Our prior work [1], [16], [17] has established that 40 fs pulses dominantly experience the instantaneous Kerr nonlinearity characterized by n_2, while the nonlinearity experienced by 132 fs pulses is dominated by molecular rotation. This is because the fastest onset timescale for the rotational contribution, $\Delta t_{rot} \sim 2T / j_{\max}\left(j_{\max}+1\right) > \sim 50$ fs, is set by the highest significantly populated rotational state $j_{\max}$ (~16-18) impulsively excited in the filament at the laser pulse clamping intensity. Here T = 8.3 ps is the fundamental rotational period for N_2 [70]. This leads us to expect that the choice of n_2 will be more significant for propagation simulations of shorter pulses.

We also expect that sensitivity to the choice of n_2 will be more pronounced in simulations of longer *f*-number-generated filaments. This is because larger *f*-numbers imply a weaker contribution of lens focusing, and a relatively more important role of nonlinear self-focusing to filament onset and propagation. For unaided filamentation of a collimated beam, the proper choice of n_2 in simulations is expected to be even more important.

Figure 4.2 shows experiment and simulation results for the longer *f*-number-generated filaments, at *f*/505. The left column of panels (green curves) is for 40 fs pulses and the right column of panels (red curves) is for 132 fs pulses. The experimental points are the same in each column, and the simulations explore the effect of using values of n_2 for N_2 and O_2 that are 50% (top row), 100% (middle row), and 150% (bottom row) of the measured values of Wahlstrand *et al*. [1] shown in Table 4.1.

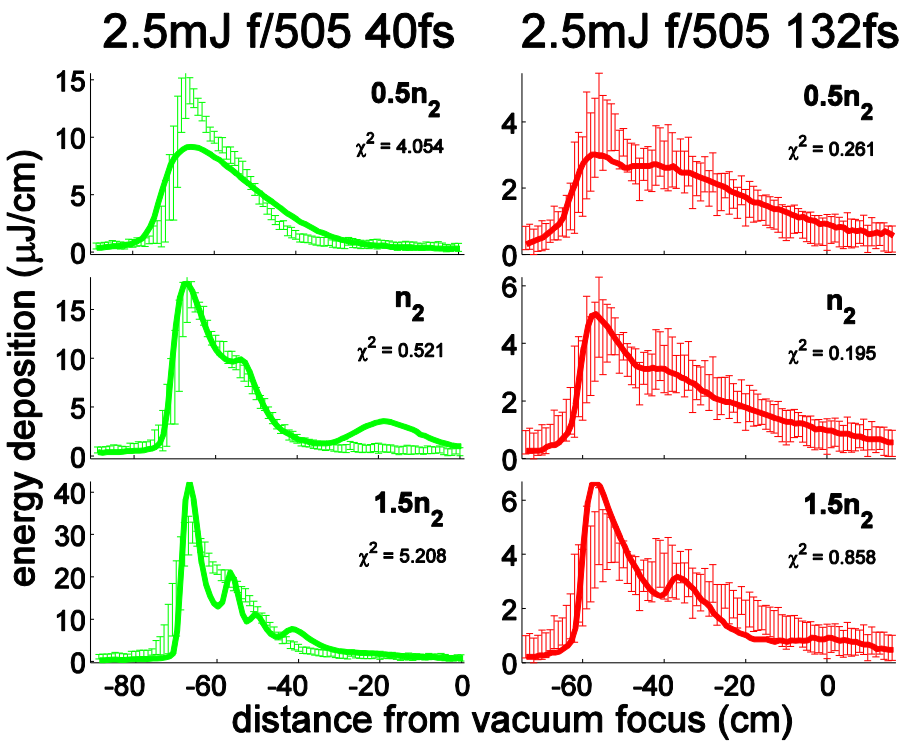

Figure 4.2 Axial scan of average peak signal from microphone trace (points) and propagation simulations of laser energy deposition (solid curves). Filaments were generated with pulse energy 2.5 mJ at *f*/505 for pulsewidths 40 fs (green) and 132 fs (red). The error bars on the points are the standard deviation of the mean for ~50 shots at each axial location. The simulations in the center row use n_2 values for N_2 and O_2 from Wahlstrand *et al.* [1] (see Table 4.1), while simulations in the top and bottom rows use 0.5 times and 1.5 times these values. The vacuum focus position is z = 0. The χ^2 fit result is shown on each plot.

In order to quantitatively assess the agreement between experiment and simulation, a two-dimensional χ^2 fit test was performed according to

$$\left(\chi^2\right)_{jk} = N^{-1}\sum_{i=1}^{N}\left(\left(\lambda_j M(z_i) - \mathrm{S}(z_i + \Delta z_k)\right)/(\lambda_j B(z_i))\right)^2 \qquad (4.6)$$

where a scale factor λ_j was applied to each set of N data points $M(z_i)$, and an axial shift Δz_k was applied to each set of N points $S(z_i)$ simulating energy absorption. Here, $B(z_i)$ is the standard deviation of the mean corresponding to measurement

$M(z_i)$. The scale factor λ_j was adjusted over 10^4 equally spaced values while Δz_k was adjusted in 1 cm increments. The best fit is taken as $\chi^2 = \min\left(\left(\chi^2\right)_{jk}\right)$, the minimum over *j* and *k*, and is shown on each panel of Fig. 4.2. In all cases, the optimum axial shift minimizing χ^2 is less than 9 cm. It was separately verified that changing the effective focal length of the thin lens applied in the simulation by ~10 cm does not change the shape of the simulated energy deposition; rather it changes the longitudinal position at which the energy deposition occurs. It is seen in Fig. 4.2 that minimum χ^2 is achieved for the middle row simulations using the values of n_2 for N_2 and O_2 given in Wahlstrand *et al*. [1]. For that case, the simulation curves match the experimental points surprisingly well.

Further examination of Fig. 4.2 shows that the experiment-simulation mismatch in the shorter pulse (40 fs) case is more sensitive to the choice of n_2 than in the longer pulse case (132 fs). As discussed earlier, the reason for this is that the dominant positive nonlinearity governing propagation in the long pulse case is field-induced molecular rotation, with reduced sensitivity to the instantaneous response characterized by n_2. It is worth noting that in the long pulse case, the signal does not go to zero at either end of the plot because measurable filament energy deposition extended beyond the range of the microphone rail travel.

Note that in our simulations, we use the ionization model of Popruzhenko *et al*. [89] without any adjustments. That ionization rate is valid for arbitrary values of the Keldysh parameter and has been verified by comparisons to numerical solutions of the single active electron, time-dependent Schrodinger equation. A fair question is

whether use of a different ionization rate, say the one of [89] scaled by a constant factor, would have resulted in a different value of n_2 providing the best fits in Fig. 4.2.

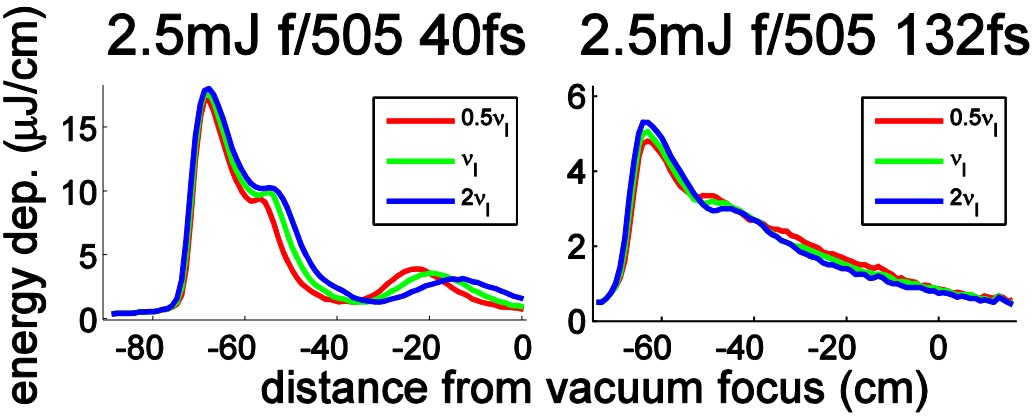

Figure 4.3 Propagation simulations of laser energy deposition for the conditions of Fig. 4.2, for three scalings of the ionization rate ν_I of Popruzhenko *et al*. [89]. All simulations use n_2 values for N_2 and O_2 from Wahlstrand *et al*. [1]. This figure illustrates the relative insensitivity of energy deposition to variations in ionization rate compared to variations in n_2.

To test this possibility, we performed simulations as in Fig. 4.2 but with scale factors of 0.5 and 2 multiplying the ionization rate ν_I of [89]. The result is shown in Fig. 4.3, where it is seen that the absorbed energy profiles remain very similar in amplitude and shape, and are certainly much less sensitive to changes in ν_I than to variations in n_2, as seen in Fig. 4.2. This is a consequence of intensity clamping combined with the high order intensity dependence of the ionization rate. Intensity clamping occurs roughly when $n_2 I \sim \Delta N_e / 2N_{cr}$, when Kerr focusing is offset by plasma-induced defocusing. If we consider multiphoton ionization (MPI) with $\Delta N_e \sim R N_0 \Delta t$, where $R = \alpha_m I^m$ is the MPI rate (m = 9 for oxygen and λ = 800 nm), N_0 is the gas density, Δt is the ionization time, and α_m is the MPI scale factor, the

clamping intensity is approximately $I_{cl} \sim \left[\frac{2n_2 N_{cr}}{\alpha \Delta t N_0} \right]^{1/(m-1)}$. Scale factors varying from $\alpha = 0.5\alpha_m$ to $\alpha = 2\alpha_m$ yield a ~±10% variation in the clamping intensity. In fact, an increase in ionization rate through α leads to a decrease in ionization time Δt, further reducing the sensitivity of I_{cl} to ionization rate.

Results from experiments and simulations for filaments generated at a lower *f*-number, *f*/300, are shown in Fig. 4.4. The figure panels are organized in the same way as in Fig. 4.2. Here again, it is seen that the best fit between simulation and experiment, as measured by χ^2, is for simulations using the n_2 values measured in Wahlstrand *et al*. [1]. These simulations match the experiment quite well. There are two additional important observations. First, as before, and for the same reason, the long pulse (132 fs) simulations are less sensitive to choice of n_2 than short pulse simulations. Second, even with the greater sensitivity of the short pulse simulations to choice of n_2, that sensitivity is reduced from the *f*/505 case of Fig. 4.2. This is because at *f*/300 (which induces ~70% more phase front curvature), the lens plays a relatively more important role in the filament propagation.

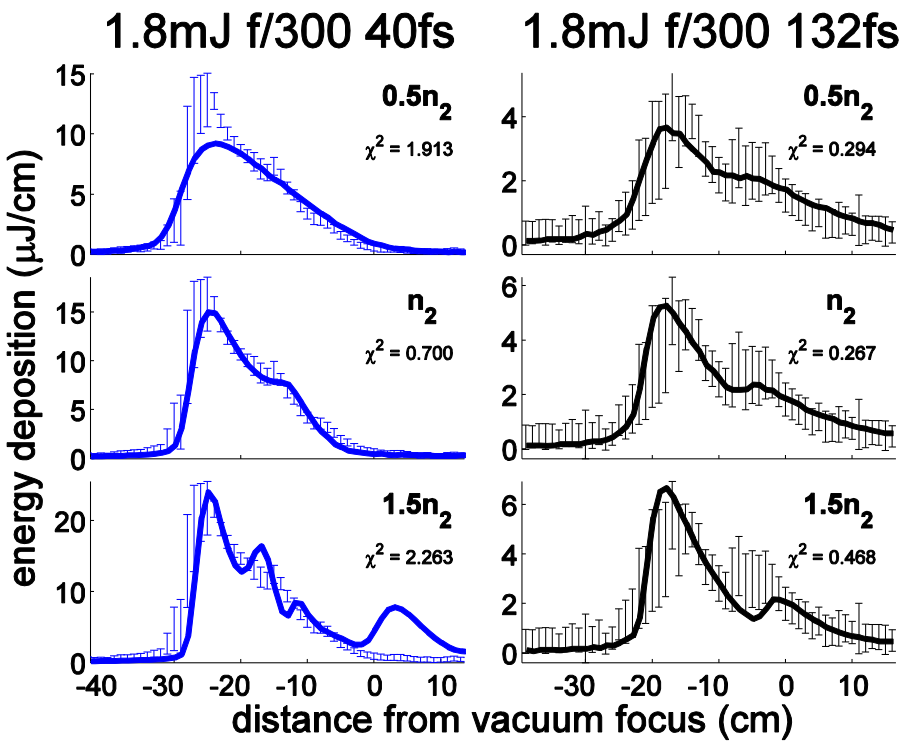

Figure 4.4 Axial scan of average peak signal from microphone trace (points) and propagation simulations of laser energy deposition (solid curves). Filaments were generated with pulse energy 1.8 mJ at *f*/300 for pulsewidths 40 fs (blue) and 132 fs (black). The error bars on the points are the standard deviation of the mean for ~50 shots at each axial location. The simulations in the center row use n_2 values for N_2 and O_2 from Wahlstrand *et al.* [1] (see Table 4.1), while simulations in the top and bottom rows use 0.5 times and 1.5 times these values. The vacuum focus position is $z = 0$. The χ^2 fit result is shown on each plot.

There are several locations in the short pulse simulations (middle green panel of Fig. 4.2 and bottom blue panel of Fig. 4.4) showing a downstream resurgence in the laser absorption. This is an artifact produced by the radial symmetry assumed by the simulation, which arises due to a combination of space-time focusing and plasma refraction at the back of the pulse. Azimuthal intensity variation in real experimental beam profiles (and the associated azimuthally varying nonlinear phase pickup) significantly reduces the on-axis superposition of beam contributions, thereby reducing or eliminating the energy deposition compared to the simulation. In effect, a beam with azimuthal asymmetry consists of several modes, each with a different

critical power. As a result these modes focus at different axial positions resulting in a more diffuse deposition of the pulse energy along the axis.

Our simulations also allow an examination of the individual laser absorption channels in air. Figure 4.5 shows plots of three of the absorption terms in Eq. (4.5). The contribution of inverse bremsstrahlung absorption (third term) is negligible because $\nu_{en} t \ll 1$, and is not shown. Two contributions dominate for most of our measured filament parameters. One is rotational excitation of molecules, described by the first term in Eq. (4.5). The other dominant channel is the energy absorbed in ionization, here taken as the promotion of bound electrons to the continuum with zero velocity (second term in Eq. (4.5)). The contribution of the fourth term, the excess energy from above threshold ionization (modeled as a semi-classical electron drift energy), which goes into electron heating, is comparatively less significant. For lower intensity and longer duration pulses, the molecular rotation channel can dominate ionization, as seen for a large portion of the filament length in the *f*/505, $\tau = 132$ fs case. This follows straightforwardly from the reduced ionization rate at lower intensity and the more efficient coupling to molecular rotation of longer pulses [1], [16], [70]. Conversely, for higher intensity pulses, ionization dominates. It is interesting to note that in both cases of Fig. 4.5, there is significant molecular absorption both in advance of the onset of ionization and well beyond where ionization fades away.

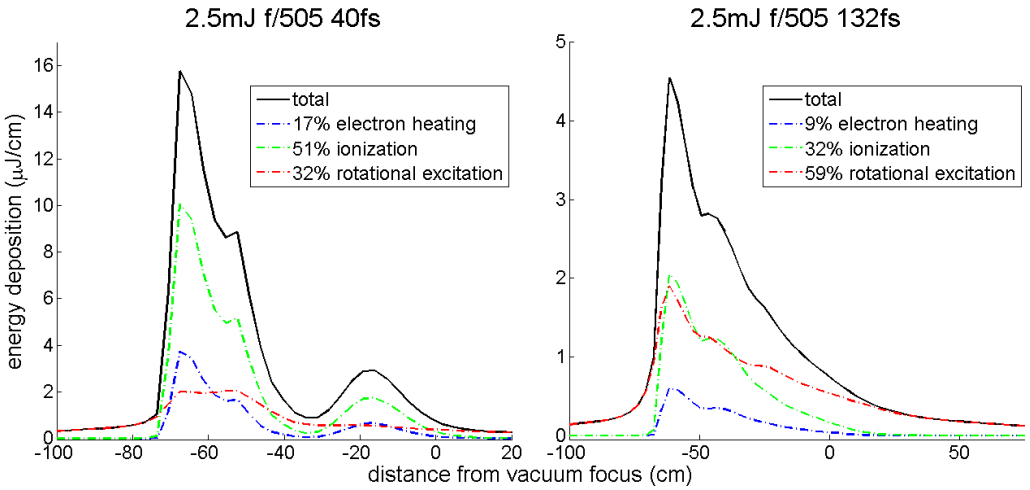

Figure 4.5 Simulated energy deposition due to various mechanisms in air for the laser parameters shown above each panel. The solid curve (black) represents the total energy deposited into the air, while dotted curves represent the energy deposited through above threshold ionization (blue), ionization of the medium (green), and rotational excitation (red). Inverse bremsstrahlung heating of the electrons is negligible and not shown.

4.7. Conclusions

We have shown that the *z*-dependent monitoring of the acoustic wave launched by a filament is a remarkably sensitive diagnostic of the laser energy absorption physics of filamentation. This diagnostic has enabled detailed comparisons of filament propagation experiments with simulations. It was seen that simulations of filament propagation in air depend sensitively on the choice of the nonlinear indices of refraction, n_2, which describe the instantaneous portion of the nonlinear response. The values of n_2 for N_2 and O_2 providing the best fit between simulation and experiment are those measured in Wahlstrand *et al*. [1], with excellent agreement in that case. For longer laser pulses and lower *f*-number induced filamentation, sensitivity to the proper choice of n_2 is reduced due to the relatively larger roles of

the molecular rotational nonlinearity and the lens focusing. Based on our results, we expect that the most sensitive test for the proper choices of n_2 is beam collapse and filamentation by a collimated beam without assistance from a lens.

Chapter 5: Energy deposition of single filaments in the atmosphere

5.1. Introduction and motivation

In the preceding chapters, several schemes have been proposed not only for long-range femtosecond filament related applications but also fundamental measurements of physical constants related to ultrashort pulse propagation. Crucial to these schemes is the nonlinear deposition of energy into the propagation medium. In the case of the air waveguide presented in Chapters 2 and 3, the magnitude and distribution of energy deposition determines the depth and axial extent of the index perturbation constituting the air waveguide. Because such waveguides are generated using multi-filamenting beams generated by the collapse of higher order transverse modes [30], [52], a basic goal is to determine the energy deposition per unit length of propagation for a single filament.

As described in the previous chapters, a filamenting pulse propagating through the atmosphere deposits energy into the propagation medium primarily through optical field ionization and by non-resonant rotational Raman excitation of the air molecules [74]. In Chapter 4, simulations were presented which account for these and other energy deposition channels which are present but are comparatively negligible: heating by above threshold ionization, whereby a photo-ionized electron is born with nonzero kinetic energy [90], and inverse bremsstrahlung heating by laser-driven electron-ion collisions in the dilute filament plasma [91]. All of the direct excitations of the air by the filament are eventually converted to a localized distribution of thermal energy of neutral air [49]: the weakly ionized plasma channel produced by

the filamenting pulse recombines in less than ~10 ns [82], and the rotational excitation collisionally decoheres on a ~100 ps timescale [70].

Several researchers have published findings attempting to theoretically estimate or experimentally measure the magnitude of energy deposition into the air during femtosecond filamentation. Sprangle, et. al., [92] provide estimates of both pulse energy depletion per unit length, as well as maximal distance over which a pulse can propagate by assuming that all liberated pulse energy goes into ionizing the air. Mechanisms which contribute to the termination of filamentary propagation such as divergence gained by the pulse during propagation [93], and temporal pulse-splitting [94] have also been examined. Additionally, energy deposition in the 'superfilamentation' regime has recently been experimentally measured [95]. Our results presented in this chapter are distinct from these recent measurements [95]–[98] of laser propagation and absorption under tight (non-filamentary) focusing of an ultrashort pulse in air, where because the focusing is lens-dominated rather than nonlinearity-dominated, the pulse intensity can exceed the typical clamping intensity in air of ~5×10^{13} W/cm^2 [99], with an attendant significant increase in gas ionization and laser absorption. The results presented in this chapter suggest that in either the loose-focusing or collimated regime of filamentary propagation, the energy loss does not play a significant role in limiting filament length, because at filament termination, the pulses still contain energy well above the critical power for self-focusing, $P > P_{cr}$.

5.2. Partitioning of the absorbed laser energy

It is first useful to assess the fraction of absorbed laser energy that goes into the acoustic wave. Once the single-cycle acoustic wave propagates away from the laser-heated volume, the gas is in pressure balance (that is, the pressure is uniform), leaving an elevated temperature and reduced density at the density hole, with the temperature and density transitioning to ambient atmospheric temperature and density outside the hole [49], [52]. For an ideal diatomic gas for which only translational and rotational degrees of freedom are available, the thermal energy density is related to the pressure by $\varepsilon = \frac{5}{2}P$. (The filament-induced gas temperature rise is insufficient to excite vibrations). Thus, after the acoustic wave propagates away, the energy density throughout the region is constant and equal to its pre-laser heating value. We therefore infer that the acoustic wave carries away nearly 100% of the energy invested in the gas by the laser pulse. Other possible energy dissipation channels are thermal radiation and thermal conduction. For the initial filament-induced temperature increase of $\Delta T \sim 100K$ [49], thermal radiation is negligible, and on the ~1 μs timescale over which the acoustic wave propagates away, thermal conduction has had little time to affect the energy balance [49].

The above analysis shows that two independent methods can be used as proportional measures of laser energy absorption: microphone measurements of the acoustic wave, and interferometric measurement of the density hole remaining after the acoustic wave propagates away. If the initial absorbed energy density from the

filament is $\Delta\varepsilon_i = \frac{5}{2}\Delta P_i$, where $\Delta P_i = N_0 k_B \Delta T_i$ is the initial pressure increase upon laser heating, N_0 is the ambient air density, ΔT_i is the initial temperature increase and k_B is Boltzmann's constant, a microphone placed a fixed short distance R from the filament will register a peak signal amplitude $\delta S_{mic} \propto \Delta P_i / R^{1/2} \propto \Delta\varepsilon_i$, a proportional measure of laser energy absorption. Meanwhile, the residual density hole left behind by the acoustic wave has a maximum initial depth $\Delta N_i = -\Delta T_i \left(N_0 / T_0 \right)$, which later evolves as $\Delta N(t) = -\Delta T(t)\left(N_0 / T_0 \right)$ as the temperature relaxes to the ambient value T_0 by thermal diffusion [49]. Therefore, an interferometric measurement of the depth of the density hole at a fixed delay, after the acoustic wave has left, is also a proportional measure of the initial laser energy absorption.

5.3. Experimental setup

The experimental setup is shown in Fig. 5.1, incorporating interferometric and microphone measurements of filament absorption (Fig. 5.1(a)), as well as a third independent technique, a direct measurement of absorption using a broadband photodiode and integrating sphere (Fig. 5.1(b)). Up to ~ 2 m long filaments were generated by weakly focusing λ = 800 nm Ti:Sapphire laser pulses at f/600 with an $f = 3$ m MgF_2 lens. Incident pulse energy was varied by passing the beam through a motorized waveplate followed by two reflections from thin film polarizers, allowing excellent polarization contrast and fine pulse energy variation between 0 and 4 mJ. Pulsewidth was varied by changing the compressor grating separation. Examination

of the beam with a card along the filament ensured that for all pulse energies chosen, propagation was in the single filament regime.

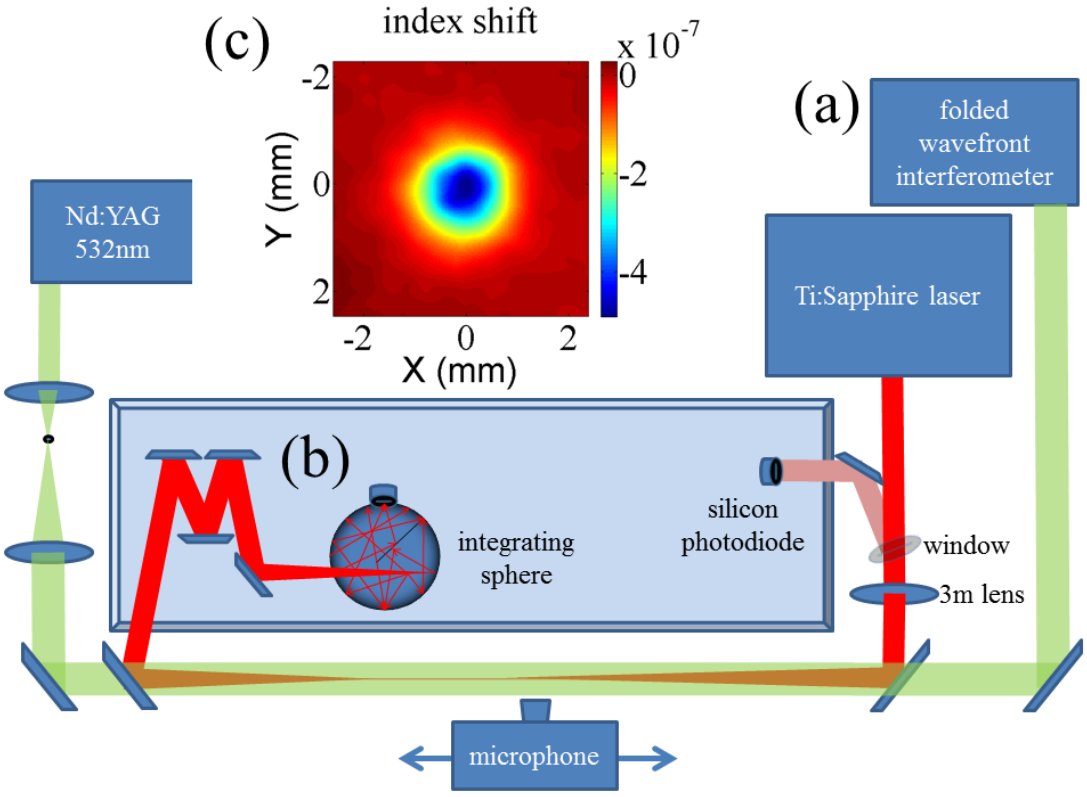

Figure 5.1 (a) Pulses from a 10 Hz, 800 nm, Ti:Sapphire amplifier are focused at *f*/600 by an *f* = 3 m MgF_2 lens to form a single filament of length < 2 m. Part of the incident pulse energy is measured by a reference Si photodiode. After filament termination, the far field beam mode is near-normally reflected by a sequence of wedges and collected by an integrating sphere, enabling a direct, broadband, and sensitive measurement of absorbed energy. (b) A 7 ns, 532 nm interferometer probe pulse (variably delayed between 2-5ms) is propagated longitudinally along the filament-induced density hole and into a folded wavefront interferometer for retrieval of $\overline{\Delta n}(\mathbf{r}_\perp)$, the axially averaged refractive index shift profile. The inset shows a typical $\overline{\Delta n}(\mathbf{r}_\perp)$ profile obtained from a 100-shot averaged phase shift profile.

For the direct absorption measurements (Fig. 5.1(b)), reflection from a thin glass window prior to the start of filamentation gives a reference photodiode signal proportional to the incident pulse energy. In the far-field, after self-termination of the

filament, the beam is attenuated by near-normal incidence reflections (< 3° from normal) from a series of glass wedges and sent into an integrating sphere with an identical photodiode. The UV-enhanced silicon photodiodes have a relatively flat spectral response in the visible/NIR spectral region as do the near-normal incidence wedge reflections and the integrating sphere internal coating. This setup accommodates the extreme spectral broadening induced by filamentation.

The reference and integrating sphere photodiode signals were absolutely calibrated against a commercial laser energy meter and relatively calibrated against each another using a long pulse (~10 ns), low energy, linearly propagating (non-filamenting) beam, derived from the Ti:Sapphire laser with the oscillator seed pulse blocked. The photodiode signals were found to be linearly proportional to each other and to the incident pulse energy to within 1% throughout the entire range of energies used in our experiments.

5.4. Direct absorption measurements

Direct absorption measurements are plotted in Figure 5.2 as a function of incident pulse energy for a range of pulsewidths. The highest absorption of ~4% (~200 μJ) is observed for the shortest and highest energy pulse (50 fs, 4 mJ). The data points are replotted on log-log scales in the inset, where dashed lines following an energy (or intensity I) squared dependence are overlaid. It is seen in all plots that absorption for the low- to mid-range of pulse energies (indicated by left- and right-hand vertical dashed lines) is well-described by an I^2 dependence, with faster variation at higher

energies. Note that the left-hand dashed line extends to lower energies for shorter pulsewidths, consistent with the wider range of intensities available in those cases. The I^2 absorption dependence is consistent with gas absorption by non-resonant two-photon rotational Raman excitation in nitrogen and oxygen, as discussed in [70], [74], [78]. At pulse energies beyond the right-hand dashed line, the absorption is seen to grow faster than I^2, in accord with the onset of plasma generation and additional heating, and then saturate (in the highest peak intensity 50 fs and 70 fs cases) owing to the limitation of laser intensity by plasma defocusing, or intensity clamping [99].

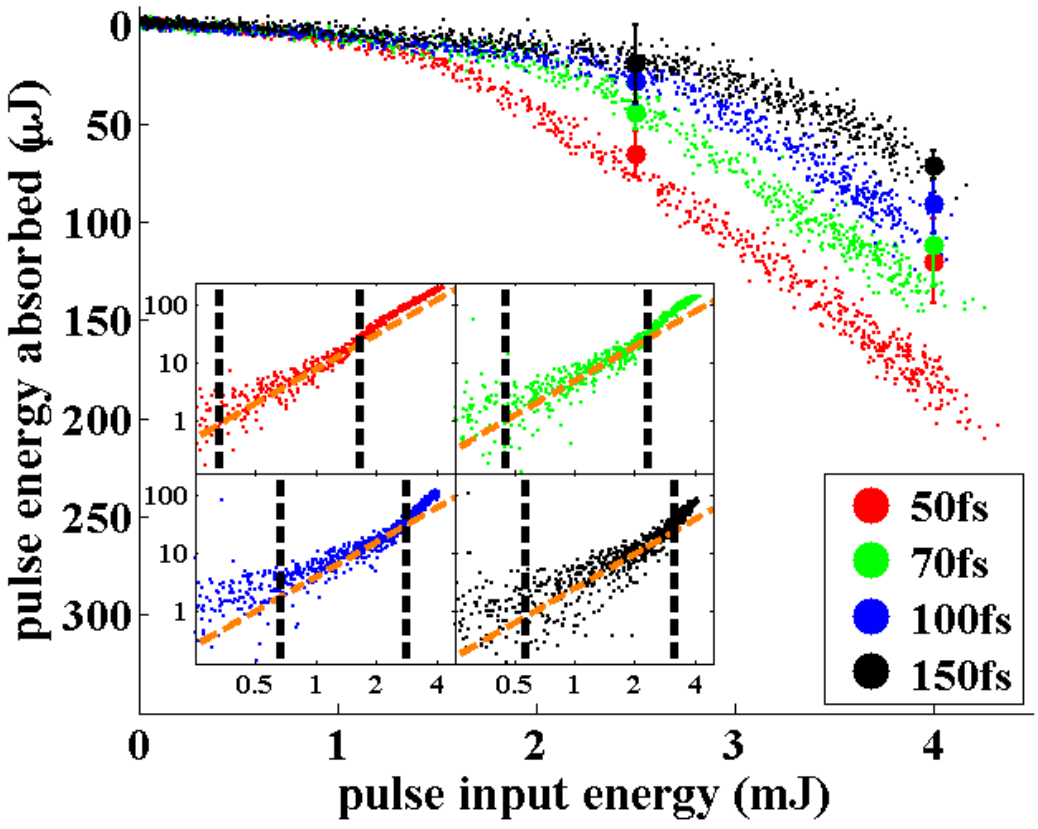

Figure 5.2 Laser pulse energy absorbed in single filamentation versus input pulse energy, as measured using a pair of calibrated photodiodes in the configuration of Fig. 5.1(b). Overlaid points represent measurements of total energy absorption, E_{abs}, determined by longitudinal interferometry. Error bars on those points are the differences between largest and smallest measured absorptions. Inset: Data points of (a) replotted on a log-log scale, overlaid with dashed lines depicting absorption $\propto I^2$.

5.5. Gas hydrodynamic measurements

The initial energy density increase from filament heating can also be written $\Delta\varepsilon_i = \rho_0 c_v \Delta T_i$, where c_v is the specific heat capacity of air at constant volume, ρ_0 is the initial air mass density and where $\int d^2\mathbf{r}_\perp dz\ \Delta\varepsilon_i(\mathbf{r}_\perp, z) = \mathrm{E}_{abs}$, the total absorbed energy. Immediately after the acoustic wave has propagated away and pressure equilibrium is established, the initial mass density distribution of the density hole follows $\Delta\rho_i = -\Delta T_i\left(\rho_0 / T_0\right) = -\Delta\varepsilon_i / c_v T_0$. As the temperature profile relaxes by thermal diffusion, we can *define* an energy density $\Delta\varepsilon(\mathbf{r}_\perp, z, t) = -c_v \Delta\rho(\mathbf{r}_\perp, z, t) T_0$ which has the property $\int d^2\mathbf{r}_\perp dz\ \Delta\varepsilon(\mathbf{r}_\perp, z, t) = -c_v T_0 \int d^2\mathbf{r}_\perp dz\ \Delta\rho(\mathbf{r}_\perp, z, t) = \mathrm{E}_{abs}$ independent of delay. In effect, the magnitude of the energy deposition is encoded in the density profile that remains in the filament's wake after the acoustic wave propagates away. Using $\Delta\rho = \rho_0 \Delta n / (n-1)$, where *n* is the air refractive index [100], the total energy loss along the filament is then $E_{abs} = -c_v T_0 \rho_0 k^{-1} (n-1)^{-1} \int d^2\mathbf{r}_\perp \Delta\Phi(\mathbf{r}_\perp)$ where $T_0 = 297\mathrm{K}$ and $\Delta\Phi(\mathbf{r}_\perp)$ is determined by interferometry.

The gas hydrodynamic response, from which we infer the laser energy absorption, was first measured interferometrically and then sonographically. A variably delayed 7 ns, 532 nm probe pulse counter-propagating with respect to the filament (see Fig. 5.1(a)) provided time-resolved interferometric measurements of the propagation path-averaged gas density depression in the long time delay thermal regime (few milliseconds). In this regime, the mild transverse gas density gradients minimize refraction and distortion of the probe. Beam propagation simulations [101] verify that

the maximum phase error introduced by probe refraction over ~ 2 m filaments is <5% for our experimental parameters. To enable quasi-real time background subtraction for interferometric phase extraction, the pre-filamenting beam is passed through an optical chopper with a 50% duty cycle, alternating shots with and without the filament.

Interferograms were analyzed using standard techniques [102] to extract the 2D spatial phase pattern $\Delta\Phi(\mathbf{r}_\perp) = k\int_0^L dz\ \Delta n(\mathbf{r}_\perp, z)$ imposed on the probe beam by its passage through the filament-induced gas density hole. Here, Δn is the air index change resulting from the gas density hole, z is the filament propagation coordinate, $\mathbf{r}_\perp$ is the transverse coordinate, L is the filament length, and k is the probe beam vacuum wavenumber.

Interferometry-extracted values of total energy absorption are overlaid on the curves of Fig. 5.2 using two input energies and four probe delays at each energy. The error bars are the difference between largest and smallest measured absorptions. These values for absorption are in reasonable agreement with those obtained directly using the photodiode arrangement of Fig. 5.1(b), except that they are consistently smaller, especially for the highest intensity pulses where the direct absorption and interferometry results differ by ~30%. We are currently investigating this discrepancy, which points to a loss mechanism at the highest intensities not contributing to thermal heating.

5.6. Sonographic measurements

While the interferometry experiment provides overall energy absorption, detailed longitudinal dependence of energy absorption was performed using sonographic probing, a technique used in several filament-related experiments [52], [76], [78], [91], [95]. Here, a compact electret-type microphone was scanned alongside the filament at a transverse distance of R = 1.5 mm along its entire longitudinal extent. The microphone signal, $\delta S_{mic} \propto \Delta P_i / R^{1/2} \propto \Delta \varepsilon_i$, was collected at 2 cm steps along the filament.

Figure 5.3 shows longitudinal distributions of energy deposition per unit length dE_{abs} / dz for a range of sonographically probed filaments, where the vertical scale is set by E_{abs} as determined by the longitudinal interferometry experiment, so that Fig. 3 is a purely hydrodynamically-determined result. The values for E_{abs} are in reasonable agreement with the direct absorption measurements of Fig. 5.2. Alternatively, the vertical scales of Fig. 5.3 could have been set by the direct absorption measurements. We note that our results for dE_{abs} / dz are more in line with the long pulse simulation results of ref. [91] at *f*/500 than the short pulse results in that paper. An important question is the dependence of absorption on f-number. We have found through propagation simulations [91] that the peak absorption rate in μJ/cm can drop by a factor of two over the range $f/600 \rightarrow f/\infty$, with average absorption roughly constant.

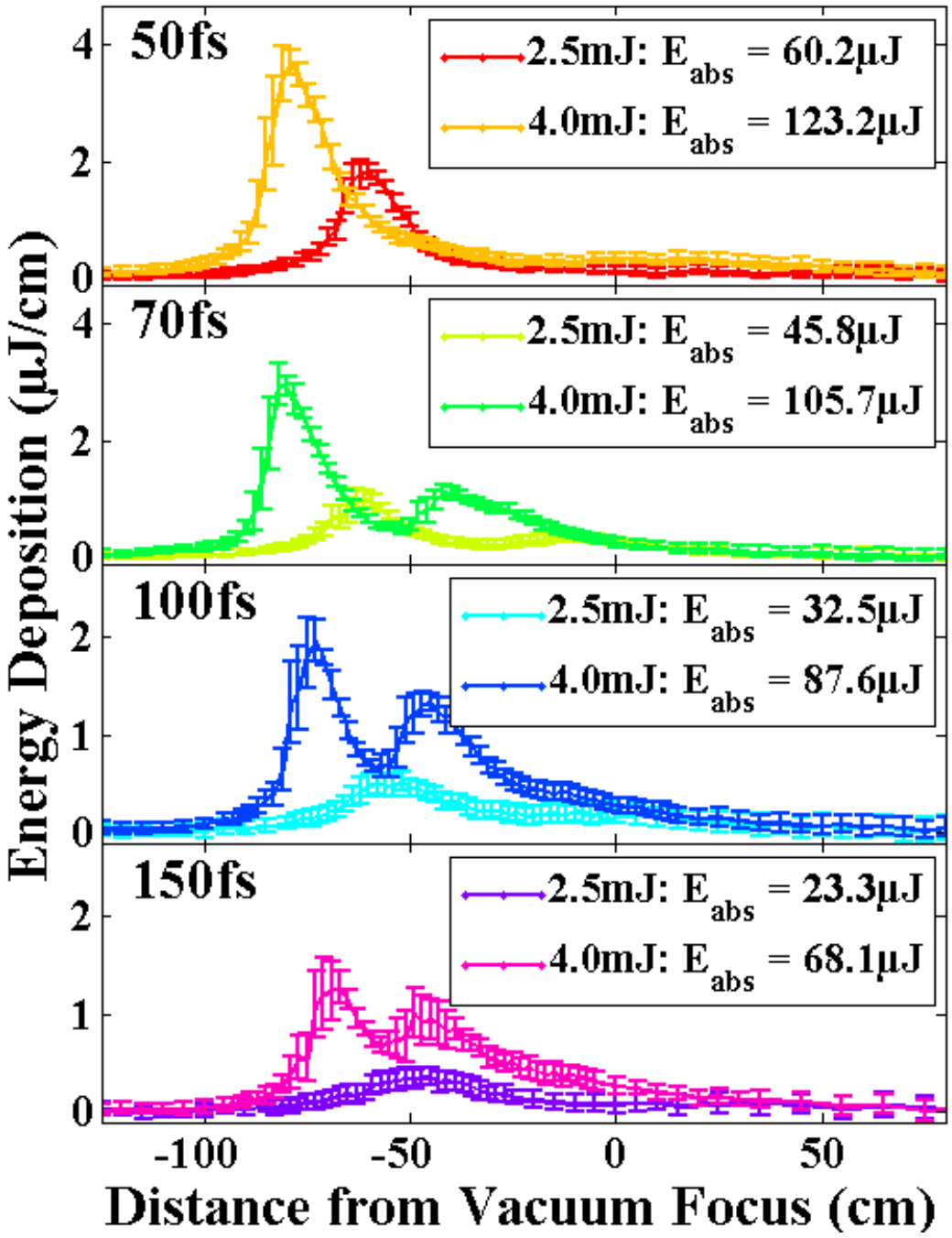

Figure 5.3 Sonographic maps of the linear energy deposition vs position along the filament. The geometric focus of the *f*/600 optics is at $z = 0$. At each position in the axial scan, 100 shots were taken. The error bars are the standard deviation of the peak microphone signal at each position. The values of E_{abs} in the legend are integrals of each curve.

5.7. Limitations on filament length

For application of filament absorption to air waveguide generation, it is useful to consider what limits the length of a single filament. In all cases measured here, filamentary propagation is observed to cease shortly after the vacuum focus with only a small fraction of the total pulse energy absorbed. Our measurements suggest that the energy loss does not play a significant role in limiting filament length, because at filament termination, the pulses still contain energy well above the critical power for self-focusing, $P > P_{cr}$. Prior results [93] have shown that ~ 8 m propagation of a non-lens-assisted filament showed a loss of ~13% and that a lens placed in the beam path downstream of filament termination would initiate another filament. In our case, the dominant effect limiting the length of filaments appears to be divergence of the background reservoir, the region outside the filament core that exchanges energy with it [15], [103]. Diffraction-limited focusing of an *f*/600 beam at λ = 800 nm would normally give a confocal parameter of $2z_0 \sim 60$ cm, which would roughly describe the axial extent of the high intensity region of the filament reservoir. Nonlinear propagation of both the core and the reservoir extends this somewhat, as seen in the sonograms of Fig. 5.3, but the overall length scale of the filament conforms to the confocal parameter.

5.8. Conclusions

The depth of the gas density hole created by a single filament directly controls the index contrast between the core and cladding of the multi-filament-generated air waveguide [30], which in turn directly determines its numerical aperture. As seen from the results, increasing the pulse energy (intensity) in single filamentation increases the energy density absorbed by the propagation medium. Further increasing the energy, for example, in each lobe of a higher order mode will eventually result in multi-filamentation, with the expectation that the energy absorption per filament will conform to our measurements. For example, in a scheme similar to [30], [31], each filamenting lobe from a high order Laguerre Gaussian mode could be made energetic enough to induce multiple filamentation, raising the possibility of dramatically increasing the energy deposition, and thereby increasing the core-cladding index contrast in an air waveguide.

In conclusion, we have presented measurements of the energy deposited by a single filament for a range of laser energies and pulsewidths using two fully independent methods: measurements of absolute absorption, and inference of absorption using interferometric and sonographic measurements of the hydrodynamic response of air to the filament. Knowledge of the spatial distribution of energy deposition from filamentation will inform further study of filament induced air waveguides, which show promise for long-range guiding of high average power lasers and remote collection of optical signals.

Chapter 6: Laser induced electrical discharges

6.1. Introduction

In this chapter, preliminary measurements will be presented for an ongoing experiment to understand the effect of femtosecond filaments on high voltage (HV) discharges in air. In particular, the goal is to elucidate the effects of the filament plasma and the filament-heating induced hydrodynamic density depression on the onset of the discharge.

Considerable work has been done over the past several decades to investigate the ability to trigger HV discharges using intense laser pulses. Spark gaps have found use in several modern applications such as HV surge protection and power switching, measurements of HVs, and as ignition sources in combustion engines. The theory of spark-gap discharges is rich in basic physics and has been discussed at length in the literature [104]–[113]. The basic principle involves electrons in the gap becoming accelerated by the applied electric field and inducing further ionization via avalanche processes. The conventional picture involves this avalanche developing into one or more 'streamers', which under the action of additional joule heating of the air and consequent lowering of neutral gas density, are finally able to create a highly conducting channel bridging the cathode and anode. While spark gaps may be found employing several different triggering mechanisms, advantages of laser triggered spark gap schemes include the inherent electrical isolation that may be achieved between the switch and the load being switched, and the precise timing characteristics afforded by short-pulse laser systems [104]. Furthermore, laser triggering of spark-gaps enables a unique spatial control of the volume through which the discharge

current passes, owing to the well-defined volume of illumination between cathode and anode. In recent years, these efforts have been advanced through the use of ultrafast laser pulses which, unlike nanosecond Q-switched pulses, can produce a continuous plasma string throughout the focal volume [114]. In particular, femtosecond lasers are capable of creating spatially contiguous low-density plasma along their entire propagation path. On the other hand, while nanosecond lasers excel in creating higher plasma densities along their propagation, longitudinally contiguous energy deposition remains a challenge. The use of double pulse schemes [114], [115] or picosecond lasers [116] have recently been proposed as solutions providing both contiguous and substantial plasma density.

6.2. Review of previous spark-breakdown literature

Regardless of the laser pulsewidth used, nearly all of the recent work has used laser pulse intensities well above the ionization threshold of the gas in question, utilizing either the conductivity of the dense plasma to provide an ionized conductive channel through which the discharge can proceed [117], or the resulting energy deposition to heat the gas between electrodes and initiate dielectric breakdown [118], [119]. It has been proposed that this hydrodynamic response is the mechanism responsible for dielectric breakdown in the case of femtosecond laser illumination [118], [119].

Following the early work of Paschen [120] and Townsend [113], it has become widely understood that in the absence of an applied laser pulse, the dielectric

breakdown threshold in gases is (for a constant electrode separation) a function of the gas pressure. Although widely stated in this manner, it may be more correct to consider the breakdown threshold a function of gas density rather than pressure. Paschen's and Townsend's experiments were typically conducted in a constant temperature gas. First identified by Peek, a correction to Paschen's original law is required to account for simultaneous changes in both the gas temperature and pressure [121]. The parameter of interest for gaseous breakdown phenomena is E/N, where E is the electric field strength, and N is the density of neutral particles. An examination of the microscopic phenomena leading to the dielectric breakdown in gases [109]–[113], [120] indicates that the relevant parameters determining the breakdown voltage are the applied electric field strength and the mean free path in the gas, which is in general a function of the gas density, *not* the pressure.

Subsequent work by Loeb [109]–[111] and Meek [112] has laid the groundwork for the explanation of spark discharges in terms of 'streamer' formation. Streamers and associated phenomena of leaders and corona discharge have generated much discussion in the femtosecond laser discharge literature on both long and short spark gaps in air. Recently, Schmidt-Sody, et. al., identified that corona generation and leader formation during filament guided discharges in air are important in the progression of the breakdown [118]. In their paper, ICCD images of the corona generation resulting in leader formation through the gap are used to image the formation and dynamics of the discharge. Additionally, other researchers have found evidence that leader or streamer formation [122], [123] can play a role in the laser induced breakdown process. Gordon, et. al., [124] demonstrated a mode of discharge

which can proceed without the aid of streamers, utilizing a 'flash ionization' caused by Ohmic heating of electrons and subsequent extension of the plasma lifetime due to decreased recombination rates resulting from increased electron temperature. Schmidt-Sody, et. al., demonstrated that a similar effect appears to occur when the discharge is triggered using pulses > 2 ps long [125]. It has been widely understood that the mechanism which controls the dielectric breakdown of a gas in a femtosecond laser triggered spark gap is also affected by the neutral gas density decrease in the wake of the laser pulse [118], [119], [124]. It has been found that this laser produced low density channel can encourage the generation of streamers and leaders at a lower voltage than would be found in the absence of an applied laser pulse [122], [123].

In this chapter, we present *preliminary* measurements of an ongoing experiment to better understand the dynamics of femtosecond laser triggered spark gaps. The aim of these measurements is to better understand and differentiate the roles of laser produced plasma and the consequent hydrodynamic effects in the wake of laser illumination.

To this end, we make spatial and temporal measurements of the gas dynamics occurring in the gap at times after the application of a 100 fs laser pulse or pulse train. In particular, we interferometrically examine the evolution of the filament-ionized and heated air in the electrode gap before breakdown. At voltages just below the breakdown voltage of the gap, we find evidence of gas heating originating from the HV source, leading to deepening and widening of the laser produced channel. These

measurements are combined with time resolved measurements of the delay between application of the laser pulse and the breakdown of the gap.

6.3. Experimental setup

In order to elucidate the mechanisms leading to spark-gap breakdown after passage of a femtosecond laser pulse, we use either single pulses or pulse sequences generated from the output of our 10 Hz Ti:Sapphire amplifier to illuminate a focal volume between two hemispherical tungsten electrodes, as shown in Figure 6.1. Single pulses from our laser amplifier are first passed through a nested interferometer, labelled below as the 'pulse stacker', which is capable of producing eight replica pulses, the relative temporal spacing of which are controlled by motorized translation stages allowing fine tuning (~10 fs) of the temporal inter-pulse delay [126]. For experiments in which a single pulse is utilized, all but one of the pulse-stacker arms are blocked, thus transmitting only a single pulse. The pulse (or pulse sequence) is then passed through an adjustable grating compressor allowing control of the temporal pulsewidth sent to the experiment. Introducing the pulse stacking optics upstream of the compressor affords the advantage of avoiding nonlinear interaction in the beamsplitting optics. Additionally, the pulse (or pulse train) is passed through an optical chopper before the compressor in order to facilitate reliable background collection for our interferometric measurements.

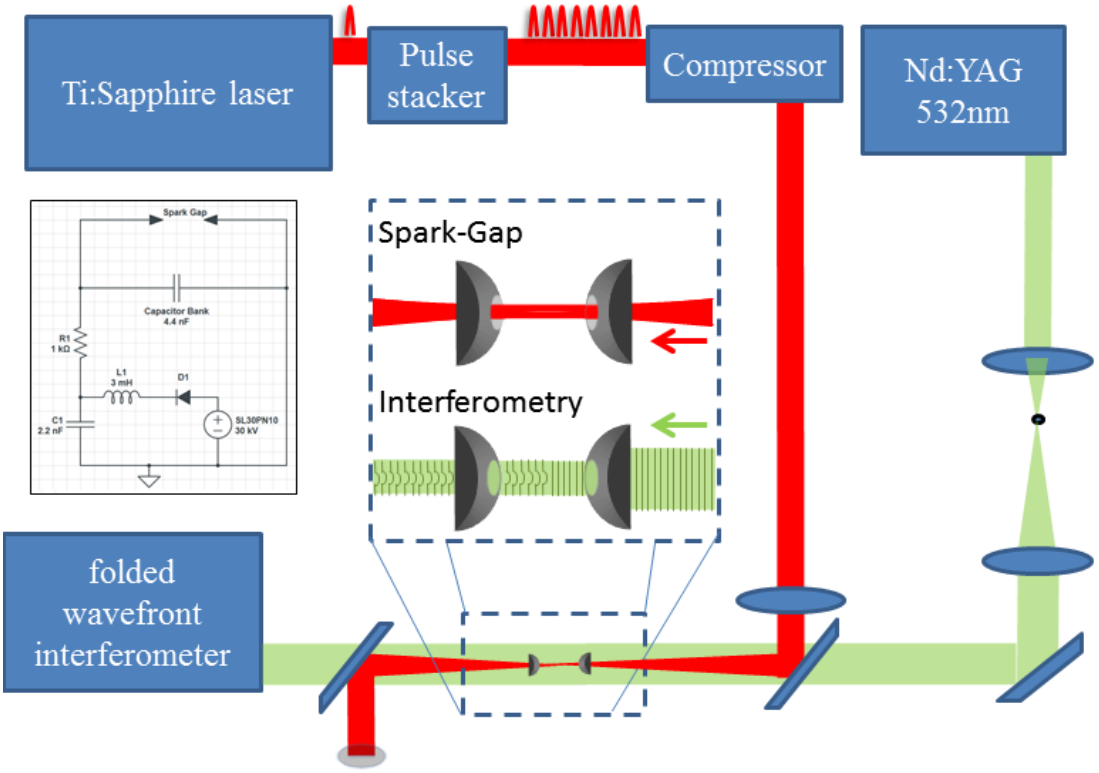

Figure 6.1 Optical setup for investigating the neutral gas density dynamics in the wake of a femtosecond laser pulse excitation in the presence of a HV DC field. The magnified view of the focal region depicts the focal geometry of the femtosecond beam through the spark gap apparatus. Arrows depict the direction of propagation. Also depicted is the usage of a probe beam to diagnose the neutral gas density in the wake of femtosecond laser pulse excitation. Shown as an inset is the circuit used to energize the spark gap apparatus.

The pulse (or pulse sequence) is focused at f/50 using an f = 50 cm lens into the spark-gap apparatus, resulting in a laser illumination between electrodes with confocal dimensions of 4 mm length and w_0 = 23 μm in the transverse dimension. Although the confocal parameter corresponding to the beam focus is 4 mm, the axial extent of the laser produced plasma is likely longer owing to the onset of filamentation. The spark-gap apparatus consists of hemispherical tungsten electrodes with 2 mm diameter holes drilled axially through them. The electrodes are separated by several mm at their closest points, and connected in parallel with a 4.4 nF capacitor bank, which is charged through a 1 kΩ resistor to a maximal potential of

+30 kV by a DC HV power supply (Spellman High-Voltage model SL30PN10). The total stored energy in the capacitor bank is approximately $E = \frac{1}{2}CV^2 = 2\text{J}$. An external diode and an additional capacitor and inductor are placed in series with the HV power supply in order to act as an RF choke to shunt towards ground the strong transient signals resulting from the spark gap breakdown. The entire circuit is shown as an inset of Figure 6.1. In order to investigate the neutral density gas hydrodynamics resulting from the passage of the laser beam in the presence of the HV field, we pass a frequency doubled 532 nm, 10 ns, Nd:YAG probe beam though the holes in the electrodes, then towards a folded wavefront interferometer. The probe beam is passed through a spatial filter prior to the interaction region, allowing for flat phase fronts which enable < 40 mrad noise floor in our single shot interferometric measurements.

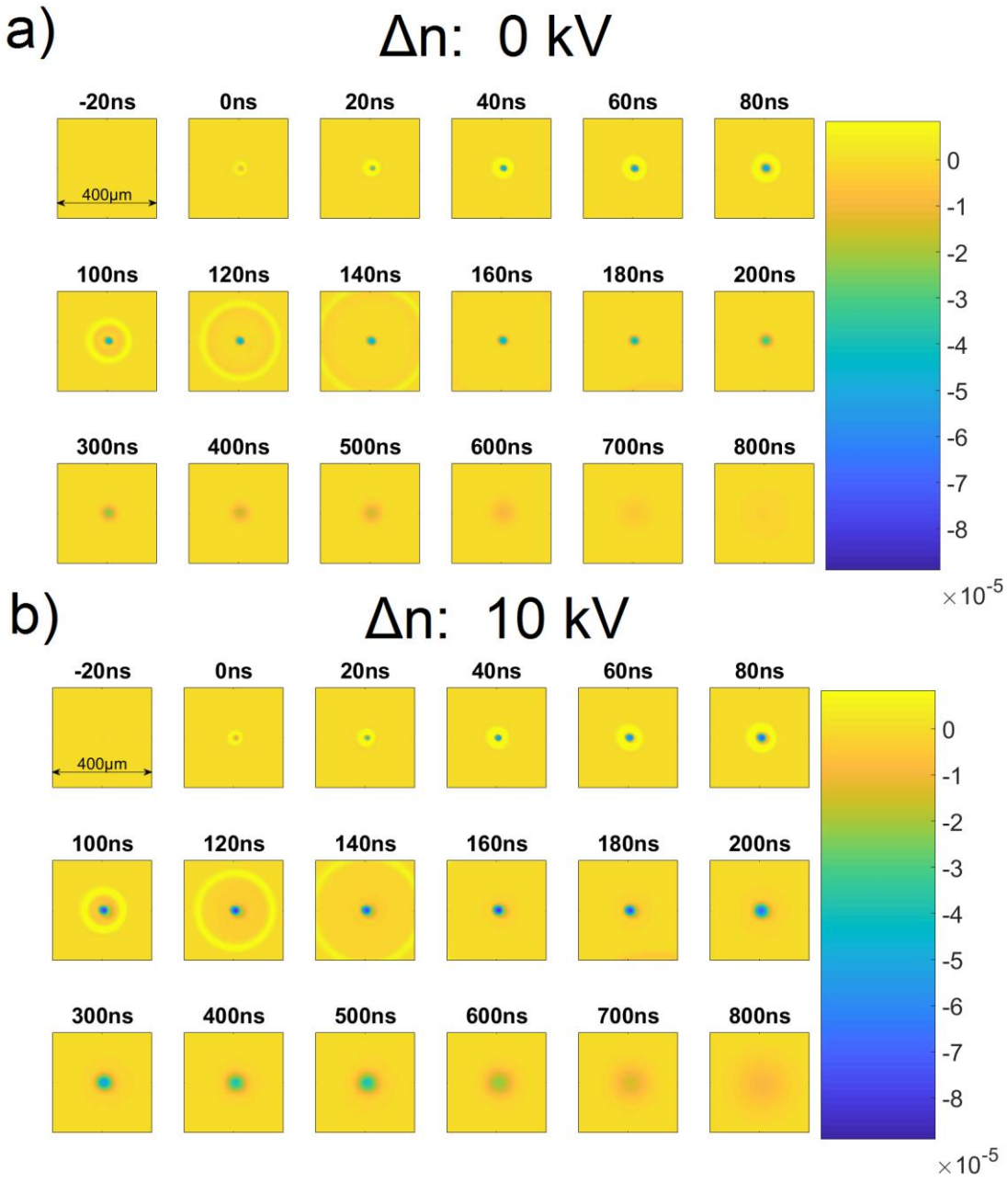

Figure 6.2 (a) Evolution of measured refractive index shift profiles at a sequence of probe delays following the passage of a single 100 fs, 65 μJ laser pulse in the spark gap without an applied HV electric field. (b) Evolution of measured refractive index shift profiles at a sequence of probe delays following the passage of a single 100 fs, 65 μJ laser pulse in the spark gap with applied 10 kV HV electric field.

When a 50-100 fs laser pulse is focused into gaseous media such air, energy is deposited into the medium primarily through optical field ionization and non-resonant

rotational Raman excitation of the air molecules (the laser bandwidth is not wide enough for vibrational Raman excitation). The laser produced plasma recombines to the neutral gas on a ~10 ns timescale [16], while molecular rotational excitation collisionally decoheres on a ~100 ps timescale [70]. Owing to the finite thermal conductivity of the gas, the initial energy invested in the gas is still contained in a ~50 μm radial zone (as depicted in Figure 6.2 above), but is repartitioned into the translational and rotational degrees of freedom of the neutral gas [49]. The result is an extended region of high pressure at temperatures up to a few hundred K above ambient [30]. In air, this pressure source launches a radial sound wave ~100 ns after the filament is formed [52]. By ~1 μs, the gas reaches pressure equilibrium with an elevated temperature and reduced gas density in the volume originally occupied by the beam. Over much longer timescales ~100 μs - ~1 ms, this density depression decays by thermal diffusion. The dynamics described here have been presented in previous chapters of this thesis and published works, and a time-sequence of index perturbation profiles following application of a 65 μJ, 100 fs FWHM laser pulse is demonstrated above in Figure 6.2.

In the absence of an applied field, and after pressure equilibrium has been achieved, one can take the (appropriately scaled) integrated probe phase shift as a measure of the energy deposited into the system [127] according to

$$E_{absorbed} = -\frac{c_v T_0 \rho_0}{k(n-1)} \int \delta\phi(\mathbf{r}_\perp)\, \mathrm{d}^2\, \mathbf{r}_\perp \qquad (6.1)$$

where c_v is the specific heat of air at constant pressure, ρ_0, T_0 are the ambient gas density and temperature, $k = \frac{2\pi}{\lambda}$ is the probe wavenumber, and $(n-1)$ is the refractivity of the gas. The integrand $\delta\phi(\mathbf{r}_\perp)$ is the interferometrically measured probe phase shift, which is a function of $\mathbf{r}_\perp$, a vector in the plane transverse to the probe beam propagation.

6.4. Role of filament plasma in HV breakdown

It is useful to first assess the role of the laser produced plasma in the breakdown process and compare it to the role played by the hydrodynamic induced density depression. A first set of experiments was performed in which air density holes of the same depth were generated, either with or without initial plasma. In the case of a single filamenting pulse that generates plasma in the usual manner, the pulse energy was chosen (22 μJ) so that the resulting density hole had a relative depth of ~3% at a 1 μs delay after the pulse. In the plasma-free case, we used a resonant 8-pulse sequence of 12.5 μJ pulses (below the ionization threshold) from our pulse stacker to rotational heat the air's nitrogen molecules, also resulting in a relative density hole depth of ~3% at 1 μs. The intra-pulse timing in the sequence is adjusted to ~ 8.3 ps (the rotational revival time of N_2) in order to maximize the rotational ensemble excitation [74]. Such a configuration allows for the efficient pumping of molecular rotations, capable of producing a substantial gas heating in the absence of plasma production. (On the basis of the I^8 ionization dependence of molecular

oxygen on intensity, we expect the single pulse excitation to produce approximately $(22\ \mu J/12.5\ \mu J)^{8} \sim 90x$ as much plasma as the pulse sequence.)

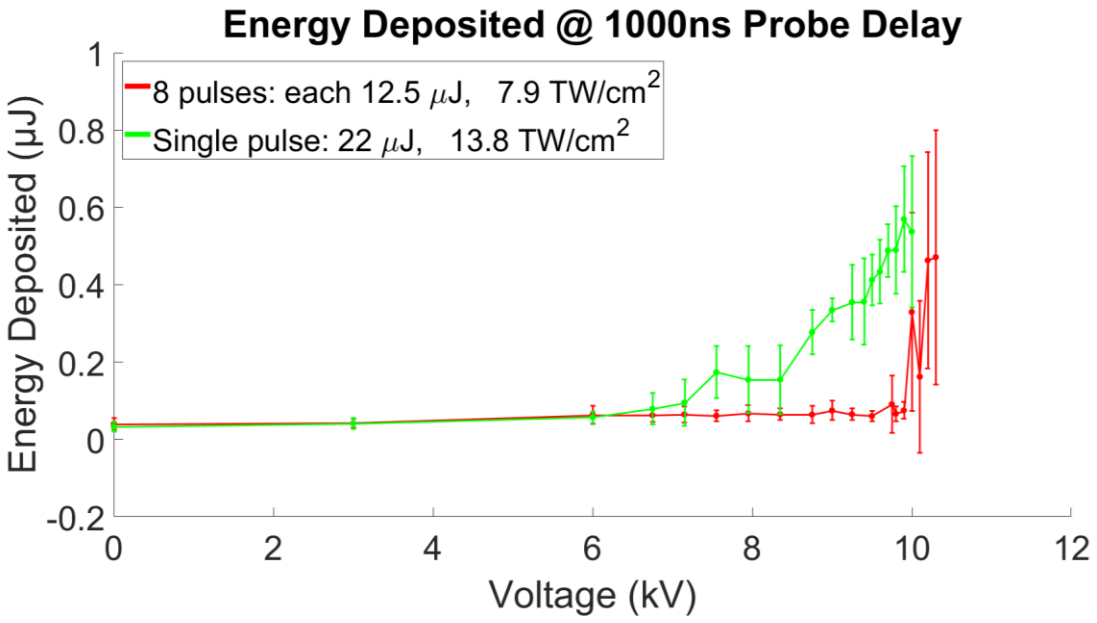

Figure 6.3 Energy deposited in the air as a function of high voltage for the case of no initial plasma (red curve) and an initial plasma present (green curve). The electrode spacing is 4 mm. For the case of no plasma, the air in the electrode gap was heated via rotational heating by a resonant 8-pulse sequence. For the case of plasma, a single laser pulse formed a filament between the electrodes. In both cases, the initial relative air density hole depth was ~3% at a delay of 1 μs.

Figure 6.3 plots the energy deposited in the gas between the electrodes (spaced at 4 mm) as a function of applied HV, calculated from the measured profile of the gas density depression at 1 μs after the laser pulse (using Eq. (6.1)). Each point is an average over 25 consecutive laser shots, while the error bars correspond to the standard deviation. All points in Figure 6.3 are *below* the breakdown voltage, and the curves terminate right at the location where breakdown occurs. It can be seen that the onset of increasing gas heating with voltage occurs at considerably lower voltage for the case of an initial plasma being present (from a single filamenting pulse). The case with initial plasma present exhibits behaviour consistent with additional Ohmic

heating by the HV source, (slow linear rise in energy absorption below ~6 kV) and an onset of avalanche in the range 6-10 kV, leading to HV breakdown (near where the curve terminates) at a lower voltage than the plasma free case. Future work will involve refining these experiments and understanding the results in more detail.

6.5. Single laser pulse energy dependence

In this section, we examine the HV dependence of inter-electrode gas heating on the energy of a single filamenting laser pulse which produces plasma.

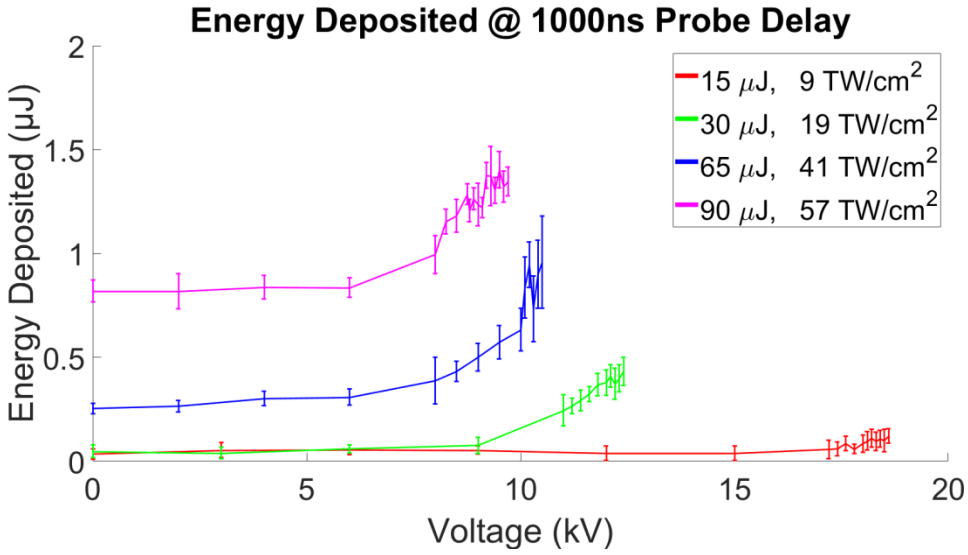

Figure 6.4 Interferometric measurements of the energy deposited at 1000 ns probe delay demonstrate the dependence of heating in response to differing input laser pulse energies prior to the breakdown of the spark gap. Plotted is a comparison of the energy deposition induced by four different single-pulse peak intensities in the presence of a range of DC HV fields.

Figure 6.4 plots energy deposition, again determined as in Eq. (6.1), as a function of HV for four laser pulse energies. It is seen that higher energy pulses initially deposit more energy in the air gap. For each curve, the energy deposition is seen to increase linearly with HV at first, consistent with Ohmic heating. Then there is a

nonlinear upturn, consistent with an electron avalanche, followed by breakdown, which occurs at lower voltages for the higher laser energies.

At higher voltages and closer to the breakdown threshold (where each curve abruptly ends), the heating (and thus energy deposition) appears to become exponential in the applied field, indicative of a runaway process which precedes the breakdown. This transition occurs at approximately (18, 12, 10, 8) kV for incident laser pulse energies of (15, 30, 65, 90) μJ, where the curves shown in Figure 6.4 begin to 'roll over'. This runaway heating can be attributed to the onset of an avalanche-like process occurring whereby laser produced electrons are sufficiently accelerated by the applied electric field to cause secondary impact ionization upon collision with neutrals.

It is instructive to consider the magnitude of Ohmic heating. If one models the electron as a point particle traversing a gas of hard-sphere scattering centers at standard atmospheric density, one can calculate the mean free path for an electron traversing a parcel of air to be ~400 nm. An electron starting from rest in a ~10 kV/cm field can then accelerate to ~1 eV in one mean free path. A Boltzmann distribution of electrons peaked at 1 eV has ~0.7% of its population at energies exceeding 12.1 eV, the collisional ionization energy threshold for molecular oxygen. In addition, a femtosecond filament–induced density hole of relative depth ~30% will increase the mean free path by ~30%, increasing the mean electron energy to ~1.3 eV, for which 2.5% of Boltzmann-distributed electrons have energy > 12.1 eV, more than three times the number observed for the distribution peaked at 1 eV.

6.6. *Effect of spark gap electrode separation*

In this section, we present results of changing the electrode separation while keeping the electric field constant and the laser pulse energy constant.

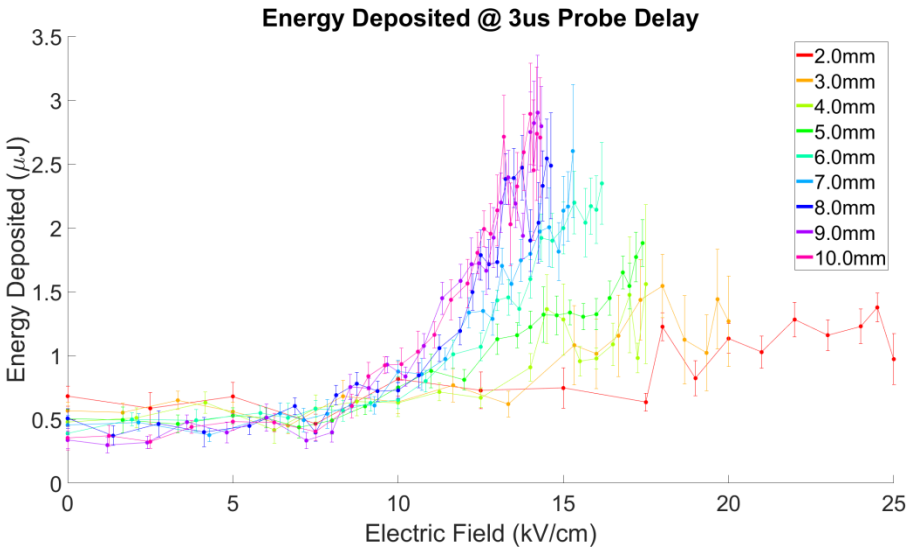

Figure 6.5 Energy deposited 3 μs after single laser pulse excitation in the presence of a variety of applied DC electric field strengths is measured for several spark gap electrode separations.

Figure 6.5 plots the energy deposited in the gap as a function of applied electric field for various electrode separations. Throughout all of these measurements, the confocal volume of the laser illumination remains 4 mm in length with a transverse size of the focal spot, w_0 = 23 μm. (Although it is likely that the laser produced plasma is generated over a slightly axially longer region owing to the onset of filamentation). Care was taken to ensure that the laser illumination was located directly in the central region of the gap, ensuring that for separations much longer than the laser's confocal parameter, no plasma was produced inside of the electrode tips. It is seen that for constant applied electric field the energy absorbed by the gas (or gas heating) increases with increased electrode separation. This is

consistent with Ohmic heating; the heated gas volume (for approximately similar gas conductivity) is simply larger in the case of wider-spaced electrodes. Note that for electrode spacing greater than 7 mm, the heating depends strongly on applied field but not on length, whereas for spacing less than 7 mm, heating depends more strongly on length than applied field. Below approximately ~8 kV, heating depends little on voltage or electrode spacing. We are currently refining these experiments to better understand these results.

6.7. Electric field simulations using Poisson solver

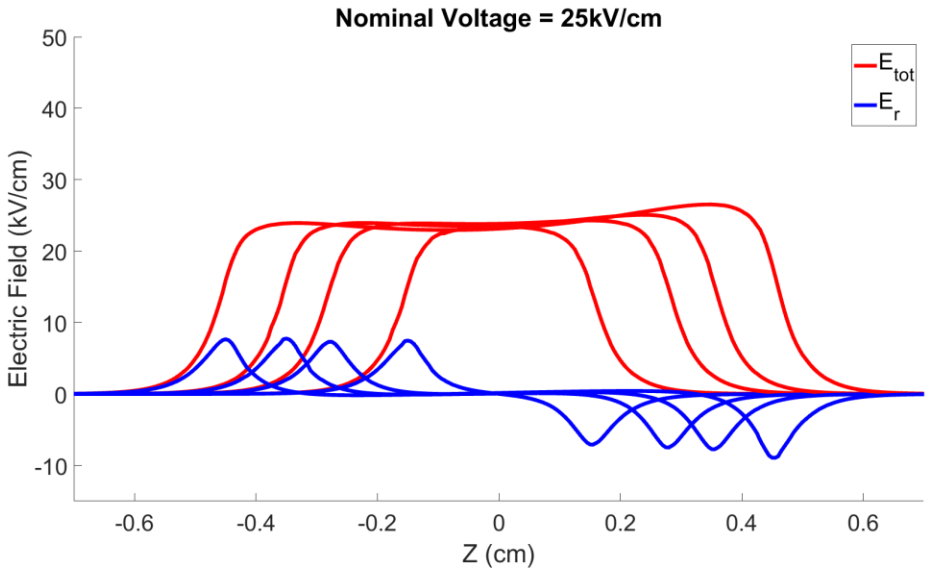

Figure 6.6 Electric field distributions for the various electrode spacings used in the experiments. Plotted are the total electric field and radial component of the total electric field calculated for a nominal voltage corresponding to 25 kV/cm. The electric fields were obtained by solving the 2D Laplace equation in radially symmetric coordinates with the freely available Poisson Superfish software.

Simulations of the electric field in the vicinity of the charged electrodes have been performed in order to visualize the features which govern the acceleration of the laser produced electrons. Figure 6.6 shows the results of a 2D radial Laplace equation

solver for the electric field in four of the separation cases shown in Figure 6.5. A 'nominal' electric field (25 kV/cm) and the measured electrode spacing are used to determine the voltage applied to the anode in each simulation. It is seen that in the region between the electrodes, the field is predominantly in the longitudinal direction, while the field does develop a slight radial component near the holes in the electrodes. This supports the idea that the HV electric field being applied to the laser produced electrons causes acceleration predominantly in the axial direction.

6.8. Inter-electrode gas heating versus time

In the absence of an applied electric field, and after the laser-heated gas achieves pressure equilibrium, the peak depth of the density hole decreases while its width increases, as the diffusion drives the gas towards equilibrium with the ambient air. Integrating the density hole profile at any later time gives a constant result proportional to the initial energy absorbed from the laser [127].

However when the HV is applied across the electrodes, the gas is heated continuously after initial laser energy deposition. Figure 6.7 shows plots of the gas heating as a function of time for a fixed laser pulse (65 μJ, 100 fs) and a range of HVs, and electrode spacing of 4 mm.

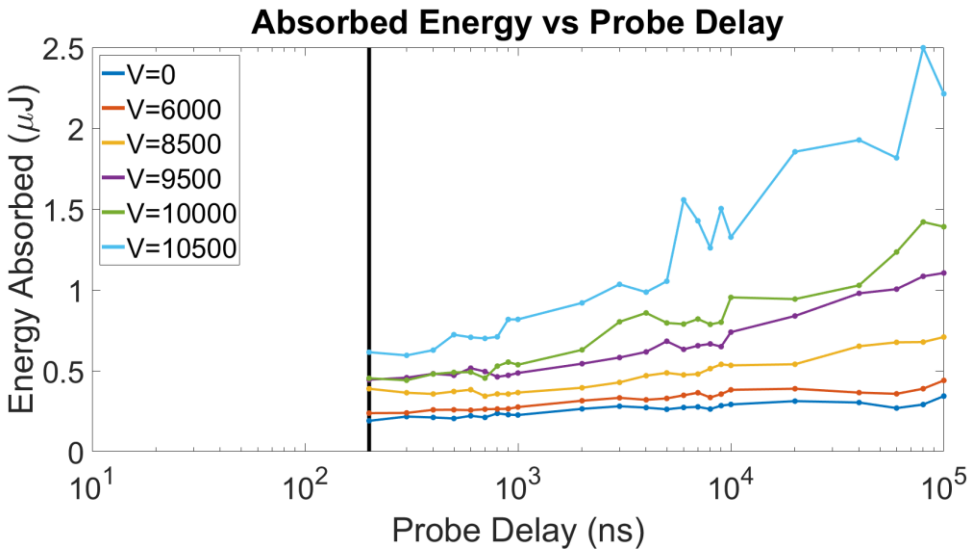

Figure 6.7 Energy absorbed by the gas is plotted as a function of probe delay for several DC electrode voltages between 0 V and 10.5 kV. The vertical bar corresponds to a probe delay of 200 ns, the point at which pressure balance is achieved in the absence of applied voltage. At higher voltages, not only does the initial depth of the density hole increase, owing to the transfer of energy from the field to the laser produced electrons, but the depth continues to increase out to the maximal probe delay measured of 100 μs.

The vertical bar corresponds to a probe delay of 200 ns, the point at which the acoustic wave has propagated away from the density hole, as seen in Figure 6.2 above. It is only after that time that the integrated interferometric phase shift of the density hole is an excellent proxy for absorbed energy.

At higher voltages, not only does the depth of the density hole at 200 ns increase, owing to short time heating by the HV source, but heating continues out to ~100 μs. This heating remains predominantly localized to the density hole region imprinted by the initial laser pulse, as seen in Figure 6.2(b).

6.9. Inducing electrical discharge using rotational revivals in air

In a next set of experiments, pulses in the pulse-train are timed to be either 'resonant', in which each pulse experiences the aligned molecules produced by the previous pulse, or 'off-resonant', in which each pulse experiences the anti-alignment which temporally precedes the full revival. These optimal delays correspond to two different points in the molecular alignment revival which occurs at approximately $t = \frac{1}{2cB} \approx 8.34$ ps after each pulse, where c is the speed of light in vacuum, and B is the molecule's rotational constant. The voltage at which the spark-gap undergoes dielectric breakdown is determined experimentally using a voltage slew method which consists of slowly raising the applied potential across the electrodes until dielectric breakdown is observed, in this case slowly enough so that consecutive laser shots at 10 Hz each see approximately the same voltage. For our purposes, it was determined that a slew-rate of ~1 V/ms was appropriate. Once the spark gap undergoes dielectric breakdown, the highest measured voltage prior to the breakdown is recorded. Voltage on the capacitor bank was measured using both a commercial high-voltage probe, and the on-board voltage monitor output of the power supply; both measurements were found to be in good quantitative agreement. The measurement of capacitor bank voltage immediately prior to breakdown is performed repeatedly in order to generate statistics such as the mean breakdown voltage and its statistical variance. The effects of pulse-sequence timing can be clearly seen in Figure 6.8, where we present measurements of this mean breakdown voltage, (denoted by the solid line) and the associated shot-to-shot variance, (denoted by the

dotted lines) for a spark-gap separation of ~8 mm. Using a train of eight pulses, each of 105 µJ and 81 fs FWHM, we observe a mean breakdown voltage of 15.7 kV or 14.6 kV, depending on whether the pulses were timed 'off-resonant', or 'on-resonant', representing a 7% decrease in the breakdown voltage. In each case, the shot-to-shot variance in the breakdown voltage was ~1.5%. For our choice of 8 mm electrode spacing, and in the absence of the laser pulse, dielectric breakdown could not be observed even up to ~25 kV, the highest voltage allowable by our setup.

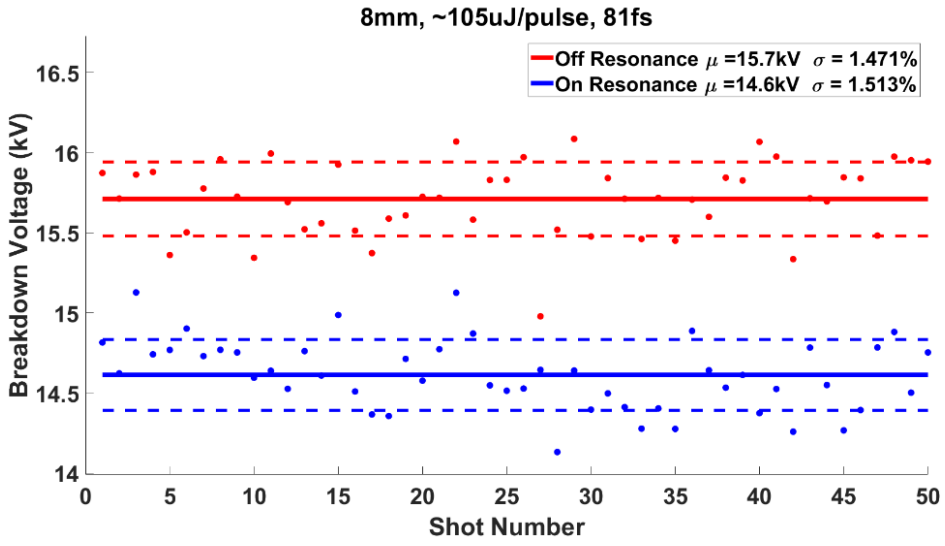

Figure 6.8 Measured dielectric breakdown voltage after application of an eight-pulse train whose pulses are timed to be either (a) resonant with the rotational revival of previous pulses in the train, shown in blue, or (b) non-resonant with the rotational revival of previous pulses in the train, shown in red.

Chapter 7: Summary and future work

7.1. Summary

Since its initial demonstration more than two decades ago, atmospheric filamentation of high intensity femtosecond laser pulses continues to be an area of considerable research interest. In addition to the rich basic physics involved in ultrashort pulse propagation, filaments have enabled or enhanced a wide variety of applications. In this thesis, femtosecond filamentation has been directed to new application areas. In particular, a novel method for laser beam waveguiding in the atmosphere, the 'air waveguide' has been demonstrated. This technique, in which arrays of femtosecond filaments are used to imprint patterns in the neutral air density, generates refractive index structures capable of guiding a separately injected laser beam, and shows promise for ranged propagation of high average power beams for directed energy applications.

Measurements presented in Chapter 2 demonstrate generation of femtosecond filament-induced air waveguides, and the guiding in these structures of secondary injected laser beams over ~15 Rayleigh ranges with up to ~90% throughput. Particular attention is paid to the measurement, analysis and simulation of the air hydrodynamic response to femtosecond filamentation –either by lowest order mode beams or high order transverse modes– which leads to air waveguide generation. In Chapter 3, experiments demonstrate the capability of air waveguides to act as broadband collection optics, enabling enhancement of signal-to-noise ratios in detection schemes requiring collection of remotely generated signals, such as laser induced breakdown spectroscopy (LIBS) and light detection and ranging (LIDAR).

These measurements, based on collection of isotropic light emission by ~ 1 m long air waveguides, imply a ~10^4 signal enhancement for air waveguides 100 meters in length. Even stronger enhancement would be expected in the case of directional signals of interest such as those produced by stimulated backscattering or backward lasing.

Crucial to the formation and utility of air waveguides is the energy deposition in the air by femtosecond filaments. This energy deposition and the resultant hydrodynamic response of the air were investigated using a variety of techniques including photodiode energy loss measurements, sonography, and time-resolved interferometric measurements of the evolving air density profile. These measurements, presented in Chapter 5, are supported by numerical simulations of nonlinear pulse propagation. In Chapter 4, the results of nonlinear pulse propagation simulations are compared to axially-resolved sonographic measurements of filament-induced acoustic wave generation to corroborate recently published measurements of the nonlinear refractive index of air (n_2). Finally, Chapter 6 presents preliminary measurements of the inter-electrode gas dynamics in a femtosecond pulse-triggered high voltage spark gap.

7.2. Future work

Much work remains to be done in order to realize the full capabilities of air waveguides. Experiments are currently underway to extend the range of our filament produced waveguides to ~50 meters. While the goal is to demonstrate guiding and

collection results analogous to those presented in Chapter 2 and Chapter 3, sufficient axial uniformity of the guides must be assured over extended distances. To this end, single-shot axially-resolved measurements of filament energy deposition will be measured using a ~50 meter long synchronized array of microphones.

In addition, the preliminary measurements presented in Chapter 6 of the dynamics leading to air breakdown in a laser triggered spark gap are currently being refined. A two-color interferometer is being employed to distinguish between the contributions of neutral gas and plasma density profiles to the dynamics leading to breakdown of the spark gap. Measurements of the electric current passing through the electrodes both prior to and during the discharge will be measured and analyzed, enabling further understanding of air dynamics in the electrode gap.

7.3. Publications by the candidate

The main results presented in this thesis have been published in a variety of peer reviewed research journals and conference proceedings, shown below. The results of Chapter 6 are in preparation for publication.

Peer Reviewed Journal Articles:

1) **E. W. Rosenthal**, N. Jhajj, I. Larkin, S. Zahedpour, J. K. Wahlstrand, H. M. Milchberg, "Energy deposition of single femtosecond filaments in the atmosphere," Optics Letters **41** (16) 3908 (2016).

2) **E. W. Rosenthal**, J. P. Palastro, N. Jhajj, S. Zahedpour, J. K. Wahlstrand, H. M. Milchberg, "Sensitivity of propagation and energy deposition in

femtosecond filamentation to the nonlinear refractive index," Journal of Physics B: Atomic, Molecular and Optical Physics **48** (9), 094011 (2015).

3) **E. W. Rosenthal**, N. Jhajj, J. K. Wahlstrand, H. M. Milchberg, "Collection of remote optical signals by air waveguides," Optica **1** (1), 5 (2014)

4) N. Jhajj, **E. W. Rosenthal**, R. Birnbaum, J. K. Wahlstrand, H. M. Milchberg, "Demonstration of long-lived high-power optical waveguides in air," Physical Review X **4** (1), 011027 (2014)

5) N. Jhajj, I. Larkin, **E. W. Rosenthal**, S. Zahedpour, J. K. Wahlstrand, H. M. Milchberg, "Spatio-temporal optical vortices," Physical Review X **6**, 031037 (2016).

6) T. I. Oh, Y. S. You, N. Jhajj, **E. W. Rosenthal**, H. M. Milchberg, K. Y. Kim, "Intense terahertz generation in two-color laser filamentation: energy scaling with terawatt laser systems," New Journal of Physics **15** (7), 075002 (2013)

7) J. K. Wahlstrand, N. Jhajj, **E. W. Rosenthal**, S. Zahedpour, H. M. Milchberg, "Direct measurement of the acoustic waves generated by femtosecond filaments," Optics Letters **39** (5), 1290 (2014)

8) T. I. Oh, Y. S. You, N. Jhajj, **E. W. Rosenthal**, H. M. Milchberg, "Scaling and saturation of high-power terahertz radiation generation in two-color laser filamentation," Applied Physics Letters **102** (20), 201113 (2013)

9) S. Varma, Y. –H. Chen, J. P. Palastro, A. B. Fallahkair, **E. W. Rosenthal**, H. M. Milchberg, "Molecular quantum wake-induced pulse shaping and extension of femtosecond air filaments," Physical Review A **86** (2), 023850 (2012)

10) H. M. Milchberg, Y. –H. Chen, Y. –H. Cheng, N. Jhajj, J. P. Palastro, **E. W. Rosenthal**, S. Varma, J. K. Wahlstrand, S. Zahedpour, "The extreme nonlinear optics of gases and femtosecond filamentation," Physics of Plasmas **21**, 10091 (2014)

11) D. Kuk, Y. J. Yoo, **E. W. Rosenthal**, N. Jhajj, H. M. Milchberg, K. Y. Kim, "Generation of scalable terahertz radiation from cylindrically focused two-color laser pulses in air," Applied Physics Letters **108** (12), 121106 (2016)

Conference Proceedings:

12) **E. W. Rosenthal**, N. Jhajj, I. Larkin, S. Zahedpour, J. K. Wahlstrand, and H. M. Milchberg, "Energy deposition of single femtosecond filaments in the atmosphere," *Poster presented at ISUILS15: International Symposium on Ultrafast Laser Science, Oct. 2nd-7th 2016, Cassis, France.*

13) **E. W. Rosenthal**, N. Jhajj, I. Larkin, S. Zahedpour, J. K. Wahlstrand, and H. M. Milchberg, "Energy deposition of single femtosecond filaments in the atmosphere," *Poster presented at COFIL2016: 6th International Symposium on Filamentation, Sept. 5th-9th 2016, Quebec City, QC, Canada.*

14) **E. W. Rosenthal**, I. Larkin, N. Jhajj, S. Zahedpour, J. Wahlstrand, and H. Milchberg, "Atmospheric Energy Absorption in Single Filamentation," in *Propagation Through and Characterization of Atmospheric and Oceanic Phenomena*, OSA Technical Digest (online) (Optical Society of America, 2016), paper Tu2A.4.

15) **E. W. Rosenthal**, I. Larkin, N. Jhajj, S. Zahedpour, J. Wahlstrand, and H. M. Milchberg, "Energy Absorption in Femtosecond Filamentation," in *High-Brightness Sources and Light-Driven Interactions*, OSA Technical Digest (online) (Optical Society of America, 2016), paper HS4B.7.

16) **E. W. Rosenthal**, N. Jhajj, R. Birnbaum and H. M. Milchberg, "Enhanced spectral broadening and beam collimation from pulse-sequence induced filamentation," *2014 Conference on Lasers and Electro-Optics (CLEO) - Laser Science to Photonic Applications*, San Jose, CA, 2014, pp. 1-2.

17) **E. W. Rosenthal**, N. Jhajj, J. K. Wahlstrand and H. M. Milchberg, "Collection of remote optical signals by air waveguides," *2014 Conference on Lasers and Electro-Optics (CLEO) - Laser Science to Photonic Applications*, San Jose, CA, 2014, pp. 1-2.

18) **E. W. Rosenthal**, "Remote Collection of Optical Signals using Air Waveguides," in *Frontiers in Optics 2014*, OSA Technical Digest (online) (Optical Society of America, 2014), paper LW4I.4.

Bibliography

[1] J. K. Wahlstrand, Y.-H. Cheng, and H. M. Milchberg, "Absolute measurement of the transient optical nonlinearity in N_2, O_2, N_2O, and Ar," *Phys. Rev. A*, vol. 85, no. 4, p. 43820, Apr. 2012.

[2] D. P. Shelton and J. E. Rice, "Measurements and Calculations of the Hyperpolarizabilities of Atoms and Small Molecules in the Gas Phase," *Chem. Rev.*, vol. 94, no. 1, pp. 3–29, 1994.

[3] R. W. Boyd, *Nonlinear Optics*, 3rd Edition. Academic Press, 2008.

[4] J. K. Wahlstrand, Y. H. Cheng, Y. H. Chen, and H. M. Milchberg, "Optical nonlinearity in Ar and N_2 near the ionization threshold," *Phys. Rev. Lett.*, vol. 107, no. 10, pp. 1–5, 2011.

[5] J. K. Wahlstrand, Y. H. Cheng, and H. M. Milchberg, "High field optical nonlinearity and the Kramers-Kronig relations," *Phys. Rev. Lett.*, vol. 109, no. 11, pp. 1–5, 2012.

[6] Y.-H. Chen, S. Varma, I. Alexeev, and H. Milchberg, "Measurement of transient nonlinear refractive index in gases using xenon supercontinuum single-shot spectral interferometry," *Opt. Express*, vol. 15, no. 12, p. 7458, 2007.

[7] Y. Shimoji, A. T. Fay, R. S. F. Chang, and N. Djeu, "Direct measurement of the nonlinear refractive index of air," *J. Opt. Soc. Am. B*, vol. 6, no. 11, p. 1994, 1989.

[8] M. J. Shaw C. J. Hooker, D. C. Wilson, M. J. Shaw, and C. J. Hooker, "Measurement of the nonlinear refractive index of air and other gases at 248

nm," *Opt. Commun.*, vol. 103, p. 153, 1993.

[9] J. K. Wahlstrand, S. Zahedpour, Y.-H. Cheng, J. P. Palastro, and H. M. Milchberg, "Absolute measurement of the ultrafast nonlinear electronic and rovibrational response in H_2 and D_2," *Phys. Rev. A*, vol. 92, no. 6, p. 63828, 2015.

[10] S. Zahedpour, J. K. Wahlstrand, and H. M. Milchberg, "Measurement of the nonlinear refractive index of air constituents at mid-infrared wavelengths," *Opt. Lett.*, vol. 40, no. 24, p. 5794, 2015.

[11] K. Y. Kim, I. Alexeev, and H. M. Milchberg, "Single-shot supercontinuum spectral interferometry," *Appl. Phys. Lett.*, vol. 81, no. 22, pp. 4124–4126, 2002.

[12] L. V. Keldysh, "Ionization in the field of a strong electromagnetic wave," *Sov. Phys. JETP*, vol. 20, no. 5, pp. 1307–1314, 1965.

[13] A. Couairon, S. Tzortzakis, L. Bergé, M. Franco, B. Prade, and A. Mysyrowicz, "Infrared femtosecond light filaments in air: simulations and experiments," *J. Opt. Soc. Am. B*, vol. 19, no. 5, pp. 1117–1131, 2002.

[14] L. Bergé, S. Skupin, R. Nuter, J. Kasparian, and J.-P. Wolf, "Ultrashort filaments of light in weakly ionized, optically transparent media," *Reports Prog. Phys.*, vol. 70, no. 10, pp. 1633–1713, 2007.

[15] A. Couairon and A. Mysyrowicz, "Femtosecond filamentation in transparent media," *Phys. Rep.*, vol. 441, no. 2–4, pp. 47–189, Mar. 2007.

[16] Y.-H. Chen, S. Varma, T. Antonsen, and H. Milchberg, "Direct Measurement of the Electron Density of Extended Femtosecond Laser Pulse-Induced

Filaments," *Phys. Rev. Lett.*, vol. 105, no. 21, p. 215005, Nov. 2010.

[17] J. K. Wahlstrand, Y.-H. Cheng, Y.-H. Chen, and H. M. Milchberg, "Optical Nonlinearity in Ar and N_2 near the Ionization Threshold," *Phys. Rev. Lett.*, vol. 107, no. 10, p. 103901, Aug. 2011.

[18] J. Wahlstrand, Y.-H. Cheng, and H. Milchberg, "High Field Optical Nonlinearity and the Kramers-Kronig Relations," *Phys. Rev. Lett.*, vol. 109, no. 11, p. 113904, Sep. 2012.

[19] A. Braun, G. Korn, X. Liu, D. Du, J. Squier, and G. Mourou, "Self-channeling of high-peak-power femtosecond laser pulses in air.," *Opt. Lett.*, vol. 20, no. 1, pp. 73–75, 1995.

[20] H. Pépin, D. Comtois, F. Vidal, C. Y. Chien, A. Desparois, T. W. Johnston, J. C. Kieffer, B. La Fontaine, F. Martin, F. A. M. Rizk, C. Potvin, P. Couture, H. P. Mercure, A. Bondiou-Clergerie, P. Lalande, and I. Gallimberti, "Triggering and guiding high-voltage large-scale leader discharges with sub-joule ultrashort laser pulses," *Phys. Plasmas*, vol. 8, no. 5 II, pp. 2532–2539, 2001.

[21] N. Zhavoronkov, "Efficient spectral conversion and temporal compression of femtosecond pulses in SF_6," *2011 Conf. Lasers Electro-Optics Eur. 12th Eur. Quantum Electron. Conf. CLEO Eur. 2011*, p. 2489, 2011.

[22] C. P. Hauri, W. Kornelis, F. W. Helbing, A. Heinrich, A. Couairon, A. Mysyrowicz, J. Biegert, and U. Keller, "Generation of intense, carrier-envelope phase-locked few-cycle laser pulses through filamentation," *Appl. Phys. B Lasers Opt.*, vol. 79, no. 6, pp. 673–677, 2004.

[23] S. Skupin, G. Stibenz, L. Bergé, F. Lederer, T. Sokollik, M. Schnürer, N.

Zhavoronkov, and G. Steinmeyer, “Self-compression by femtosecond pulse filamentation: Experiments versus numerical simulations,” *Phys. Rev. E - Stat. Nonlinear, Soft Matter Phys.*, vol. 74, no. 5, pp. 1–9, 2006.

[24] O. Varela, B. Alonso, I. J. Sola, J. San Román, A. Zaïr, C. Méndez, and L. Roso, “Self-compression controlled by the chirp of the input pulse.,” *Opt. Lett.*, vol. 35, no. 21, pp. 3649–51, 2010.

[25] P.B. Corkum, C. Rolland, and T. Srinivasan-Rao, “Supercontinuum Generation in Gases,” *Phys. Rev. Lett.*, vol. 57, no. 18, p. 2268, 1986.

[26] K. Stelmaszczyk, P. Rohwetter, G. Méjean, J. Yu, E. Salmon, J. Kasparian, R. Ackermann, J. P. Wolf, and L. Wöste, “Long-distance remote laser-induced breakdown spectroscopy using filamentation in air,” *Appl. Phys. Lett.*, vol. 85, no. 18, pp. 3977–3979, 2004.

[27] K.-Y. Kim, J. H. Glownia, A. J. Taylor, and G. Rodriguez, “Terahertz emission from ultrafast ionizing air in symmetry-broken laser fields,” *Opt. Express*, vol. 15, no. 8, p. 4577, 2007.

[28] K. Y. Kim, A. J. Taylor, J. H. Glownia, and G. Rodriguez, “Coherent control of terahertz supercontinuum generation in ultrafast laser–gas interactions,” *Nat. Photonics*, vol. 2, no. 10, pp. 605–609, 2008.

[29] C. D’Amico, A. Houard, M. Franco, B. Prade, A. Mysyrowicz, A. Couairon, and V. T. Tikhonchuk, “Conical forward THz emission from femtosecond-laser-beam filamentation in air,” *Phys. Rev. Lett.*, vol. 98, no. 23, pp. 8–11, 2007.

[30] N. Jhajj, E. W. Rosenthal, R. Birnbaum, J. K. Wahlstrand, and H. M.

Milchberg, “Demonstration of Long-Lived High-Power Optical Waveguides in Air,” *Phys. Rev. X*, vol. 4, no. 1, p. 11027, 2014.

[31] E. W. Rosenthal, N. Jhajj, J. K. Wahlstrand, and H. Milchberg, “Collection of remote optical signals by air waveguides,” *Optica*, vol. 1, no. 1, p. 5, 2014.

[32] A. Couairon and L. Bergé, “Modeling the filamentation of ultra-short pulses in ionizing media,” *Phys. Plasmas*, vol. 7, no. 1, pp. 193–209, 2000.

[33] H. Gao, W. Chu, G. Yu, B. Zeng, J. Zhao, Z. Wang, W. Liu, Y. Cheng, and Z. Xu, “Femtosecond laser filament array generated with step phase plate in air,” *Opt. Express*, vol. 21, no. 4, pp. 4612–4622, 2013.

[34] A. Camino, Z. Hao, X. Liu, and J. Lin, “Control of laser filamentation in fused silica by a periodic microlens array.,” *Opt. Express*, vol. 21, no. 7, pp. 7908–15, 2013.

[35] P.-P. Li, M.-Q. Cai, J.-Q. Lü, D. Wang, G.-G. Liu, S.-X. Qian, Y. Li, C. Tu, and H.-T. Wang, “Control of femtosecond multi-filamentation in glass by designable patterned optical fields,” *AIP Adv.*, vol. 6, no. 12, p. 125103, 2016.

[36] M. Rodriguez, R. Bourayou, G. Méjean, J. Kasparian, J. Yu, E. Salmon, A. Scholz, B. Stecklum, J. Eislöffel, U. Laux, A. P. Hatzes, R. Sauerbrey, L. Wöste, and J. P. Wolf, “Kilometer-range nonlinear propagation of femtosecond laser pulses,” *Phys. Rev. E - Stat. Nonlinear, Soft Matter Phys.*, vol. 69, no. 3 2, pp. 1–7, 2004.

[37] P. Sprangle, J. Peñano, and B. Hafizi, “Optimum wavelength and power for efficient laser propagation in various atmospheric environments,” *J. Dir. Energy*, vol. 2, no. 1, pp. 71–95, 2006.

[38] P. Sprangle, J. Peñano, B. Hafizi, D. Gordon, and M. Scully, “Remotely induced atmospheric lasing,” *Appl. Phys. Lett.*, vol. 98, no. 21, pp. 1–4, 2011.

[39] J. Kasparian, M. Rodriguez, G. Méjean, J. Yu, E. Salmon, H. Wille, R. Bourayou, S. Frey, Y.-B. André, A. Mysyrowicz, R. Sauerbrey, J.-P. Wolf, and L. Wöste, “White-Light Filaments for Atmospheric Analysis,” *Science*, vol. 301, no. 5629, pp. 61–64, 2003.

[40] P. Rairoux, H. Schillinger, S. Niedermeier, M. Rodriguez, F. Ronneberger, R. Sauerbrey, B. Stein, D. Waite, C. Wedekind, H. Wille, L. Wöste, and C. Ziener, “Remote sensing of the atmosphere using ultrashort laser pulses,” *Appl. Phys. B Lasers Opt.*, vol. 71, no. 4, pp. 573–580, 2000.

[41] J. Liu, J. Dai, S. L. Chin, and X.-C. Zhang, “Broadband terahertz wave remote sensing using coherent manipulation of fluorescence from asymmetrically ionized gases,” *Nat. Photonics*, vol. 4, no. 9, pp. 627–631, 2010.

[42] K. W. Fischer, M. R. Witiw, J. A. Baars, and T. R. Oke, “Atmospheric laser communication new challenges for applied meteorology,” *Bull. Am. Meteorol. Soc.*, vol. 85, no. 5, pp. 725–732, 2004.

[43] P. Panagiotopoulos, N. K. Efremidis, D. G. Papazoglou, A. Couairon, and S. Tzortzakis, “Tailoring the filamentation of intense femtosecond laser pulses with periodic lattices,” *Phys. Rev. A - At. Mol. Opt. Phys.*, vol. 82, no. 6, pp. 1–4, 2010.

[44] M. Bellec, P. Panagiotopoulos, D. G. Papazoglou, N. K. Efremidis, A. Couairon, and S. Tzortzakis, “Observation and optical tailoring of photonic lattice filaments,” *Phys. Rev. Lett.*, vol. 109, no. 11, pp. 1–5, 2012.

[45] S. Suntsov, D. Abdollahpour, D. G. Papazoglou, P. Panagiotopoulos, A. Couairon, and S. Tzortzakis, “Tailoring femtosecond laser pulse filamentation using plasma photonic lattices,” *Appl. Phys. Lett.*, vol. 103, no. 2, pp. 1–4, 2013.

[46] R. R. Musin, M. N. Shneider, A. M. Zheltikov, and R. B. Miles, “Guiding radar signals by arrays of laser-induced filaments: finite-difference analysis,” *Appl. Opt.*, vol. 46, no. 23, pp. 5593–5597, 2007.

[47] M. Châteauneuf, S. Payeur, J. Dubois, and J. C. Kieffer, “Microwave guiding in air by a cylindrical filament array waveguide,” *Appl. Phys. Lett.*, vol. 92, no. 9, pp. 1–4, 2008.

[48] S.-B. Wen, C.-F. Chen, X. Mao, and R. E. Russo, “Guiding and focusing of a nanosecond infrared laser within transient hollow plasma femtosecond filament channels,” *J. Phys. D. Appl. Phys.*, vol. 45, no. 35, p. 355203, 2012.

[49] Y.-H. Cheng, J. K. Wahlstrand, N. Jhajj, and H. M. Milchberg, “The effect of long timescale gas dynamics on femtosecond filamentation,” *Opt. Express*, vol. 21, no. 4, pp. 4740–4751, 2013.

[50] K. Kim, I. Alexeev, and H. Milchberg, “Single-shot measurement of laser-induced double step ionization of helium,” *Opt. Express*, vol. 10, no. 26, pp. 1563–1572, 2002.

[51] L. Levi, O. Lahav, R. A. Nemirovsky, J. Nemirovsky, I. Orr, I. Kaminer, M. Segev, and O. Cohen, “Long-Lived Waveguides and Sound Wave Generation by Laser Filamentation,” *arXiv*, p. 1307.3588, 2013.

[52] J. K. Wahlstrand, N. Jhajj, E. W. Rosenthal, S. Zahedpour, and H. M.

Milchberg, “Direct imaging of the acoustic waves generated by femtosecond filaments in air,” *Opt. Lett.*, vol. 39, no. 5, pp. 1290–1293, 2014.

[53] A. W. Snyder and J. D. Love, *Optical Waveguide Theory*. London: Chapman and Hall, 1991.

[54] K. P. Birch, “Precise determination of refractometric parameters for atmospheric gases,” *J. Opt. Soc. Am. A*, vol. 8, no. 4, p. 647, 1991.

[55] NIST, “Thermophysical Properties of Fluid Systems,” *NIST Chemistry WebBook, SRD 69*. [Online]. http://webbook.nist.gov/chemistry/fluid/.

[56] M. D. Feit and J. A. Fleck, “Light propagation in graded-index optical fibers,” *Appl. Opt.*, vol. 17, no. 24, p. 3990, 1978.

[57] V. V. Vorob’ev, “Thermal blooming of laser beams in the atmosphere,” *Prog. Quantum Electron.*, vol. 15, no. 1–2, pp. 1–152, 1991.

[58] P. N. Malevich, D. Kartashov, Z. Pu, S. Ališauskas, A. Pugžlys, A. Baltuška, L. Giniūnas, R. Danielius, A. A. Lanin, A. M. Zheltikov, M. Marangoni, and G. Cerullo, “Ultrafast-laser-induced backward stimulated Raman scattering for tracing atmospheric gases,” *Opt. Express*, vol. 20, no. 17, p. 18784, 2012.

[59] P. Rohwetter, J. Yu, G. Méjean, K. Stelmaszczyk, E. Salmon, J. Kasparian, J.-P. Wolf, L. Wöste, “Remote LIBS with ultrashort pulses: characteristics in picosecond and femtosecond regimes,” *J. Anal. At. Spectrom.*, vol. 19, pp. 437–444, 2004.

[60] M. Scheller, M. S. Mills, M.-A. Miri, W. Cheng, J. V. Moloney, M. Kolesik, P. Polynkin, and D. N. Christodoulides, “Externally refuelled optical filaments,” *Nat. Photonics*, vol. 8, no. 4, pp. 297–301, 2014.

[61] S. Varma, Y.-H. Chen, J. Palastro, A. Fallahkair, E. W. Rosenthal, T. Antonsen, and H. Milchberg, "Molecular quantum wake-induced pulse shaping and extension of femtosecond air filaments," *Phys. Rev. A*, vol. 86, no. 2, p. 23850, Aug. 2012.

[62] J. Scaffidi, J. Pender, W. Pearman, S. R. Goode, B. W. Colston, J. C. Carter, and S. M. Angel, "Dual-pulse laser-induced breakdown spectroscopy with combinations of femtosecond and nanosecond laser pulses.," *Appl. Opt.*, vol. 42, no. 30, pp. 6099–6106, 2003.

[63] D. S. Steingrube, E. Schulz, T. Binhammer, M. B. Gaarde, A. Couairon, U. Morgner, and M. Kovačev, "High-order harmonic generation directly from a filament," *New J. Phys.*, vol. 13, 2011.

[64] E. T. J. Nibbering, G. Grillon, M. a. Franco, B. S. Prade, and a. Mysyrowicz, "Determination of the inertial contribution to the nonlinear refractive index of air, N_2, and O_2 by use of unfocused high-intensity femtosecond laser pulses," *J. Opt. Soc. Am. B*, vol. 14, no. 3, p. 650, 1997.

[65] V. Loriot, E. Hertz, O. Faucher, and B. Lavorel, "Measurement of high order Kerr refractive index of major air components: erratum.," *Opt. Express*, vol. 18, no. 3, pp. 3011–3012, 2010.

[66] J.-F. Ripoche, G. Grillon, B. Prade, M. Franco, E. Nibbering, R. Lange, and A. Mysyrowicz, "Determination of the time dependence of n_2 in air," *Opt. Commun.*, vol. 135, no. 4–6, pp. 310–314, 1997.

[67] V. Loriot, E. Hertz, O. Faucher, and B. Lavorel, "Measurement of high order Kerr refractive index of major air components: erratum.," *Opt. Express*, vol.

17, no. 16, p. 13429, 2009.

[68] J. K. Wahlstrand and H. M. Milchberg, “Effect of a plasma grating on pump-probe experiments near the ionization threshold in gases.,” *Opt. Lett.*, vol. 36, no. 19, pp. 3822–4, Oct. 2011.

[69] J. K. Wahlstrand, J. H. Odhner, E. T. McCole, Y. H. Cheng, J. P. Palastro, R. J. Levis, and H. M. Milchberg, “Effect of two-beam coupling in strong-field optical pump-probe experiments,” *Phys. Rev. A - At. Mol. Opt. Phys.*, vol. 87, no. 5, pp. 1–13, 2013.

[70] Chen, Y.-H., Varma, S., York, A., Milchberg, H., “Single-shot, space- and time-resolved measurement of rotational wavepacket revivals in H_2, D_2, N_2, O_2, and N_2O,” *Opt. Express*, vol. 15, no. 18, p. 11341, 2007.

[71] Y.-H. Chen, S. Varma, I. Alexeev, and H. Milchberg, “Measurement of transient nonlinear refractive index in gases using xenon supercontinuum single-shot spectral interferometry.,” *Opt. Express*, vol. 15, no. 12, pp. 7458–67, Jun. 2007.

[72] Á. Börzsönyi, Z. Heiner, A. P. Kovács, M. P. Kalashnikov, and K. Osvay, “Measurement of pressure dependent nonlinear refractive index of inert gases,” *Opt. Express*, vol. 18, no. 25, p. 25847, 2010.

[73] O. A. Bukin, E. E. Bykova, Y. E. Geints, S. S. Golik, A. A. Zemlyanov, A. A. Ilyin, A. M. Kabanov, G. G. Matvienko, V. K. Oshlakov, and E. B. Sokolova, “Filamentation of a sharply focused ultrashort laser pulse at wavelengths of 800 and 400 nm: Measurements of the nonlinear index of air refraction,” *Atmos. Ocean. Opt.*, vol. 24, no. 5, pp. 417–424, 2011.

[74] S. Zahedpour, J. K. Wahlstrand, and H. M. Milchberg, “Quantum control of molecular gas hydrodynamics,” *Phys. Rev. Lett.*, vol. 112, no. 14, pp. 1–5, 2014.

[75] J. Palastro, T. Antonsen, S. Varma, Y.-H. Chen, and H. Milchberg, “Simulations of femtosecond atmospheric filaments enhanced by dual pulse molecular alignment,” *Phys. Rev. A*, vol. 85, no. 4, p. 43843, Apr. 2012.

[76] J. Yu, D. Mondelain, J. Kasparian, E. Salmon, S. Geffroy, C. Favre, V. Boutou, and J.-P. Wolf, “Sonographic probing of laser filaments in air,” *Appl. Opt.*, vol. 42, no. 36, pp. 7117–20, 2003.

[77] Z.-Y. Zheng, J. Zhang, Z.-Q. Hao, Z. Zhang, M. Chen, X. Lu, Z.-H. Wang, and Z.-Y. Wei, “Paper airplane propelled by laser plasma channels generated by femtosecond laser pulses in air.,” *Opt. Express*, vol. 13, no. 26, pp. 10616–10621, 2005.

[78] D. V. Kartashov, A. V. Kirsanov, A. M. Kiselev, A. N. Stepanov, N. N. Bochkarev, Y. N. Ponomarev, and B. A. Tikhomirov, “Nonlinear absorption of intense femtosecond laser radiation in air,” *Opt. Express*, vol. 14, no. 17, p. 7552, 2006.

[79] B. Clough, J. Liu, and X.-C. Zhang, “Laser-induced photoacoustics influenced by single-cycle terahertz radiation,” *Opt. Lett.*, vol. 35, no. 21, pp. 3544–3546, 2010.

[80] R. P. Fischer, A. C. Ting, D. F. Gordon, R. F. Fernsler, G. P. DiComo, and P. Sprangle, “Conductivity Measurements of Femtosecond Laser Plasma Filaments,” *IEEE Trans. Plasma Sci.*, vol. 35, no. 5, pp. 1430–1436, 2007.

[81] F. Théberge, W. Liu, P. T. Simard, A. Becker, and S. L. Chin, “Plasma density inside a femtosecond laser filament in air: Strong dependence on external focusing,” *Phys. Rev. E - Stat. Nonlinear, Soft Matter Phys.*, vol. 74, no. 3, pp. 1–7, 2006.

[82] S. Tzortzakis, B. Prade, M. Franco, and A. Mysyrowicz, “Time-evolution of the plasma channel at the trail of a self-guided IR femtosecond laser pulse in air,” *Opt. Commun.*, vol. 181, no. 1, pp. 123–127, 2000.

[83] G. Rodriguez, A. R. Valenzuela, B. Yellampalle, M. J. Schmitt, and K.-Y. Kim, “In-line holographic imaging and electron density extraction of ultrafast ionized air filaments,” *J. Opt. Soc. Am. B*, vol. 25, no. 12, p. 1988, 2008.

[84] S. Eisenmann, A. Pukhov, and A. Zigler, “Fine Structure of a Laser-Plasma Filament in Air,” *Phys. Rev. Lett.*, vol. 98, no. 15, p. 155002, 2007.

[85] P. Polynkin and M. Kolesik, “Critical power for self-focusing in the case of ultrashort laser pulses,” *Phys. Rev. A - At. Mol. Opt. Phys.*, vol. 87, no. 5, pp. 1–5, 2013.

[86] J. P. Palastro, T. M. Antonsen, and H. M. Milchberg, “Compression, spectral broadening, and collimation in multiple, femtosecond pulse filamentation in atmosphere,” *Phys. Rev. A - At. Mol. Opt. Phys.*, vol. 86, no. 3, pp. 1–7, 2012.

[87] J. P. Palastro, “Time-dependent polarization states of high-power, ultrashort laser pulses during atmospheric propagation,” *Phys. Rev. A - At. Mol. Opt. Phys.*, vol. 89, no. 1, pp. 1–7, 2014.

[88] I. Alexeev, A. Ting, D. F. Gordon, E. Briscoe, J. R. Penano, R. F. Hubbard, and P. Sprangle, “Longitudinal compression of short laser pulses in air,” *Appl.*

Phys. Lett., vol. 84, no. 20, pp. 4080–4082, 2004.

[89] S. V. Popruzhenko, V. D. Mur, V. S. Popov, and D. Bauer, "Strong field ionization rate for arbitrary laser frequencies," *Phys. Rev. Lett.*, vol. 101, no. 19, pp. 1–4, 2008.

[90] N. H. Burnett and P. B. Corkum, "Cold-plasma production for recombination extremeultraviolet lasers by optical-field-induced ionization," *J. Opt. Soc. Am. B*, vol. 6, no. 6, p. 1195, 1989.

[91] E. W. Rosenthal, J. P. Palastro, N. Jhajj, S. Zahedpour, J. K. Wahlstrand, and H. M. Milchberg, "Sensitivity of propagation and energy deposition in femtosecond filamentation to the nonlinear refractive index," *J. Phys. B At. Mol. Opt. Phys.*, vol. 48, no. 9, p. 94011, 2015.

[92] P. Sprangle, J. Peñano, and B. Hafizi, "Propagation of intense short laser pulses in the atmosphere," *Phys. Rev. E*, vol. 66, no. 4, p. 46418, Oct. 2002.

[93] W. Liu, Q. Luo, F. Théberge, H. L. Xu, S. A. Hosseini, S. M. Sarifi, and S. L. Chin, "The influence of divergence on the filament length during the propagation of intense ultra-short laser pulses," *Appl. Phys. B Lasers Opt.*, vol. 82, no. 3, pp. 373–376, 2006.

[94] M. V. Chegotov, "Ionization modulation of a short intensive laser pulse," *J. Phys. D. Appl. Phys.*, vol. 35, no. 7, pp. 647–657, 2002.

[95] G. Point, E. Thouin, A. Mysyrowicz, and A. Houard, "Energy deposition from focused terawatt laser pulses in air undergoing multifilamentation," *Opt. Express*, vol. 24, no. 6, p. 6271, 2016.

[96] G. Point, C. Milián, A. Couairon, A. Mysyrowicz, and A. Houard, "Generation

of long-lived underdense channels using femtosecond filamentation in air," *J. Phys. B At. Mol. Opt. Phys.*, vol. 48, no. 9, p. 94009, 2015.

[97] A. A. Ilyin, S. S. Golik, and K. A. Shmirko, "Absorption and emission characteristics of femtosecond laser plasma filaments in the air," *Spectrochim. Acta - Part B At. Spectrosc.*, vol. 112, pp. 16–22, 2015.

[98] P. P. Kiran, S. Bagchi, C. L. Arnold, S. R. Krishnan, G. R. Kumar, and A. Couairon, "Filamentation without intensity clamping.," *Opt. Express*, vol. 18, no. 20, pp. 21504–21510, 2010.

[99] J. Kasparian, R. Sauerbrey, and S. L. Chin, "The critical laser intensity of self-guided light filaments in air," *Appl. Phys. B Lasers Opt.*, vol. 71, no. 6, pp. 877–879, 2000.

[100] P. E. Ciddor, "Refractive index of air: new equations for the visible and near infrared.," *Appl. Opt.*, vol. 35, no. 9, pp. 1566–1573, 1996.

[101] J. Van Roey, J. Van Der Donk, and P. E. Lagasse, "Beam-propagation method : analysis and assessment," *J. Opt. Soc. Am.*, vol. 71, no. 7, p. 803, 1981.

[102] M. Takeda, H. Ina, and S. Kobayashi, "Fourier-transform method of fringe-pattern analysis for computer-based topography and interferometry," *J. Opt. Soc. Am.*, vol. 72, no. 1, p. 156, 1982.

[103] M. Mlejnek, E. M. Wright, and J. V Moloney, "Dynamic spatial replenishment of femtosecond pulses propagating in air.," *Opt. Lett.*, vol. 23, no. 5, pp. 382–4, Mar. 1998.

[104] A. H. Guenther and J. R. Bettis, "A Review of Laser-Triggered Switching,"

Proc. IEEE, vol. 59, no. 4, pp. 689–697, 1971.

[105] W. K. Pendleton and A. H. Guenther, "Investigation of a laser triggered spark gap," *Rev. Sci. Instrum.*, vol. 36, no. 11, pp. 1546–1550, 1965.

[106] A. H. Guenther and J. R. Bettis, "Laser-Triggered Megavolt Switching," *IEEE J. Quantum Electron.*, vol. QE-3, no. 11, p. 581, 1967.

[107] L. L. Steinmetz, "Laser-Triggered Spark Gap," *Rev. Sci. Instrum.*, vol. 39, no. 6, pp. 904–909, 1968.

[108] M. J. Kushner, R. D. Milroy, and W. D. Kimura, "A laser-triggered spark gap model," *J. Appl. Phys.*, vol. 58, no. 8, pp. 2988–3000, 1985.

[109] L. B. Loeb and A. F. Kip, "Electrical discharges in air at atmospheric pressure: The nature of the positive and negative point-to-plane coronas and the mechanism of spark propagation," *J. Appl. Phys.*, vol. 10, no. 3, pp. 142–160, 1939.

[110] L. B. Loeb and J. M. Meek, "The mechanism of spark discharge in air at atmospheric pressure. I," *J. Appl. Phys.*, vol. 11, no. 6, pp. 438–447, 1940.

[111] L. B. Loeb and J. M. Meek, "The mechanism of spark discharge in air at atmospheric pressure. II," *J. Appl. Phys.*, vol. 11, no. 7, pp. 459–474, 1940.

[112] J. M. Meek, "A theory of spark discharge," *Phys. Rev.*, vol. 57, no. 8, pp. 722–728, 1940.

[113] J. S. Townsend, "The conductivity produced in gases by the motion of negatively-charged ions," *Nature*, vol. 62, p. 340, 1900.

[114] P. Polynkin, B. Pasenhow, N. Driscoll, M. Scheller, E. M. Wright, and J. V. Moloney, "Seeded optically driven avalanche ionization in molecular and

noble gases," *Phys. Rev. A - At. Mol. Opt. Phys.*, vol. 86, no. 4, pp. 1–8, 2012.

[115] P. Polynkin and J. V. Moloney, "Optical breakdown of air triggered by femtosecond laser filaments," *Appl. Phys. Lett.*, vol. 99, no. 15, 2011.

[116] A. Schmitt-Sody, H. G. Kurz, L. Bergé, S. Skupin, and P. Polynkin, "Picosecond laser filamentation in air," *New J. Phys.*, vol. 18, no. 9, 2016.

[117] M. Rodriguez, R. Sauerbrey, H. Wille, L. Wöste, T. Fujii, Y.-B. André, A. Mysyrowicz, L. Klingbeil, K. Rethmeier, W. Kalkner, J. Kasparian, E. Salmon, J. Yu, and J.-P. Wolf, "Triggering and guiding megavolt discharges by use of laser-induced ionized filaments," *Opt. Lett.*, vol. 27, no. 9, pp. 772–774, 2002.

[118] A. Schmitt-Sody, D. French, W. White, A. Lucero, W. P. Roach, and V. Hasson, "The importance of corona generation and leader formation during laser filament guided discharges in air," *Appl. Phys. Lett.*, vol. 106, no. 12, 2015.

[119] S. Tzortzakis, B. Prade, M. Franco, A. Mysyrowicz, S. Hüller, and P. Mora, "Femtosecond laser-guided electric discharge in air," *Phys. Rev. E*, vol. 64, no. 5, p. 57401, 2001.

[120] F. Paschen, "Ueber die zum Funkenübergang in Luft, Wasserstoff und Kohlensäure bei verschiedenen Drucken erforderliche Potentialdifferenz," *Wied. Ann.*, vol. 37, p. 69, 1889.

[121] E. Sili and J. Pascal Cambronne, "A New Empirical Expression of the Breakdown Voltage for Combinated Variations of the Temperature and Pressure," *World Acad. Sci. Eng. Tecnol.*, vol. 6, no. 4, pp. 1–6, 2012.

[122] T. Fujii, M. Miki, N. Goto, A. Zhidkov, T. Fukuchi, Y. Oishi, and K. Nemoto,

"Leader effects on femtosecond-laser-filament-triggered discharges," *Phys. Plasmas*, vol. 15, no. 1, pp. 2–7, 2008.

[123] K. Sugiyama, T. Fujii, M. Miki, A. Zhidkov, M. Yamaguchi, E. Hotta, and K. Nemoto, "Submicrosecond laser-filament-assisted corona bursts near a high-voltage electrode," *Phys. Plasmas*, vol. 17, no. 4, 2010.

[124] D. F. Gordon, A. Ting, R. F. Hubbard, E. Briscoe, C. Manka, S. P. Slinker, A. P. Baronavski, H. D. Ladouceur, P. W. Grounds, and P. G. Girardi, "Streamerless guided electric discharges triggered by femtosecond laser filaments," *Phys. Plasmas*, vol. 10, no. 11, pp. 4530–4538, 2003.

[125] A. Schmitt-Sody, J. Elle, A. Lucero, M. Domonkos, A. Ting, and V. Hasson, "Dependence of single-shot pulse durations on near-infrared filamentation-guided breakdown in air," *AIP Adv.*, vol. 7, no. 3, p. 35018, 2017.

[126] C. W. Siders, J. L. Siders, A. J. Taylor, S. G. Park, and A. M. Weiner, "Efficient High-Energy Pulse-Train Generation Using a 2^n-Pulse Michelson Interferometer.," *Appl. Opt.*, vol. 37, no. 22, pp. 5302–5305, 1998.

[127] E. W. Rosenthal, N. Jhajj, I. Larkin, S. Zahedpour, J. K. Wahlstrand, and H. M. Milchberg, "Energy deposition of single femtosecond filaments in the atmosphere," *Opt. Lett.*, vol. 41, no. 16, pp. 3908–3911, 2016.